INVESTIGATION OF THE EFFECT OF SPEED RATIO ON WORKPIECE SURFACE TOPOGRAPHY IN CYLINDRICAL PLUNGE GRINDING USING GROOVED AND NON-GROOVED GRINDING WHEELS

by

Akshay Patel

Submitted in partial fulfilment of the requirements
for the degree of Master of Applied Science

at

Dalhousie University
Halifax, Nova Scotia
April 2019

Table of Contents

List of Tables

List of Figures

Abstract

This work explores the effect of integer and non-integer speed ratios on surface topography in cylindrical plunge grinding with grooved and non-grooved grinding wheels. For this investigation, an extensive experimental study was performed along with computer simulations. This research started with the development of stochastic wheel models to carry out 2D cylindrical grinding simulations. The simulator provided an excellent prediction of surface roughness trends and insights into the underlying mechanisms that govern the resulting surface roughness. Next, all the integer speed ratios from 2 to 7 were used in both experiments and simulations to study the workpiece topographies. Integer speed ratios were found to produce higher workpiece surface roughness values compared to non-integer speed ratios, and thread-like patterns were observed for grooved-wheel grinding. A dwell time study was conducted which revealed that the surface roughness improved for dwell times up to 10 seconds for both grooved and non-grooved wheels. Therefore, the final set of experiments and simulations used 10 seconds of dwell time with non-integer speed ratios between 4 and 5. The experiments also found that grooved grinding wheels consume less energy and exhibit less process forces than the non-grooved wheels. Roughness peaks were found to occur in the workpiece surface because of a synchronization phenomenon that can occur between the cutting edges on the grinding wheel and the workpiece. Formulae to determine the minimum number of grinding wheel revolutions required for synchronization at different speed ratios were derived using a kinematical approach. These formulae were used to help predict optimal speed ratios. It was found that a speed ratio of 4.78 yielded the best surface finish of 0.302 μm for grooved-wheel grinding, while a speed ratio of 4.22 produced the best surface finish of 0.189 μm for non-grooved-wheel grinding. Although the grooved wheels yielded a rougher workpiece surface than the non-grooved wheels, grooved-wheel grinding using the optimal speed ratio was able to achieve close to the 0.30 μm “fine quality” surface finish standard. An important key takeaway from the work of this thesis is that grooved wheels have potential to further improve the surface finish if speed ratios with a higher number of grinding wheel revolutions for synchronization are selected and successfully achieved.

List of Symbols Used

α	Thread angle
a	Depth of cut
a_g	Groove depth
A_o	Total surface area on grinding wheel periphery
A_g	Grooved surface area on grinding wheel periphery
b_g	Groove width
b_w	Grinding wheel width
a	Dressing depth
D	Angular distance between two consecutive cuts by two adjacent wheel grains
d_e	Equivalent diameter
d_g	Grain diameter
d_s	Grinding wheel diameter
d_w	Workpiece diameter
E	Specific energy
f	Number of incomplete grinding wheel revolutions
f_r	Infeed rate of grinding wheel into the workpiece
f_g	Groove lead
h	Grain protrusion height
h_m	Undeformed chip thickness
L	Angular grain spacing
l_e	Contact length
η	Groove factor
N	Number of complete wheel revolutions
n_g	Number of wheel grains from Torus method calculations
N_g	Number of wheel grains on the grinding wheel model in consideration

N_s^{syn}	Minimum number of grinding wheel revolutions required for synchronization
N_w^{syn}	Minimum number of workpiece revolutions required for synchronization
n_w	Number of workpiece radials
θ_s	Grinding wheel angular position w.r.t positive X line
θ_{s_step}	Wheel grain angular spacing in non-stochastic model
θ_w	Workpiece angular position w.r.t positive X line
θ_{w_step}	Workpiece radial angular spacing
ϕ_s	Phase angle of grinding wheel after one workpiece revolution
ϕ_w	Workpiece phase difference
P	Spindle power
Q_w	Material removal rate
R_a	Average surface roughness
R_G	Number of grinding wheel revolutions
S	Speed ratio
T_{dwell}	Dwell time
T_{max}	Minimum dwell time required for synchronization
V_g	Grain volume fraction
v_r	Radial feed rate of grinding wheel
v_s	Grinding wheel peripheral velocity
v_w	Workpiece peripheral velocity
ω_s	Grinding wheel angular speed
ω_w	Workpiece angular speed

Acknowledgements

The past twenty months of my graduate studies have been a steep learning curve, and the people who supported me in this journey shall forever have a special place in my heart. I am taking this opportunity to thank each one of them.

Foremost, I express my deepest gratitude to my supervisors, Dr. Andrew Warkentin and Dr. Robert Bauer for their constant support, guidance and motivation throughout the research and writing of this thesis. I consider myself fortunate to have got a chance to work with such amazing researchers. Honestly, I cannot put into words the intensity of gratitude I have for them.

I thank my committee members, Dr. Johnston Clifton and Dr. Uday Venkatadri for their time and valuable feedback on my work.

I wish to thank my senior colleagues, Dr. Al-Mokhtar, Scott, and Cameron for training me with CNC machine operations and their valuable advice in times of need. I thank my colleague, Alex for his help with solving problems in the grinding lab. He has been generous and co-operative in sharing the lab which allowed me to complete my experiments in time. I am thankful to Jon for his timely help in setting up a new microcontroller and also his electronics help throughout the research phase. I appreciate everything that Peter Jones, Kate Hide and Angus McPherson have done in contributing to the progress of my work.

I thank everyone in my family for their love and belief in me. Their blessings, as always, drove me to achieve my goals in time. Mom, I love you. Thank you for being an amazing sculptor of my life. And lastly, there are my fun-loving friends—Akash, Abhishek, Ayushi, Dhananjay, Omkar and Ripu. I thank them for giving me happy distractions outside the work life that helped me relax and re-tune myself.

Chapter 1

Introduction

Cylindrical grinding is an important subfield of grinding technology. It is widely used as a machine tool to obtain smooth surfaces on cylindrical workpieces. A rotating grinding wheel is brought in contact with a rotating cylindrical workpiece to remove unwanted material thereby enhancing the surface and dimensional quality of the workpiece. In addition to cylindrical workpieces, this process is also used to grind taper workpieces, cams, faces of shoulders and various contours on the cylindrical surface using conventional and modified grinding wheels. The utility of the cylindrical grinding process has proved to be crucial in the automotive, aviation, and manufacturing industry. Researchers have constantly attempted to study different aspects of cylindrical grinding in order to improve the process with the intensions of improving workpiece surface finish, tolerances and production rates while reducing workpiece mechanical and thermal damage.

Research has shown that grinding wheels with grooves inscribed on them can reduce process forces and power consumption. However, grooved grinding wheels have been found to yield rougher workpiece surfaces than non-grooved wheels. The challenge is to determine the right conditions for grooved-wheel grinding that can yield fine surface finish as per the grinding standards while maintaining beneficial reductions in process forces and power. The Speed ratio, which is the ratio of the angular speeds of the grinding wheel and workpiece, has not yet received any significant investigation in the cylindrical grinding process. The motivation is, therefore, to use the speed ratio as a primary variable to investigate cylindrical grinding for improved surface finish, lower process forces and spindle power with a grooved and conventional grinding wheel.

1.1 Objectives

The objectives of this thesis are to:

- Investigate using experiments and simulations, the workpiece topographies obtained using the grooved and non-grooved grinding wheel for a wide range of integer and non-integer speed ratios.
- Determine the speed ratios for grooved wheel grinding that can yield the surface as smooth as non-grooved wheel grinding.
- Determine optimal as well as undesirable speed ratios for the surface finish in both the grooved and non-grooved wheel grinding.
- Develop methods to predict good and bad surface-finish-yielding speed ratios.

1.2 Organization of Thesis

The content of this thesis is organized in seven chapters. Chapter 2 gives background information regarding grinding in general followed by a focused discussion on cylindrical grinding and its kinematics. Chapter 3 reviews the literature on optimization of the cylindrical grinding process, simulation techniques and the application of grooved wheels in grinding in general followed by a detailed literature review of cylindrical grinding with grooved wheels. Chapter 4 has been divided into two parts. The first part provides information about the apparatus, input process-parameters and the methodology used for the experimental work in this thesis. The second part discusses the procedural development of the workpiece and the wheel model used for the simulation work of this thesis. Chapter 5 presents and compares the experimental and simulation results using three different studies: The effect of integer speed ratios, the effect of dwell time, and the effect of non-integer speed ratios. Chapter 6 develops an understanding of the synchronization phenomenon in cylindrical grinding for different speed ratio cases to analyze the experimental and simulation results. Chapter 7 explains the trends of the simulation and experimental results using the understanding of synchronization and presents the summary of important results. Chapter 8 presents the conclusions from this thesis work.

Chapter 2

Background

Grinding is a subset of abrasive machining which is a broad field based on the removal of material from a workpiece with the help of abrasives. Grinding wheels, which are formed of abrasive particles, perform the cutting action on the workpiece to remove the material as necessary [1]. Metal removal in the form of small chips is caused by the action of irregularly-shaped abrasive particles interacting with the workpiece material [2]. Grinding is predominantly used after machining as a finishing process to complete the final product. Modern grinding wheels and grinding machines are capable of creating parts that are alike to within a quarter of a thousandth to ten-thousandth of an inch [3]. Due to its capability of machining with high precision and speed, grinding has gained enormous importance in the manufacturing industry.

The two main types of grinding processes are flat grinding and cylindrical grinding. Flat grinding is suitable for machining flat surfaces. The peripheral area, as well as the flat surface area of the grinding wheel, can be used for material removal depending on the desired application [3]. Cylindrical grinding is used to grind round parts.

2.1 Cylindrical Grinding and its Classifications

Cylindrical grinding is the process of removing material from a rotating cylindrical workpiece with a rotating abrasive wheel. Based on the side of the surface to be ground, Cylindrical grinding can be classified into two types: Internal cylindrical grinding and external cylindrical grinding. As shown in Figure 2.1 (a), external grinding is applied to grind the external surface of the workpiece. The wheel and workpiece rotate in the same direction in external grinding. Internal grinding is used for grinding the internal surface of the workpiece (Figure 2.1 (b)) [4]. The long contact path between the grinding wheel and the workpiece acts as a hindrance for cutting fluids to reach the grinding zone making

internal grinding a complicated process to carry out [5]. For internal cylindrical grinding, the wheel and the workpiece rotate in opposite directions with respect to each other.

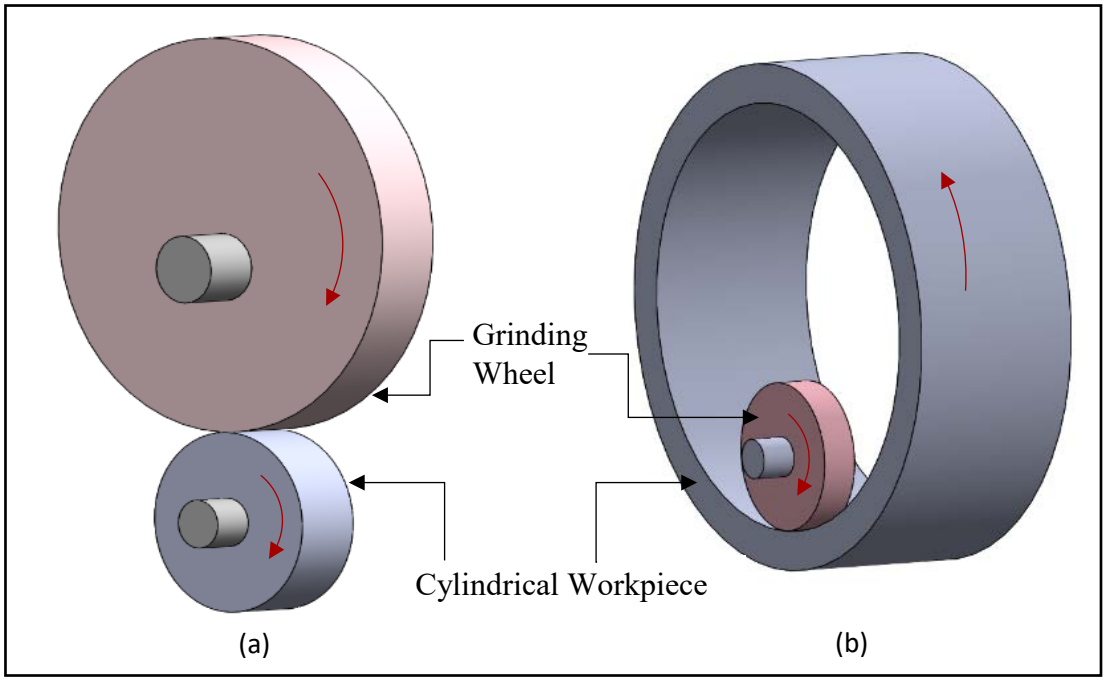

Figure 2.1: (a) External Cylindrical Grinding and (b) Internal Cylindrical Grinding

For the purpose of this thesis, the term "cylindrical grinding" refers to external cylindrical grinding. The term "internal cylindrical grinding" will be clearly used if a discussion specific to internal cylindrical grinding is required. One of the ways of classifying external cylindrical grinding is based on the translational motion of the grinding wheel with respect to the workpiece. Plunge cylindrical grinding is the process in which the grinding wheel travels perpendicular to the rotational axis of the workpiece as it removes the material as shown in Figure 2.2. Traverse grinding is the process in which the grinding wheel travels along the rotational axis of the workpiece. Creep feed grinding is a single pass type of traverse grinding achieved using a single deep cut. Single-pass creep feed grinding needs optimized control over process parameters [6]. The work of this thesis is focused on cylindrical plunge grinding.

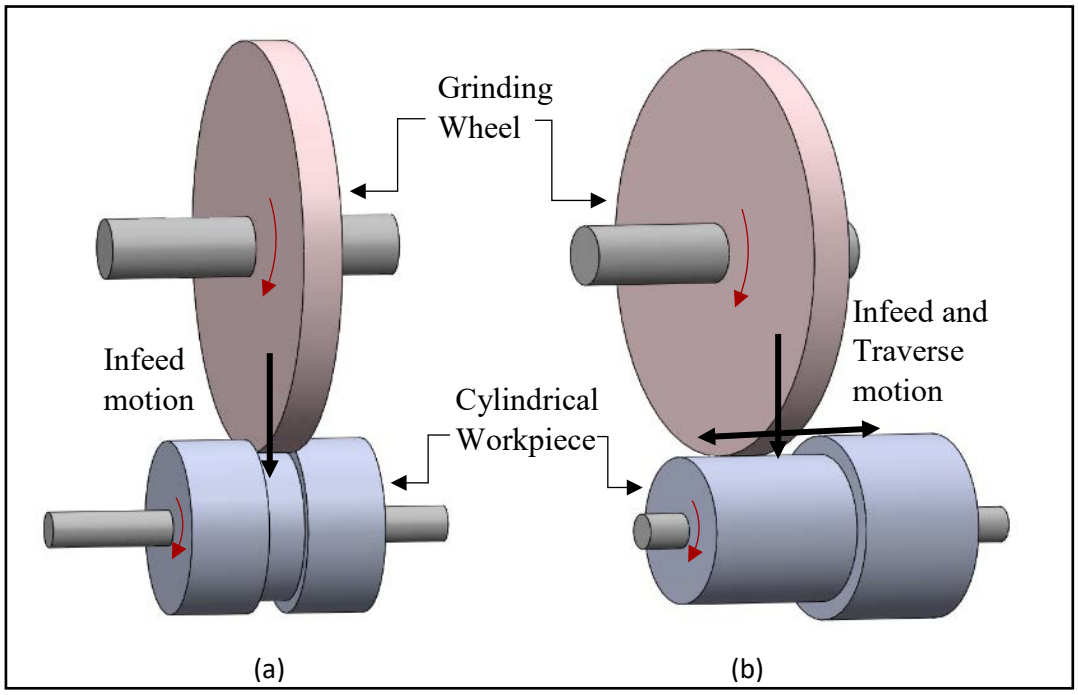

Figure 2.2: (a) Plunge Cylindrical Grinding and (b) Traverse Cylindrical Grinding

2.2 Grinding Wheels

The grinding wheel plays the role of a cutting tool in the grinding process. It is basically made up of abrasive particles bonded together to form a hard surface that is capable of cutting metal parts at high rotational speeds. Performance of any grinding wheel depends on the kind of abrasives it is made up of, the size of the abrasive grains, the kind of bond holding the abrasive grains and the pores between the abrasive grains [7].

2.2.1 Abrasive and Bonding Materials

Abrasive particles, which are held together by bonding material are responsible for removing material during grinding. High hardness, wear resistance and toughness are desirable properties of abrasives [1]. Aluminum oxide is among the most common abrasive materials used for making grinding wheels. Abrasives made up of silicon carbide and cubic

boron nitride have also been used extensively for all types of grinding. Diamond and CBN are considered super-abrasives [8].

Bonding materials are responsible for holding the abrasive grains, and directly play a role in establishing the final shape and structural integrity of the grinding wheel [1]. It is important that bonding material withstand high cutting forces and temperatures for abrasives to remain intact with each other during grinding. In addition to holding the abrasive grits together, a bond should be able to provide adequate grit retention, allow controlled bond erosion which leads to gradual exposure of new cutting points, provide enough strength for effective grinding force transfer from the spindle to the workpiece and provide adequate heat dissipation during grinding [8]. Resin bonds, vitrified bonds and metal bonds are three major material types used for bonding the abrasives together. Vitrified bonds are relatively unaffected to water and oil and are used in most of the grinding wheels. Silicate bond, shellac bond and rubber bond are some other types used in binding the abrasive grits together [1]. In this thesis, a vitrified bond grinding wheel is used.

2.2.2 Marking System for Grinding Wheels

The marking system defined by the American National Standards Institute uses numbers and letters to separately identify the grinding wheels for its type, grit size, grade, structure and bond material [9]. An example of marking the grinding wheels is shown in Figure 2.3.

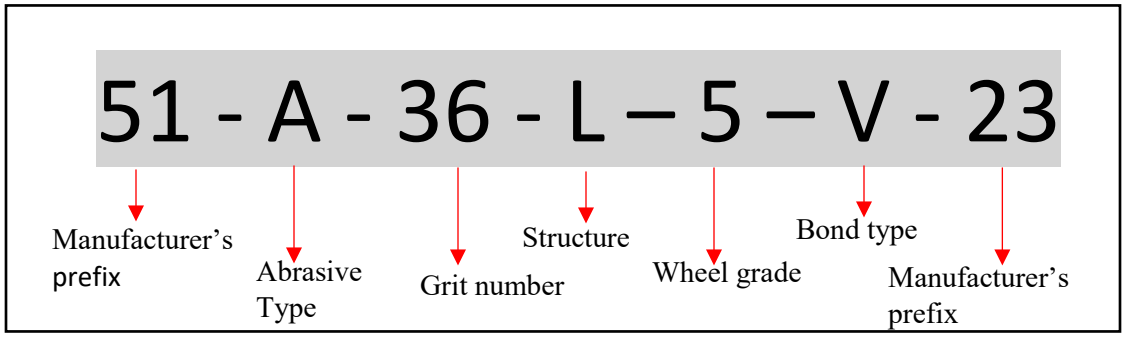

Figure 2.3: Grinding wheel marking system

Abrasive type includes an initial letter of abrasive used. Grain size indicates whether the grits are coarse, medium, fine or very fine. The scale of grade ranges from A

to Z where A is a very soft grinding wheel and Z is a very hard grinding wheel. Structure ranges from 1 (very dense structure) to 15 (very open structure). Bond type is represented by the initial letters of the bonding agents. The last part is for the manufacturer's private marking unique for every manufacturer [1]. In this thesis, a WRA60-J5-W grinding wheel is used corresponding to an Aluminium oxide 60-grit J5 structure vitrified bond wheel.

2.2.3 Wear Mechanisms of Grinding Wheel

Grinding wheels are required to be dressed to account for the changes in the effectiveness of their cutting ability as they wear at the microscopic level. Understanding the wheel wear is important. Knowledge of a wheel's wear characteristics can help understand the changes in process outputs. Three dominant mechanisms of wheel wear are attritious wear, grain fracture and bond-fracture.

Attritious wear is caused by rubbing of the grain with the workpiece which makes it dull. Process forces on the grain increase due to attritious wear which can lead to grain fracture and bond-fracture [10]. Abrasive grain fracture occurs due to mechanical forces induced during chip formation and high thermal shock loads caused by an instantaneous increase in temperature while cutting [11]. Only a fragment of the grain is broken in grain fracture and it leads to the exposure of new grain surfaces —a process which is referred to as "self-sharpening". In bond fracture, the grain completely dislodges from the grinding wheel due to bond breakage. Both types of fracture wear cause irregularities in the wheel shape leading to deterioration of the surface finish and inaccuracy in the dimensions of the machined part [11].

2.2.4 Grain Diameter and Grain Volume Fraction

Grit number in the standard marking system represents the size of an individual grain on the grinding wheel. Grit number M is used to calculate the grain diameter d_g [12]:

$$d_g = 28 \times M^{-1} \tag{2.1}$$

Similarly, structure number S is useful in calculating the grain volume fraction V_g [12]:

$$V_g = 0.02(32 - \mathrm{S}) \tag{2.2}$$

2.2.5 Grooved Grinding Wheels

There are differences in the style of naming grooved wheels in the literature. Intermittent wheels, developed by engraving slots or pockets on their surfaces, have a discontinuous type of contact with the workpiece during grinding. Segmented wheels are believed to be similar to intermittent wheels, but the naming varies for some researchers.

Grooved wheels have grooves engraved on the wheel's peripheral surface at different angles as shown in Figure 2.4. Helically-angled grooves are the most popular and have grooves at a helix angle. Similarly, circumferentially-grooved wheels are helically-grooved wheels with the helix angle approaching 90 degrees. In the same manner, axially-grooved wheels have a helix angle that is equal to zero degrees [13].

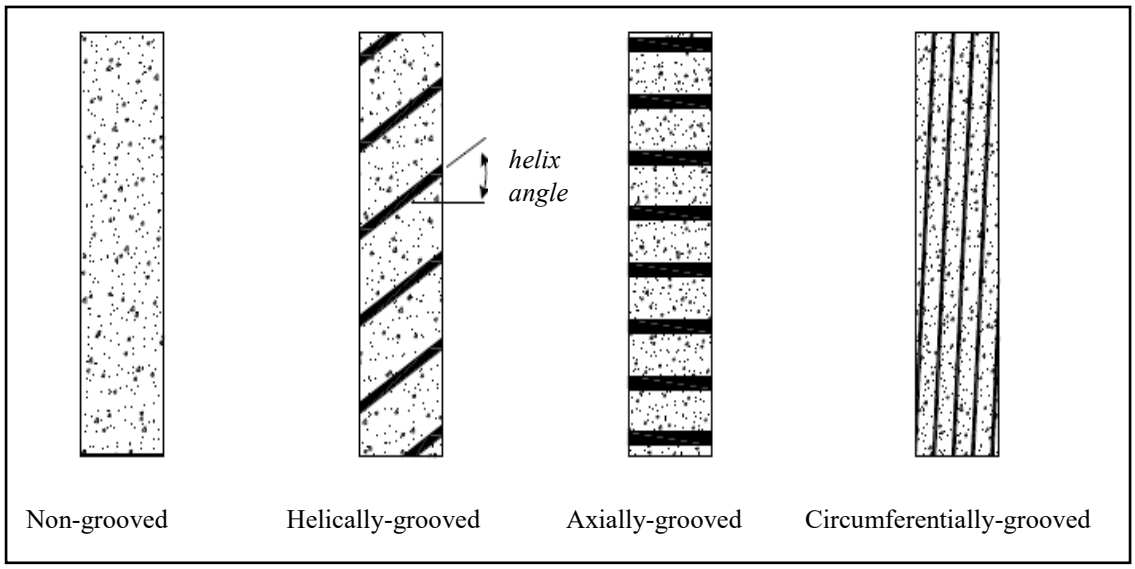

Figure 2.4: Wheel grooving patterns. Adapted from [17].

Figure 2.5 shows the difference between the normal and grooved wheels used for the experimental work of this thesis. A single groove was imparted using a single pass of the dressing tool at controlled speeds of dressing tool and wheel rotation.

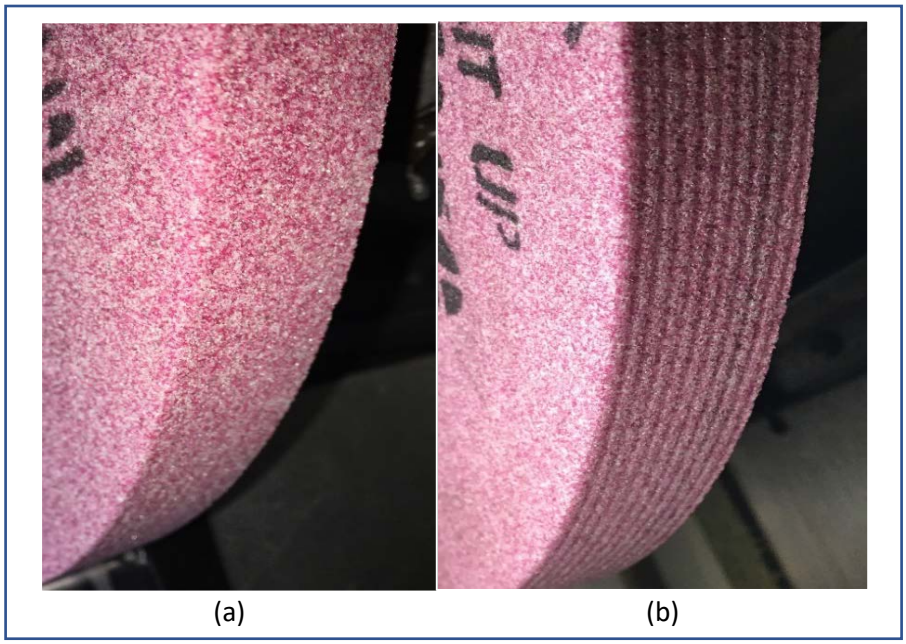

Figure 2.5: Comparison between the peripheral surface of normal and grooved wheel

Verkerk [14] defined the term 'Groove factor (η)' in 1979. It is the ratio of the non-grooved area and total surface area of the wheel:

$$\eta = \left(\frac{A_o - A_g}{A_o}\right) \% \tag{2.3}$$

where A_o is total surface area and A_g is the total area of the grooves on the wheel. The groove factor decreases as the groove area increases. The grooved wheel shown in Figure 5 (b) has a 50 % groove factor.

Mohamed *et al.* [17] defines grooved lead f_g as the distance the groove travels axially around the wheel. It can be calculated by using groove width b_g and groove factor η as follows:

$$f_g = \frac{b_g}{\eta} \tag{2.4}$$

2.3 Grinding Kinematics

This section intends to review important kinematical parameters in cylindrical grinding. Figure 2.6 represents a cylindrical grinding process where the diameter of the grinding wheel is d_s and the workpiece diameter is d_w. The angular speed of the wheel is ω_s and the angular speed of the workpiece is ω_w. The depth of cut into the workpiece is a and the peripheral velocities of the grinding wheel and the workpiece are v_s and v_w, respectively

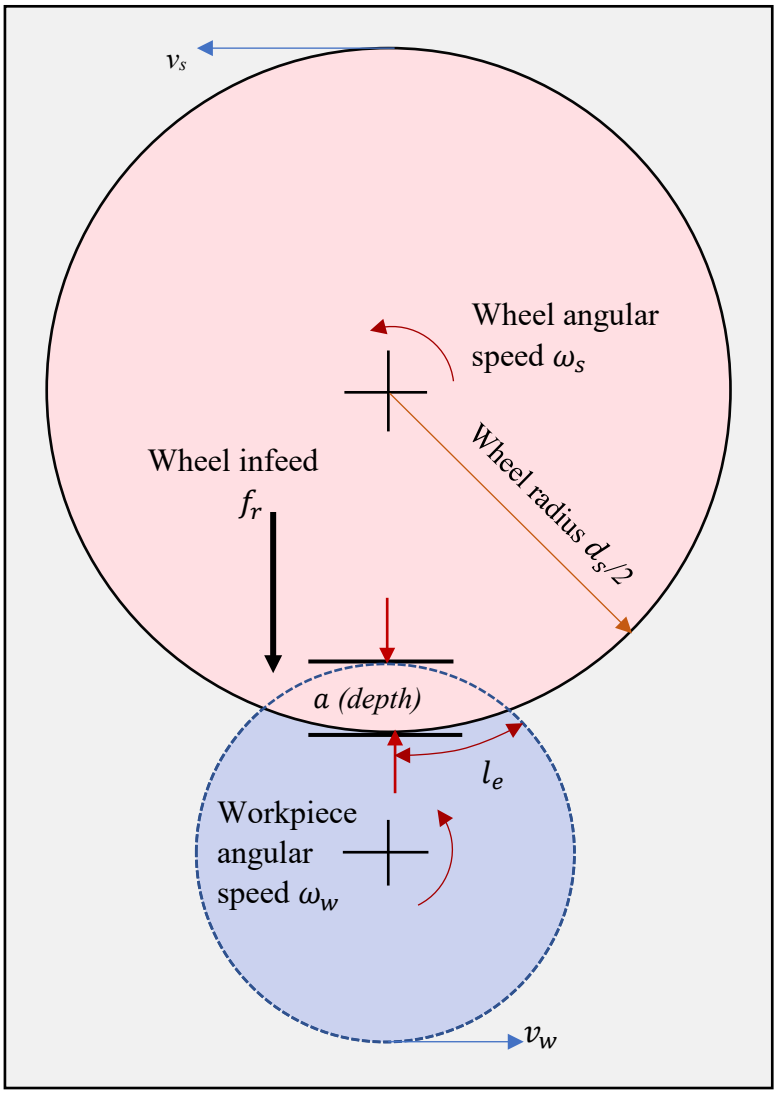

Figure 2.6: Cylindrical grinding parameters

2.3.1 Material Removal Rate (MRR)

The total volume of workpiece material removed per unit time is defined as the material removal rate Q_w [17]. The mathematical expression for Q_w is given as:

$$Q_w = a.b_w.v_w \tag{2.5}$$

where a represents the depth of cut into the workpiece, b_w represents the width of the grinding zone and v_w represents workpiece velocity. For plunge cylindrical grinding, b_w is equal to the grinding wheel width.

2.3.2 Speed Ratio S

The ratio of grinding wheel angular speed ω_w and workpiece angular speed ω_s is defined as the speed ratio S [4]. An interesting fact about the speed ratios is that the same value of the speed ratio can be achieved using an infinite combination of wheel and workpiece speeds.

$$S = \frac{\omega_s}{\omega_w} \tag{2.6}$$

2.3.3 Contact Length l_e

The length of the contact zone between the grinding wheel and the workpiece where the process forces and spindle power are applied is called the contact length l_e [4]. The contact length is estimated using:

$$l_e = \sqrt{a.d_e} \tag{2.7}$$

where d_e is the equivalent diameter determined using Equation 2.8.

$$d_e = \frac{d_s}{1 + \frac{d_s}{d_w}} \tag{2.8}$$

2.3.4 Surface Roughness Parameter R_a

The average surface roughness R_a is the most commonly used parameter in understanding the quality of the surface finish of a machined workpiece. $R_a$is defined as the average absolute deviation of the roughness irregularities from the mean line over a sampling length [18]. The lower the value of R_a, the better the surface finish. Achieving low surface roughness is a primary goal to grinding researchers.

2.3.5 Grain Protrusion Height h and Angular Grain Spacing L

The protrusion height h can be defined as the distance of each cutting edge on the wheel surface from the center of the grinding wheel [19]. It is important to note that the protrusion height of the cutting edges can be greater or smaller than the nominal wheel radius as shown in Figure 2.7. The angular grain spacing is the angular distance between two consecutive grains. The protrusion heights and angular spacing of the grains in a stochastic wheel model are different for different pairs of adjacent grains on the wheel.

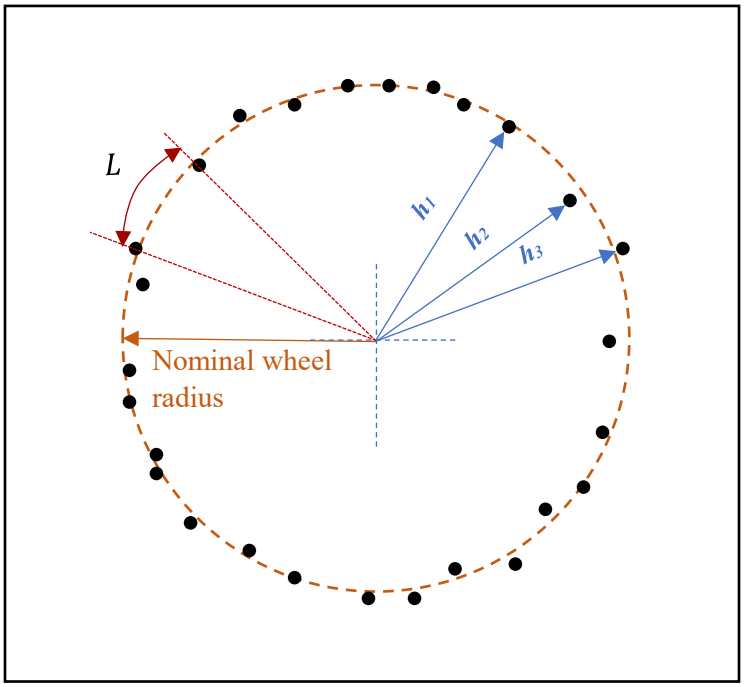

Figure 2.7: Wheel model showing protrusion heights and angular grain spacing

2.3.6 Undeformed chip thickness h_m

Malkin [15] defines the undeformed chip thickness h_m as "the maximum cutting depth taken by a cutting point" as shown in Figure 2.8. This figure visualizes the wheel center moving from O to O′ as the cutting path of length l_k is formed from F′ to A′. The parameters like equivalent diameter d_e and grain spacing L can be used to calculate the undeformed chip thickness in cylindrical plunge grinding as follows:

$$h_m = 2L\left(\frac{v_w}{v_s}\right)\left(\frac{a}{d_e}\right)^{1/2} - \frac{L^2}{d_e}\left(\frac{v_w}{v_s}\right)^2 \tag{2.9}$$

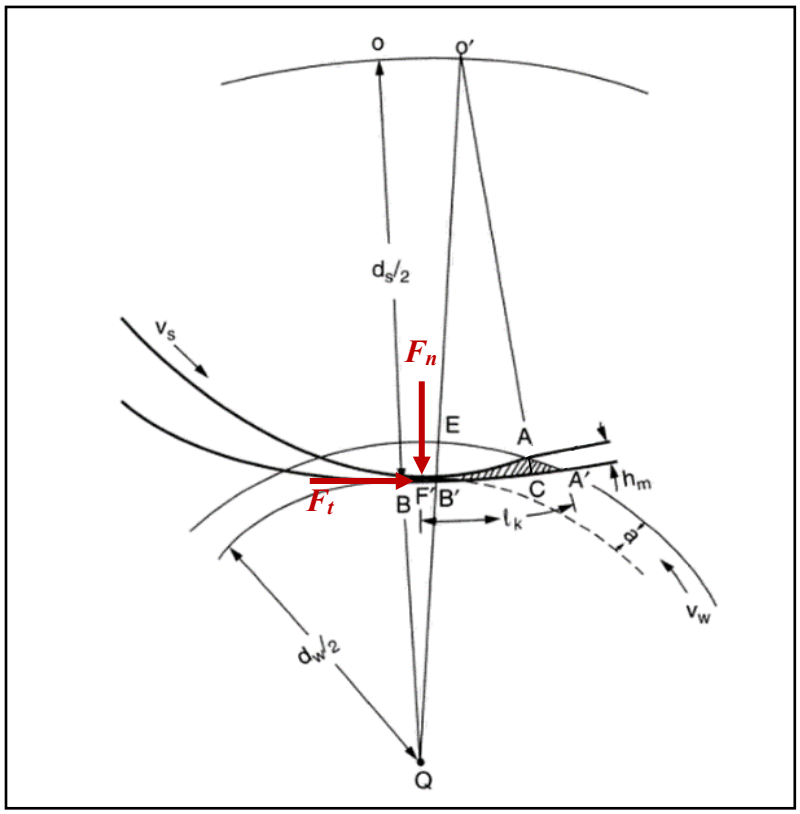

Figure 2.8: Undeformed chip geometry for external cylindrical grinding. Adapted from [15].

2.4 Grinding Forces and Spindle Power

The material removal by a grinding wheel results in the application of a normal force F_n, tangential force F_t and transverse or axial force F_a on the workpiece. These process forces can be measured using force sensors. As shown in Figure 2.8, the normal force acts along the line of wheel-workpiece centers in the grinding zone towards the workpiece. The tangential force is applied tangentially to the workpiece circumference in the grinding zone at the wheel-workpiece interface. In cylindrical plunge grinding, since the wheel does not move axially to remove the workpiece material, the transverse force F_a is typically very small. However, the transverse force reading can be used to identify the presence of errors in the mounting of the workpiece.

The machining of the workpiece also requires a certain amount of spindle power P. The power consumed can be measured by a spindle transducer. Grinding spindle power is also used to calculate specific energy E [17]:

$$\mathrm{E} = \frac{P}{Q_w} \tag{2.10}$$

where Q_w is the volumetric material removal rate defined by Equation 2.5. Grinding efficiency is the reciprocal of specific energy; therefore, grinding efficiency increases as the specific energy decreases.

2.5 Background Conclusion

This chapter introduced the necessary concepts, kinematic relations and variables necessary for this thesis. The concept of grooved wheels in grinding was also introduced which is relevant to the work of this thesis.

Chapter 3

Literature Review

This chapter reviews the literature focused on optimizing the cylindrical grinding process in terms of improvement in workpiece surface finish, as well as reduction of process forces and power consumption. It also reviews the techniques used to simulate the cylindrical grinding process. Finally, the effect of grooves on the cylindrical grinding process has been summarized.

3.1 Review of Literature on Optimization of Cylindrical Grinding

Researchers have experimented with different combinations of process parameters to investigate the dominant factors contributing to the surface finish in cylindrical grinding. There have been several studies based on trying to find the optimum process parameters, workpiece material and grinding conditions that could enhance the workpiece surface finish. This chapter reviews some studies that aimed to optimize the cylindrical grinding process by determining the factors that improve or deteriorate the resulting surface finish of machined cylindrical workpieces.

3.1.1 Workpiece Material Hardness

George *et al.* [20] conducted cylindrical grinding experiments with an array of machine variables like work speed, depth of cut and hardness of the material. The authors established an empirical relationship between surface roughness values and input parameters and based their optimization of the cylindrical grinding process on the Taguchi method. Experimental results showed a decrease in surface roughness with an increase in workpiece material hardness. Panthangi and Naduvinamani [21] used different grades of mild steel like EN 19, EN 24, and EN 31 as workpiece material to determine optimum

cylindrical grinding conditions for surface finish. The ANOVA technique was applied to the experimental data using three variables: material hardness, workpiece speed and depth of cut. It was found that the workpiece hardness was the most contributing factor towards surface roughness. Similarly, Patil *et al.* [22] also found that the workpiece hardness contributed most to the workpiece surface roughness.

3.1.2 Infeed and Depth of Cut

George *et al.* [20] observed an increase in surface roughness with depth of cut. Panthangi and Naduvinamani [21] found a slight improvement in surface finish with an increase in depth of cut. Patil *et al.* [22] reported an increase in surface roughness with infeed and grinding depth. Pal *et al.* [23] studied the effects of different parameters on the surface finish in cylindrical grinding. Grinding parameters like infeed, longitudinal feed and work speed were used as variable inputs for grinding cylindrical workpiece of mild steel. Three varied levels of each parameter were used and the output response was noted. Surface roughness was found to increase with an increase in longitudinal feed and infeed. Finally, maximum surface finish was achieved with an infeed of 0.0406 mm/cycle, a longitudinal feed of 70.829 mm/sec and a work speed of 80.613 rpm. Kumar *et al.* [24] used Taguchi's parameter design approach to optimize cutting speed and depth of cut in cylindrical grinding. To evaluate the effects of these parameters, the authors used techniques like signal-to-noise ratio, analysis of variance and orthogonal arrays. The orthogonal array was used to plan the experiments while ANOVA, a method that analyzes the group mean differences in a sample, was used for determining the parameters that significantly affected the final surface quality. A cutting speed of 41.07 m/min and a depth of cut of 0.020mm were concluded to be the optimal values for achieving the highest MRR of 19.906 mm^3/s. Cutting speed contributed to 47.30% and depth of cut contributed to 4.40% in the final result which shows that cutting speed had a larger influence on the final outcome. Kumar *et al.* [25] optimized cylindrical grinding process parameters like speed, feed and depth of cut for obtaining enhanced surface finish on C40E steel. ANOVA was used to analyze surface roughness results using "smaller is better" criteria. The workpiece speed contributed the most towards the surface roughness followed by the feed and depth of cut. From this optimization technique, grinding speed of 210 rpm, the feed of 0.11 mm/rev and

depth of cut of 0.04 mm were found to be the optimized values for achieving best surface finish. Rudrapati *et al.* [26] determined the dominant parameters contributing to the surface roughness. The parameters, according to their dominant effect in descending order on surface roughness were longitudinal feed, infeed and work speed. Krishnan *et al.* [27] optimized the process parameters like work speed, feed rate and depth of cut to achieve surface quality and high material removal rate when grinding cylindrical workpiece of AISI 4140 steel. The authors utilized the experimental data to build a mathematical surface model using a statistics-based optimization technique called as Response Surface Methodology. The depth of cut was found to directly affect the surface roughness in both predicted surface results and experimental results. Thiagarajan *et al.* [28] observed an increase in workpiece surface roughness with an increase in the feed and the depth of cut.

3.1.3 Workpiece Speed and Wheel Speed

George *et al.* [20] observed an increase in surface roughness with wheel speed while Panthangi and Naduvinamani [21] and Pal *et al.* [23] found an improvement in surface finish with an increase in workpiece speed. Thiagarajan *et al.* [28] evaluated the effect of process variables on the tangential grinding force, surface roughness and grinding temperature in cylindrical grinding. The tangential force and surface roughness were found to decrease with an increase in wheel velocity and the workpiece velocity. The grinding temperature was found to increase with wheel speed, workpiece speed, feed rate and grinding depth. The optimization results obtained using ANOVA showed that the MRR was influenced by the roughness constraint. Their model predicted an increase in MRR significantly if the roughness constraint was raised. The ANOVA model outputs concluded that the surface roughness decreased with wheel speed and workpiece speed. Rudrapati *et al.* [29] studied the relation of infeed, longitudinal feed and work speed with the surface roughness in cylindrical grinding of mild steel workpieces. For this purpose, the authors used response surface methodology (RSM). The ANOVA technique was also used to obtain significant coefficients to help understand the contribution of different process parameters on the final surface roughness effect. The relationship between process and response was determined using a mathematical model. Of all the three parameters, work speed had a significant effect on surface roughness. Sharma *et al.* [30] also used the

Taguchi method to optimize the process parameters in cylindrical grinding. The authors developed a mathematical model based on regression analysis to compare experimental and predicted surface roughness. The authors concluded that the surface roughness decreased with an increase in wheel speed.

Kiyak *et al.* [31] investigated the effect of various machining parameters like workpiece speed and feed rate on the surface roughness of AISI 1050 steel in dry and wet cylindrical grinding at a constant wheel speed of 20 m/sec and depth of cut of 0.025 mm. The surface roughness increased with an increase in workpiece speed at different feed rates (Figure 3.1). The surface roughness was found to increase with material removal rate for dry grinding due to rising workpiece thermal damage when compared to wet grinding. It was found that a lower feed rate and workpiece speed yielded a better surface finish for cylindrical workpieces.

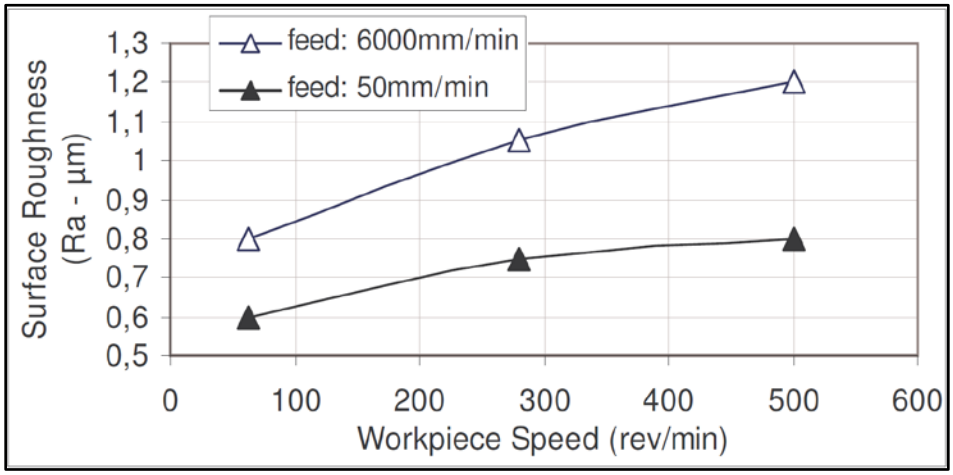

Figure 3.1: Effect of workpiece speed on surface roughness at different feed rates in wet cylindrical grinding, adapted from [31].

Table 3.1 summarizes the effect of various grinding parameters on workpiece surface finish as observed by different authors. The summarized data shows that the surface roughness is directly dependent on the depth of cut and the grinding infeed. No clear upward or downward trend in workpiece surface finish was observed by the workpiece speed. Though some authors used varying wheel speed and workpiece speed, no specific relation like speed ratio was used to investigate the effect of the varying wheel and workpiece speeds in a defined pattern.

Author	Year	Workpiece material	Wheel material	Workpiece hardness	ω_s	ω_w	a	f	longitudinal feed	Ra
Kiyak et *al.* [27]	2003	AISI 1050 steel	SiC	-	-	▲	-	-	-	▲
Pal *et al.* [23]	2011	Mild steel	Not reported	-	-	▼	-	▲	▲	▲
Thiagarajan *et al.* [28]	2011	Al/SiC composite	Al_2O_3	-	▲	▲	▼	▼	-	▼
Rudrapati *et al.* [29]	2012	Mild steel	Not reported	-	-	▲	-	▲	▲	▲
George *et al.* [20]	2013	EN 24, EN 31, and EN 353	SiC	▲	▼	-	▼	-	-	▼
Sharma *et al.* [31]	2016	Not reported	Not reported	-	▲	-	-	-	-	▼
Pathangi and Naduvinamani [25]	2017	EN 19, EN 24, and EN 31	Not reported	▲	-	▲	▲	-	-	▼
Patil *et al.* [26]	2017	EN 19	SiC	-	-	-	▲	▲	-	▲
Krishnan *et al.* [24]	2018	EN 19	Not reported	-	-	-	▼	-	-	▼

Table 3.1: Effect of grinding parameters on surface roughness for different authors. "▲" represents an increase and "▼" represents a decrease in the parameter value.

3.2 Review of Cylindrical Grinding Simulations

Researchers have simulated various aspects of a cylindrical grinding process like workpiece texture, wheel models, grinding temperatures and energy partitions using numerical, analytical, empirical, and FEM techniques.

3.2.1 FEM-Based Simulations

Zahedi *et al.* [32] modelled the cylindrical grinding process using FEM simulation of a single CBN grain on 100Cr6 steel for two different nominal grain diameters: 76 µm and 151 µm for a varying depth of cut and cutting velocity. The authors generated a stochastic grinding wheel model by using the actual wheel topography measurements to position the grains using a Gamma probability density function. The material model sensitive to temperature and strain rate that allowed for the prediction of work-hardening and thermal softening was used. The authors found that sharper grains exhibited smaller forces and higher material removal for the same depth of cut. Thermal softening was found to be a dominant factor for larger strain rates and the work-hardening was a dominant factor for smaller strain rates. Ding *et al.* [33] also used FEM-based simulations to investigate the distribution of temperature and energy for different process parameters and thermal physical parameters. The chip removal behaviour of the grinding process was simulated, and the workpiece and the chip temperatures were measured. The source of energy generation was chosen to be workpiece deformation, grit fracture, and wheel-workpiece friction. The energy was provided in the form of heat to the workpiece, grinding wheel, and chips where the maximum temperature was chosen to be the melting point of the workpiece. The grinding energy was partitioned into the workpiece, grinding wheel, grinding chips, grinding fluid and radiation dissipation as shown in Figure 3.2. Increasing the workpiece speed was found to increase the energy partition into the chips. The authors concluded that increasing the workpiece speed improves the surface finish of the workpiece.

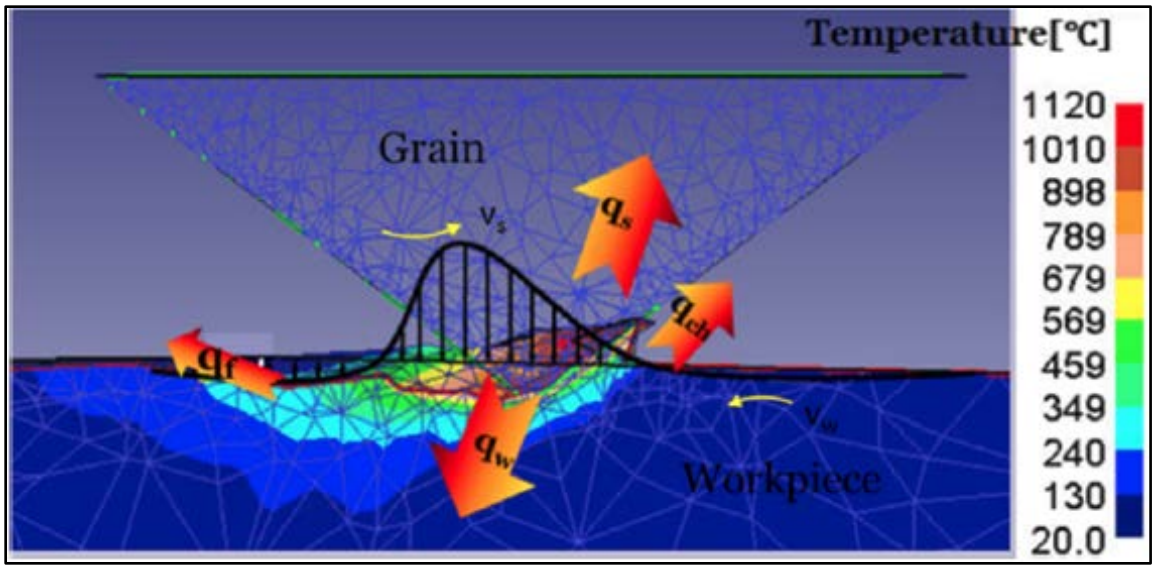

Figure 3.2: Energy partition during grinding, adapted from [30]

3.2.2 Dynamic Simulations

Botcha *et al.* [35] investigated a three-degree-of-freedom lumped-mass model of the cylindrical grinding process that integrated randomly-distributed grinding wheel grains, abrasive-workpiece interactions and the regenerative relationship between machine vibrations and cutting forces. The authors modelled the relative displacement at the wheel-work interface along the plunge direction as a spring-mass-damper system. A data-driven model was developed using two accelerometers and a power cell to extract the signal features for predicting the surface roughness. Kabini *et al.* [36] developed a theoretical model to predict the chatter vibration in the cylindrical grinding process. The dynamic model of the cylindrical grinding process was based on the assumption of chatter vibration as a two-dimensional system and the distributed force was assumed to be along the wheel-workpiece contact. The effects of variation of workpiece speed, wheel speed, and infeed on vibration amplitudes were investigated using the chatter vibration model and were validated using CBN grinding wheel experiments.

Wang *et al.* [37] constructed a surface roughness model of cylindrical traverse grinding based on the fuzzy basis function neural networks using the adaptive least-squares

algorithm. Chi *et al.* [38] proposed a simulation model to predict the workpiece surface topography in cylindrical grinding using the technique of grain trajectory mapping on the workpiece by considering the displacement and micro-interaction between the grinding wheel and the workpiece. The simulation model integrated the influence of the dynamic elements such as vibration and movement of grains, and the static elements such as workpiece deformation, the cutting mechanism and residue material. The authors developed the workpiece topography by first modelling the grinding wheel and calculating the grain trajectory, calculating the displacement of grains caused by deformation and vibration and finally computing the topography height by analyzing the grain passing through each point on the workpiece. Figure 3.3 shows one of the simulated workpiece topographies obtained using the technique discussed above. Guo, J [39] presented a surface roughness prediction model of traverse cylindrical grinding that combined the cylindrical grinding parameters and the time-domain and frequency domain effects of workpiece vibrations. The static and dynamic features were combined to form a feature vector which was used as an input variable to the surface roughness prediction model. The authors used the Gaussian kernel function for computation in high-dimension feature space to build the surface roughness prediction model. The computational efficiency was improved by adopting the sequential sparse Bayesian learning algorithm.

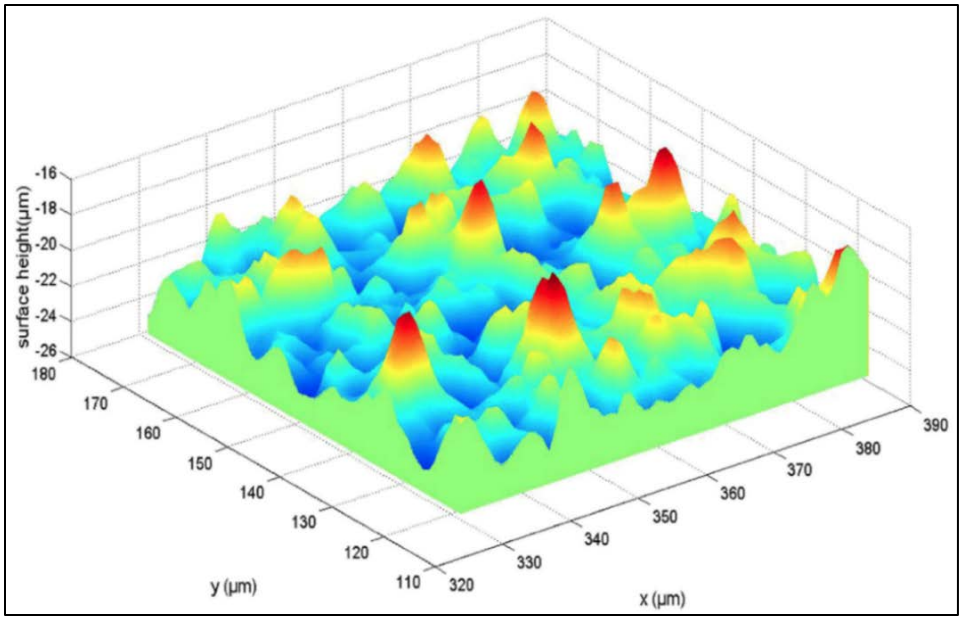

Figure 3.3: Simulated workpiece topography, adapted from [38]

Voronov. S. A and Veidun. Ma [40] proposed a dynamic cylindrical grinding model that calculated the cutting forces, predicted the surface geometry and investigated the effects of cutting conditions on vibrations. The authors assumed the cutting thickness and cross-sectional area of the grain and material contact as the key variables influencing the grinding process. The simulations were performed considering the grinding process as a flat system with two orthogonal degrees of freedom and the cutting forces were resolved along the feed direction and normal to the feed direction. Lee *et al.* [41] developed a cylindrical plunge grinding simulation system to establish the standards of grinding operation. The authors modelled the phenomena of dressing, chip geometry, wheel surface, workpiece burns and spark-out to base the simulation process on the behaviour of cutting-edge wear. An optimization routine was also formed by fixing the constraints on surface roughness, wheel wear and grinding power to get the optimum grinding conditions. The mathematical model of this work did not predict the workpiece topography after grinding.

3.2.3 Kinematical Simulations

Liu *et al.* [34] investigated the effect of the swivel angle which is the angle of tilt of grinding wheel axis relative to the workpiece axis on the surface finish of different materials. This study was approached experimentally and numerically. For point grinding, the workpiece surface is generated at the point, unlike conventional grinding where the surface is generated at a line. The authors assumed that the protrusion heights of the active grains were normally distributed. Grain spacing was considered to be a uniform distribution along the surface of the grinding wheel. A slight decrease in the surface roughness was observed as the cutting speed increased which can be attributed to an increase in total abrasive grains interacting with the workpiece. It was further concluded that there is no significant impact of swivel angle on the resulting workpiece surface roughness.

3.3 Grooved Wheels in Grinding

Discontinuous grinding wheels with multi-porous grooves have benefits of the long-life span and low production cost [42]. Kim *et al.* [42] found that the implementation of grooved wheels was problematic in practice because of limited groove depth and need of re-grooving the wheels frequently. A helical groove pattern is one of the most common groove patterns used in grinding nowadays. Helical grooves are imparted at an angle called the helix angle. Nakayama *et al.* [43] first proposed that modifying the wheels with helical grooves could lower energy. Quite recently, Mohamed *et al.* [44] proposed a new method that used a single point diamond dressing tool to groove and re-groove the grinding wheel.

A review paper by Li and Axinite [45] identifies textured wheels as grinding wheels with specially designed and implemented active and passive areas on their surface. The authors state that the surface finish obtained using textured wheels is rougher than conventional wheels due to the small overlapping part of neighbouring wheel grains influenced by the increased distance between the grains in texturing the wheels. Workpiece texturing has been found to be an interesting phenomenon when using textured grinding wheels. Li and Axinite observed that an improvement in coolant transportation, heat dissipation and wheel wear resistance, and a reduction in grinding temperatures, forces and energy consumption has been reported widely in the literature. A recent review paper by Cameron *et al.* [13] on grooving processes of vitrified bond grinding wheels reports similar advantages of grooved wheels as Li and Axinite [45]. The authors also reported a trade-off between these advantages and workpiece surface finish.

The fly-cutting experiments of Nakayama *et al.* [43] showed a significant reduction in wheel wear when grinding with grooved wheels whereas Mohamed *et al.* [49] and Aslan and Budak [46] found that the grooved wheels had no significant effect on the wheel wear.

Nakayama [43] found that grooving of the wheel before machining showed elimination of grinding burns and waviness on the surface. Suto *et al.* [47] found an increase in cooling efficiency for grooved wheel grinding. Similarly, Mohamed *et al.* [49] found that the chance of workpiece burn reduced by 50 % when using a circumferentially-grooved wheel. The thermos mechanical force prediction model of Aslan and Budak [45]

and the force prediction model of Kwak and Ha [48] proposed that increasing the grooved area on the wheel reduces the process forces. Mohamed *et al.* [49] studied the degree of workpiece burn and proved that grooved wheels increase the abrasive grain spacing which results in a reduction of cutting forces and thermal damage. Researchers believe that the reduction in thermal damage of the workpiece due to grooved wheel grinding can be attributed to the elimination of uneven thermal expansion of the workpiece and better circulation of coolant through the grooves leading to less heat generation in the grinding zone. Several studies have found that the specific energy reduces significantly for grooved wheel grinding as compared to non-grooved wheel grinding [49,50,51]. The grooved wheels were found to increase the surface roughness [14,52,53].

3.3.1 Cylindrical Grinding with Grooved Wheels

Uhlmann and Hochschild [54] chose cylindrical grinding to evaluate the influence of structured and non-structured CBN grinding wheels. The authors used a universal cylindrical grinding for machining along with rotating cutting force dynamometer to record grinding forces. The grinding forces were found to decrease with the abrasive layer. Also, mean heat development was lower for grooved wheels. The authors described this result as an effect of better lubrication that could have reduced the friction resulting in an increase in the ductile phase of chip formation. Discontinuous heat generation due to segmentation and better accessibility of coolant to the grinding area were the reason for lower heat generation.

Gavas *et al.* [55] found that helically-grooved wheels improved the surface finish. In one study, Gavas *et al.* [56] compared the surface roughness results of grinding three different grades of steel with helically-grooved wheels and conventional wheels. Helically-grooved wheels used for the experiments having angles of 15° and 30° showed improved surface roughness and roundness than a flat-surface wheel. It was also observed that the surface roughness and roundness had different effects depending on material type and grinding method. In general, the surface roughness and roundness were found to improve with grooved wheels.

Koklu [57] studied the cylindrical grinding process using helically-grooved grinding wheels for four different types of steel. One of the main results of this study shows that grinding with helically-grooved wheels improves the surface finish of the workpiece. It was further observed that, for a helix angle of 45°, surface roughness and roundness improved by 28-73% and 47-137%, respectively for all four types of steel. Residual stresses reduced by 4.4% for AISI 1040 steel. Performance of flat surface grinding wheels (FSGW) and helically-grooved grinding wheels with different angles (HGGWs) was compared. ANOVA was used to analyze the performance of materials and grinding wheels in their final contribution to surface roughness and roundness. It was further evident from the analysis that material type and grinding wheel accounted for 18.6% and 73.8% contribution on the achieved surface roughness. Material type and grinding wheel accounted for a contribution of 15.8% and 65.6% on the roundness after machining.

Tawakoli *et al.* [58] used different types of structured grinding wheels to perform Cylindrical plunge dry grinding of bearing steel (100Cr6, HRC 62±2) for comparing the effects of structured wheels with that of conventional wheels. The authors modified the conventional cBN wheel by special conditioning monitored by dressing depth and dressing feed to get the desired structures on the wheel. The authors reported a reduction in grinding forces and energy as the contact layer reduced; however, the workpiece surface finish deteriorated.

The most recent study of the effects of the grooved wheel in cylindrical grinding was done by Dewar *et al.* [59]. A high-angled helically-grooved grinding wheel with a 50 % groove factor was used for grinding at different infeed rates. There was a significant reduction in the normal and the tangential forces for grooved wheel grinding. Grooved wheels reduced the power consumption by 29% but increased the surface roughness of the workpiece by 38%. The authors stated that the grooved wheels could reduce the cycle time up to 30%.

There has not been a significant amount of work in the literature on cylindrical grinding with grooved wheels. Only a few researchers have used grooved wheels in cylindrical grinding and have reported advantages like reduction in process forces, energy consumption, and thermal damage with a compromise in workpiece surface finish.

3.4 Conclusion of Literature Review

In this chapter, the literature was reviewed for improving the cylindrical grinding process. There has been a difference in the findings of the parameters that contribute most to the surface roughness. While some studies suggest that increasing depth of cut increases surface roughness, other studies suggest the same for feed and workpiece speed. The simulation studies on cylindrical grinding were also reviewed. There has not been much simulation work in cylindrical grinding that predicts the workpiece topography for different combinations of wheel speeds and workpiece speeds. The use of grooves in grinding was also reviewed, which suggests that the surface roughness of the workpiece generally deteriorates whereas the process forces, power consumption and workpiece thermal damage tend to reduce. It has been observed that the literature lacks both experimental and simulation research on the effect of wheel-workpiece speed relation on the surface finish in cylindrical grinding. Also, no studies using a grooved wheel for cylindrical grinding simulation was found.

Chapter 4

The Methodology of Experimental and Simulation Work

This chapter will discuss the apparatus, experimental procedure and process parameters for the experiments. It also discusses the simulation parameters and the design of the workpiece and the wheel model for the corresponding simulation work.

4.1 Experimental Work

4.1.1 Setup for Cylindrical Grinding Experiments

Figure 4.1 shows the cylindrical grinding setup used for the grinding experiments in this thesis. The rotary axis machine developed by Dewar. S [4] was used to hold cylindrical workpieces. The rotary axis was mounted on a force dynamometer, which was attached to the work bed of the CNC grinding machine. The rotary axis unit was aligned with the spindle using a Mitutoyo dial indicator and was fixed on the mounting plates with 4 fine-threaded bolts. The entire unit was covered with an aluminum waterproofing box that had a circular hole for the cylindrical workpiece to extend out for grinding.

A coolant nozzle was aligned so as to direct the coolant jet on the wheel circumference during dressing, grooving and grinding operations. A pressure gauge was attached to the coolant nozzle to monitor the coolant pressure. The wheel was allowed to revolve for 10 seconds after each operation to remove excessive coolant on its peripheral area. The grinding wheel was initially trued by dressing it with a single-point diamond dressing tool and later balanced on a balancing device. The change in wheel diameter with each dressing pass was monitored using the CNC controller. A single-point diamond tool was fixed on the grinding machine bed. The wear of the dressing tool with each set of experiments was monitored using a Celestron Digital Microscope Pro.

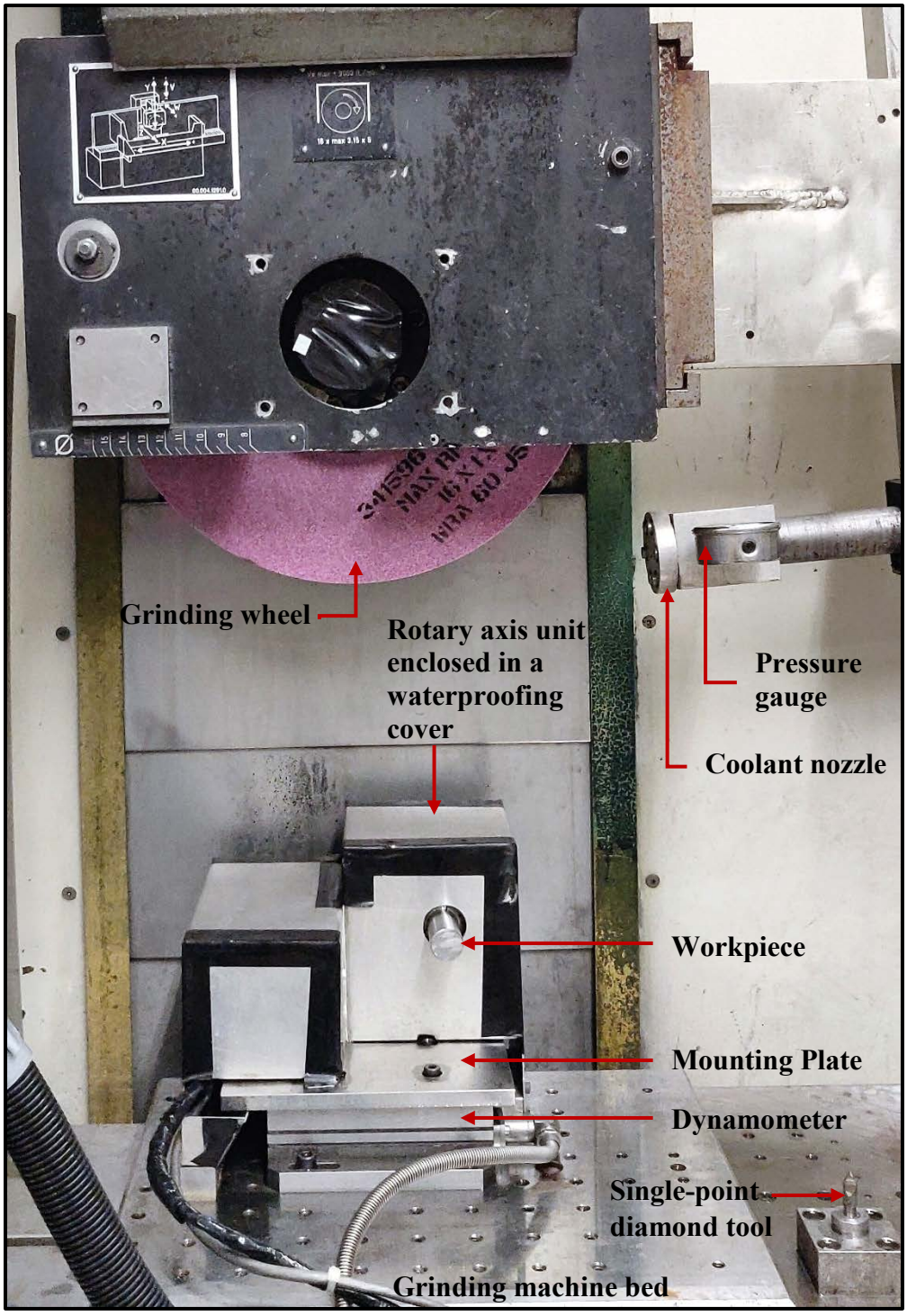

Figure 4.1: Setup of cylindrical grinding experiments

4.1.1.1 CNC Grinding Machine

A Blohm Planomat grinding machine was used for dressing, grooving and grinding operations. This machine is controlled by a Fanuc 18i-m CNC controller. The machine has provisions for attaching sensors, coolant nozzles, and cutting tools. Figure 4.2 shows the Blohm Planomat CNC grinding machine with the cylindrical grinding setup on its work bed.

Figure 4.2: Blohm Planomat CNC grinding machine

4.1.1.2 The Rotary Axis Machine

The rotary axis used for holding and rotating the cylindrical workpieces was designed and developed by Dewar. [4]. This axis consists of a collet mount and collet master, timing belts, timing pulleys, DC brushed motor, encoder and an electrical box consisting of a motor controller, power supply, encoder receiver, PCB and cooling fans. An Arduino-operated controller was used to control the workpiece speed.

4.1.1.3 Grinding Fluid Delivery

A mixed solution of water and CIMTECH 310 was used as a coolant for all the cylindrical grinding experiments. A circular coherent jet coolant delivery nozzle of 8 mm diameter was used to deliver the coolant in the cutting zone at a rate of 10 gallons per minute. The refractometer shown in Figure 4.3 was used to measure the Brix % concentration of the fluid. The concentration of CIMTECH 310 in water was maintained at approximately 5.1% throughout the grinding experiments.

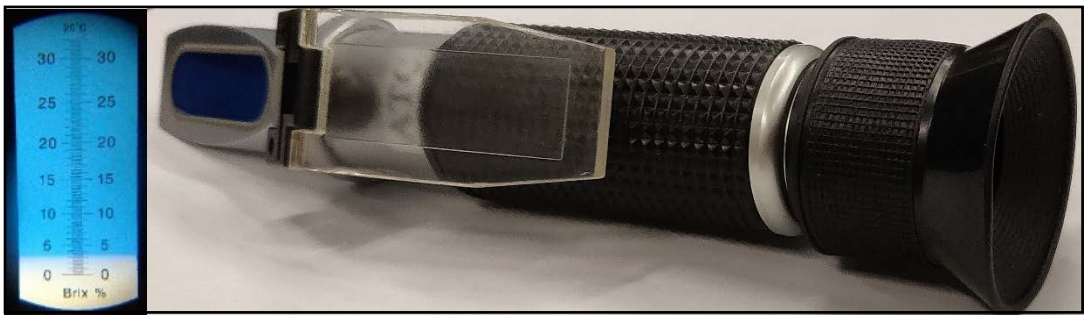

Figure 4.3: Refractometer

4.1.1.4 Workpieces

Precision ground 1045 steel was used as the workpiece material for cylindrical grinding. The workpieces were 1" in diameter and 3.25" in length. One end of the workpiece was inserted into the Collet Master and the other end was cantilevered. The grinding was performed at a distance of 3.25" from the free end of the workpiece (Figure 4.4).

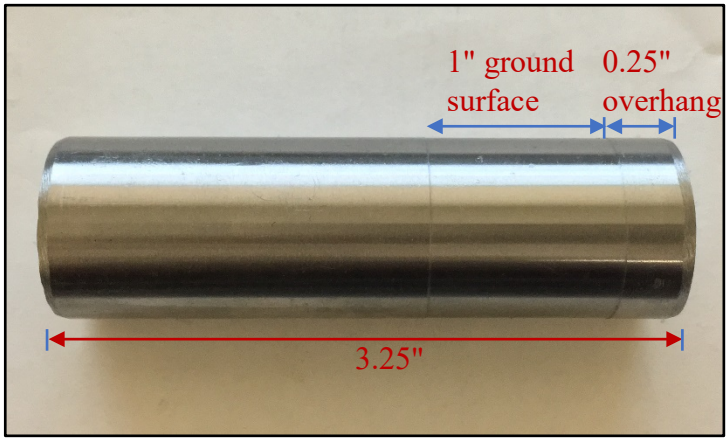

Figure 4.4: Workpiece sample

4.1.1.5 The Stroboscope and the Oscilloscope

The major challenge for the integer speed ratio experiments was to set the wheel and workpiece angular speeds accurately to achieve the desired integer ratios between them. A stroboscope and oscilloscope were used together to achieve the desired integer speed ratios.

A Type 1531-AB electronic stroboscope emitting a high-intensity, short duration light flash was used to measure the angular speed of the grinding wheel and the workpiece and to generate the optical effect of a stationary grinding wheel and workpiece when the speeds were manually adjusted correctly. An Agilent 5461D Mixed-Signal Oscilloscope was connected to the stroboscope to measure the actual flash rate of the oscilloscope once the wheel and workpiece appeared stationary using the strobe light. The actual flash rate of the oscilloscope was determined by measuring the frequency of the flash rate signal waveform on the oscilloscope display.

Figure 4.5 shows the setup of the stroboscope and oscilloscope. White marker were placed on the grinding wheel and the workpiece. The stroboscope was positioned with it's flash lamp facing both white markers. The rotary axis was then given a command to rotate the workpiece at a desired speed. To more precisely determine the actual workpiece rotation rate, the stroboscope flash rate was adjusted until the white marker on the workpiece appeared to have stopped rotating. The oscilloscope, which was connected to the stroboscope was used to measure the flash rate of the stroboscope when the workpiece appeared to have stopped rotating. This measured flash rate, which corresponds to the actual workpiece RPM, was determined and the grinding machine was commanded to rotate the grinding wheel to try to achieve an integer ratio between the grinding wheel angular speed and the workpiece angular speed. in accordance with the variations in the workpiece speeds from intended inputs.

Small adjustments to the grinding wheel speed were then made to ensure that the white marker on the wheel appeared stationary. Since the grinding wheel speed had to be adjusted according to the workpiece speed, the grinding wheel speed was not exactly 1000 RPM as planned. This small difference in wheel speed was acceptable since the focus of this thesis was to study the speed ratios.

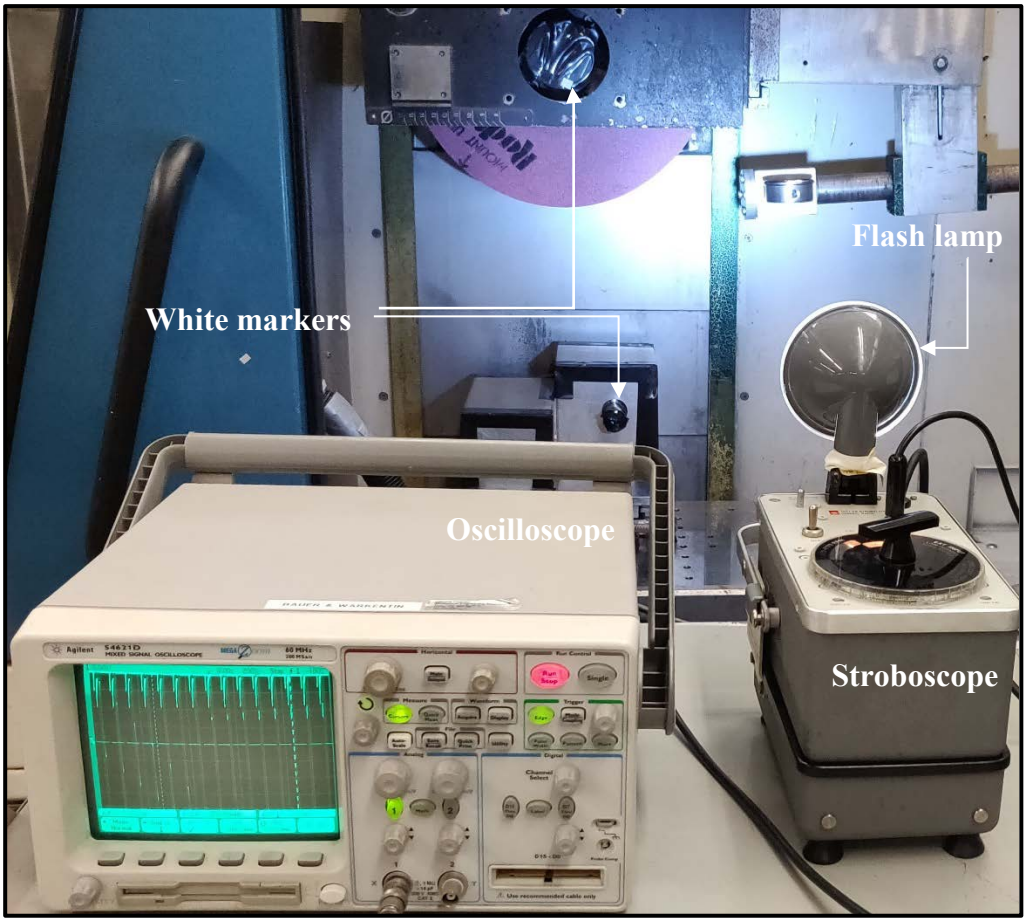

Figure 4.5: Stroboscope and oscilloscope set-up for integer speed ratio experiments.

4.1.1.6 The Tachometer

A hand-held digital tachometer was used to measure the workpiece speed instead of the stroboscope and oscilloscope assembly for the experiments that did not require the speed ratios to be an integer. The tachometer was calibrated by comparing it's speed readings with the stroboscope and the oscilloscope unit's readings. The tachometer was found to be accurate to within 0.1 RPM. The major reasons for replacing the stroboscope and the oscilloscope unit with the tachometer was ease of use and reduced setup times.

4.1.1.7 Data Acquisition Instrumentation

Figure 4.6 shows the instrumentation setup for acquiring force and power data during the grinding experiments. The force dynamometer acquired the real-time force data during grinding and sent it for amplification to the charge amplifier. The signal of the force data was sent from the charge amplifier to the connector block. The power transducer measured the power required for the spindle motor and sent it to the connector block. The connector block was connected to a Data Acquisition card. The force and power data were read by the Data Acquisition card which was used to process the acquired data using LabVIEW software. Table 4.1 details the data acquisition instrumentation.

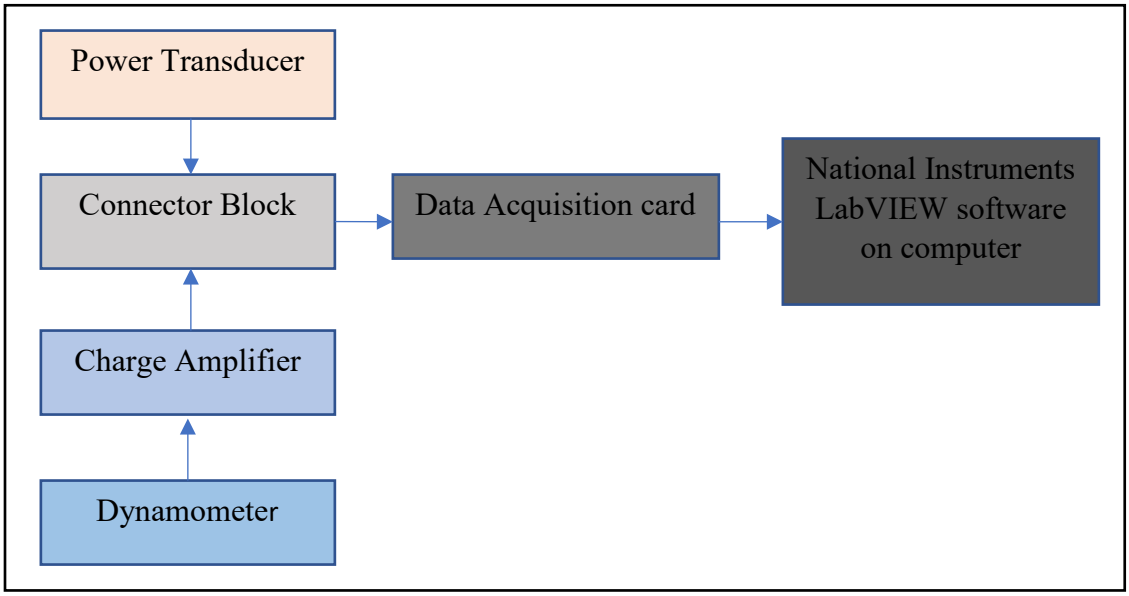

Figure 4.6: Data Acquisition Instrumentation

Instruments	Make and model
Force dynamometer	Kistler: Type 9257B 3 Component Dynamometer
Power Transducer	Load Control Inc. PH-3A
Charge Amplifier	Kistler: Type 5019 Multi-Channel Amplifier
DAQ Card	National Instruments PCI-MIO-16XE-10
Data processing software	National Instruments LabVIEW

Table 4.1: Instrumentation details

4.1.2 Dressing

The grinding wheel was dressed to prepare it for the grinding experiments. The dressing conditions for all the grooved and the non-grooved experiments in this thesis were the same.

A single-point diamond tool was used for dressing. The width of the dressing tool was measured using a Celestron Digital Microscope. The tool was 1150 µm wide at a depth of 4 thou from the tip of the tool. The overlap ratio (the ratio of the tool width and the radial feed rate of the grinding wheel) was consistently maintained at 7.5 for all the dressing operations. This consistency of overlap ratio was achieved by changing the radial feed rate according to the change in tool width with tool wear. Table 4.2 presents the dressing parameters used throughout this thesis where radial feed rate and tool width values correspond to the first dressing operation of this thesis.

Dressing Parameters	**Values**
The radial feed rate of grinding wheel v_r	110 mm/min
The width of the dressing tool b_g at dressing depth	820 µm
Overlap Ratio	7.5
Grinding wheel angular speed ω_s	970 RPM
The depth of cut for each pass d	10 µm

Table 4.2: Dressing parameters

4.1.3 Grooving

A single pass dressing program was used to inscribe 4 thou-deep 1.15 mm-wide circumferential grooves on the grinding wheel. The wheel speed was maintained at 150 RPM while grooving. The tool was fed transversely into the rotating wheel once at the tool infeed rate calculated using:

$$\text{Tool infeed rate} = \frac{b_g \omega_s}{60 \times \eta} \tag{4.1}$$

where b_g is the grooved width, ω_s is the spindle speed and η is the intended groove factor. Shallow circumferential grooves were created on the grinding wheel before every grooved grinding wheel experiment. The grooves were removed using the dressing procedure and new grooves were created before every grooved grinding wheel experiment. The tool infeed rate was changed with the change in the tool width to maintain a consistent 50% groove factor for all the grinding experiments. Table 4.3 presents the grooving parameters.

Grooving Parameters	**Values**
Spindle speed ω_s	150 RPM
Groove width b_g	1.15 mm
Groove factor η	50%
Groove depth a_g	4 thou
Tool infeed rate	5.75 mm/sec

Table 4.3 Grooving parameters

4.1.4 Grinding Parameters

Table 4.4 presents the grinding parameters common to all of the grinding experiments.

Grinding Parameters	Values/make
Workpiece material and dimensions	Precision ground AISI 1045 steel. Diameter = 1 in and length = 3.25 in
Grinding wheel	WRA60-J5-W
Grinding wheel width b_w	1 inch
Grinding wheel speed ω_s	~1000 RPM
Depth of cut a	3 thou
Lubricant	CIMTECH 310
Lubricant concentration and flowrate	5.1 % concentrated, 10 gpm flowrate

Table 4.4 Grinding parameters

4.1.5 Workpiece Topography analysis

The ground workpieces were scanned using a 130 µm optical pen of the Nanovea Profilometer as shown in Figure 4.7. The workpieces profiles were scanned along the circumference of the workpiece. When necessary, area scans of the workpiece surface were taken using the optical pen. The acquired scans were processed using 3D Professional software.

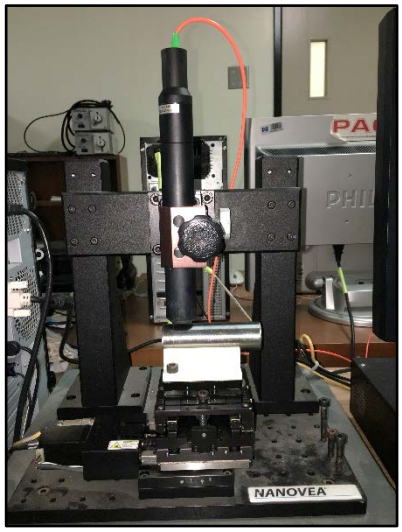

Figure 4.7: Nanovea Profilometer

4.2 Simulation Work

A 2D kinematic cylindrical grinding computer simulator developed by Dr. Robert Bauer was used to predict and compare the surface topography and the surface roughness of the cylindrical workpieces after grinding. The simulator contribution of this thesis was limited to developing a stochastic grinding wheel model for comparison of the simulator results with the experimental results. This section discusses the workpiece model and development of the grinding wheel model used in the computer simulator. Also, this section will present the simulation parameters used.

4.2.1 Workpiece Model

The development of the workpiece model was based on the approach of non-stochastically placing workpiece radials around the workpiece circumference. The number of radials was determined using the workpiece resolution parameter Res_w which is equal to the arc length in meters between any two consecutive radials. The simulator allowed the user to choose the workpiece resolution as required.

For a given workpiece radius R_w, the number of workpiece radials for a chosen workpiece resolution was determined using:

$$n_w = ceil\left(\frac{2\pi R_w}{Res_w}\right) \tag{4.2}$$

The "ceil" command in MATLAB rounds the answer to the nearest integer towards positive infinity. The workpiece radial angular spacing θ_{w_step} was determined using:

$$\theta_{w\_step} = \frac{2\pi}{n_w} \tag{4.3}$$

The workpiece model was formed by evenly spacing n_w radials at an angular spacing of θ_{w_step} around the workpiece circumference at a distance of the workpiece radius R_w from the workpiece center.

4.2.2 Grinding Wheel Model

First, a non-stochastic wheel model was designed by distributing the grains evenly about the circumference of the grinding wheel. The formation of this non-stochastic wheel model required calculating the number of grains on the grinding wheel.

The actual grinding wheel used in the experimental parts of this thesis had a grit number M=60 and a structure number S=5.

The nominal grain diameter d_g was calculated using Equation 2.1:

$$d_g = \frac{15.2}{60} \text{ mm} \tag{4.4}$$

The grain volume fraction V_g was calculated using Equation 2.2:

$$V_g = 0.02(32 - 5) \tag{4.5}$$

The torus method can be used to approximate the number of grains n_g in the non-stochastic model [16]:

$$n_g = \frac{3}{2}\pi V_g \left(\frac{d_s}{d_g} - 1\right) \tag{4.6}$$

where d_s is the nominal wheel diameter in meters.

Substituting Equation 4.4, Equation 4.5 and d_s = 406.4 mm in Equation 4.6 yielded:

$$n_g = 4080 \tag{4.7}$$

The knowledge of the number of grains was used to estimate the grain spacing L on the non-stochastic grinding wheel by using [16]:

$$L = \frac{\pi(d_s - d_g)}{n_g} \tag{4.8}$$

Substituting Equation 4.4, Equation 4.7 and d_s = 406.4 m in Equation 4.8 yielded:

$$L = 0.312 \text{ mm} \tag{4.9}$$

The angular spacing θ_{s_step} between the grains was estimated using:

$$\theta_{s\_step} = \frac{2\pi}{n_g} \tag{4.10}$$

A non-stochastic wheel model was, therefore formed with 4080 evenly-distributed grains. All of the grains were kept at an equal distance of 8 inches from the wheel center.

The non-stochastic model was modified to form a stochastic wheel model using the procedure discussed below. The grains in the non-stochastic model were randomly shaken within $0.1d_g$ mm in their radial positions towards and away from the wheel center using a uniform probability distribution. Figure 4.8 shows an example of shaking the protrusion heights of the grains from their nominal non-stochastic positions on the wheel model. Similarly, the angular positions of the grains were randomly shaken using a uniform distribution within θ_{s_step} radians. This shaking led to a thorough randomization of the grains and the formation of a non-grooved stochastic wheel model. The grooved wheel model was formed from this non-grooved stochastic wheel model by giving the first and the 2041th grain a positive protrusion height and subtracting the groove depth of 4 thou from the protrusion heights of all the grains from index 2042 to 4080. This adjustment led one half of the wheel model to be inactive replicating the 50% groove factor of the real grooved wheel. The formation of the grooved wheel model from the non-grooved wheel model is shown in Figure 4.9.

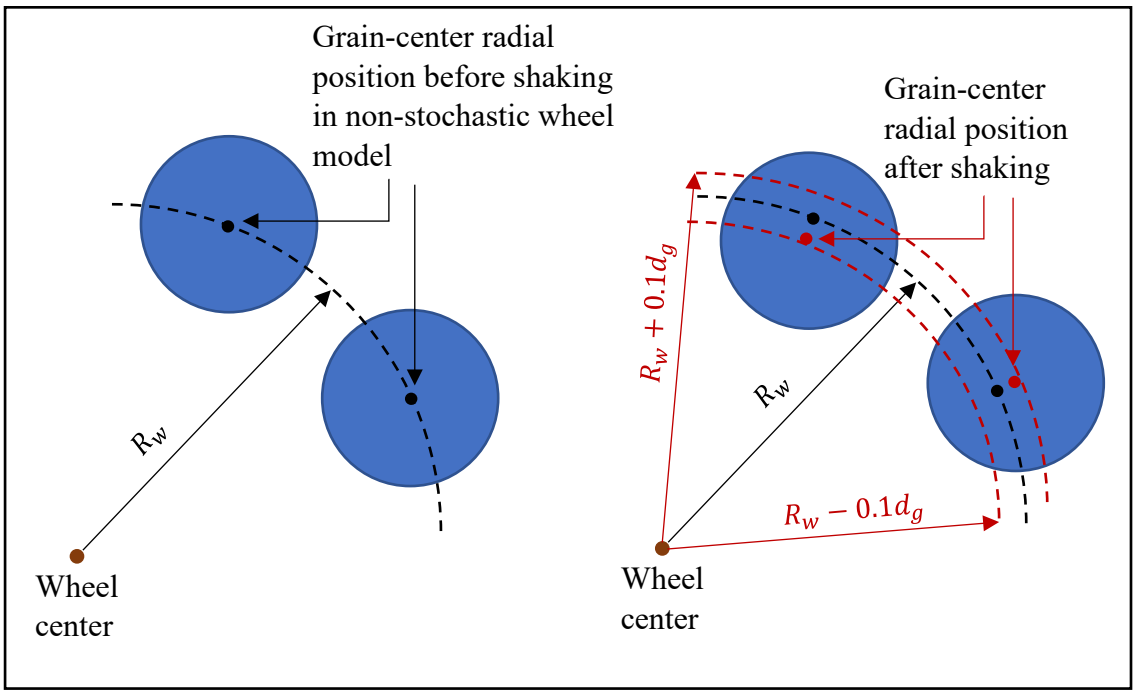

Figure 4.8: Shaking of grains in radial direction

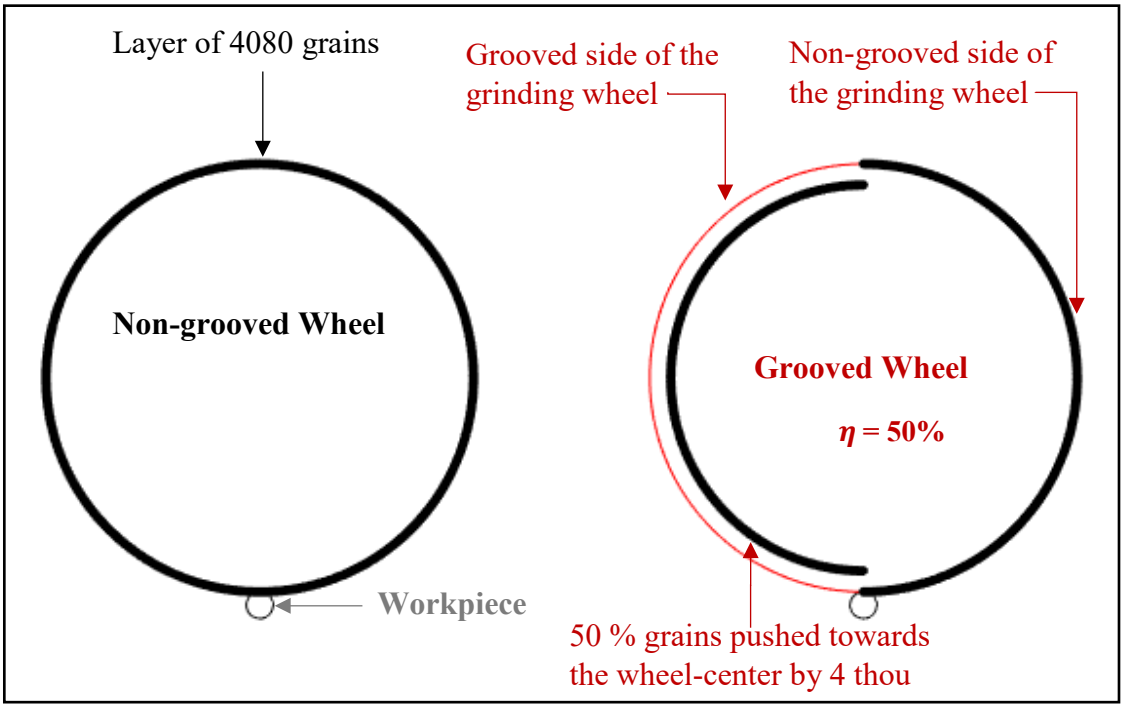

Figure 4.9: Formation of grooved wheel model from non-grooved wheel model

4.2.3 Simulation Parameters

Table 4.5 summarizes the parameters used for the computer simulation of the cylindrical grinding process. Note that the parameters given in Table 4.5 are used only when comparisons between simulation results and experimental results are being carried out.

The depth of cut (a)	76 µm
Groove depth	102 µm
Wheel surface speed (v_s)	21.2791 CW
Workpiece surface speed (v_w)	0.3325 CW
Workpiece resolution	1E-5 m
Workpiece diameter (d_w)	0.0254 m
Wheel diameter (d_s)	0.4064 m

Table 4.5: Simulation parameters

4.3 Conclusion

This chapter presented the apparatus and methodology used to conduct the experiments in this thesis. The development of the workpiece and wheel computer models was also discussed along with the simulation parameters used for comparison of simulation results with the experimental results.

Chapter 5

Cylindrical Plunge Grinding Experiments and Simulations

This chapter discusses the experimental and simulation results for three different studies conducted in cylindrical plunge grinding with and without the grooved wheel. The effect of integer speed ratios, non-integer speed ratios and dwell time on surface roughness, forces and power are considered. The observations noted in this chapter on surface roughness will be explained in Chapter 6.

5.1 Investigation of the Effect of Integer Speed Ratios on cylindrical Plunge Grinding Process

The first set of experiments were performed to investigate the effect of integer speed ratios on surface roughness, grinding power and forces.

5.1.1 Experimental Setup

Wheel dressing and grooving parameters are given in Table 4.2 and 4.3 respectively. Table 5.1 lists the specific grinding parameters for these experiments. First, a non-grooved grinding wheel was used for plunge grinding at every integer speed ratio within the range of 2 to 7. Then the same experiments were performed using a grooved grinding wheel having a 50% groove factor. All the non-grooved and grooved experiments were performed twice to confirm the repeatability of the results. The workpiece was only allowed to rotate one complete revolution in each experiment during the dwell time of the grinding process. This minimal dwell period is not the typical process but was done to eliminate the effects of dwell time on the results.

Speed ratios (S)	2-7
Wheel diameter d_s	15.75 in
Infeed rate f_r	12.7 µm/rev
Dwell time T_{dwell}	1 workpiece revolutions

Table 5.1: Grinding parameters for integer speed ratio experiments

Figure 5.1 shows typical variations in process forces during plunge cylindrical grinding. The forces are zero prior to grinding. Grinding is indicated by an increase in process forces. Since the wheel plunges at a constant rate into the workpiece, the grinding forces cause the workpiece to deflect away from the grinding wheel effectively reducing the depth of cut. As the grinding wheel continues to plunge into the workpiece, the workpiece deflection increases but not as fast as the grinding wheel is plunging into the workpiece. The forces increase until the commanded depth is reached. According to Dewar *et al.* [59], this phase of continuously increase in force is called the spark-in phase. Eventually a steady state is reached when the workpiece deflection and grinding force are approximately constant. In a typical cylindrical grinding cycle, the grinding wheel is kept at the final depth of cut for a certain period of time so that elastic recovery of the workpiece can occur. This last phase is called the spark-out phase.

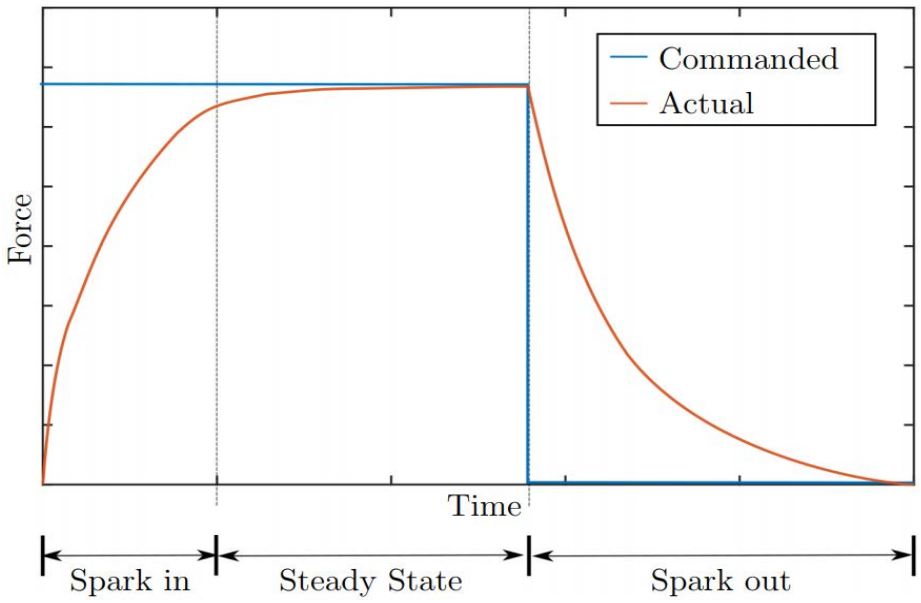

Figure 5.1: Variations in grinding force throughout the grinding cycle. Image source [4].

5.1.2 Results for Integer Speed Ratio Experiments and Simulations

5.1.2.1 Surface Topographical Results

Figure 5.2 shows the raw profile sample of the ground workpiece with the non-grooved wheel by plotting deviations in the workpiece surface around it's circumference. The profile shown was recorded using the 130 µm optical pen of the profilometer.

The scanned data of the profile was processed using the Professional 3D software to study the topographical properties of the ground workpieces. The curvature of the workpiece around its circumference in the scan data was removed using the form removal function in the software. The form-free profile was then used to determine the roughness value of the ground surface on the workpiece.

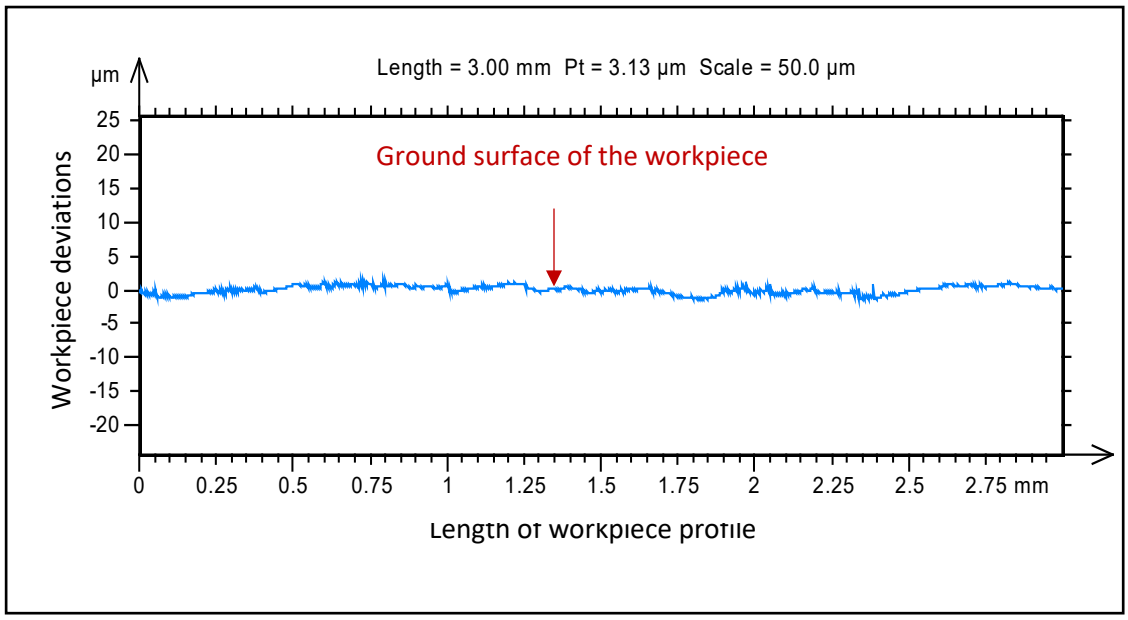

Figure 5.2: Raw profile sample of the workpiece ground with non-grooved wheel

Figure 5.3 compares the experimental roughness results for non-grooved wheel grinding with the simulation results obtained using the stochastic wheel model described in section 4.2.2. The roughness was measured along the circumference of the workpiece. The experimental surface roughness decreased with an increase in the speed ratio value. Similarly, the simulated surface roughness was observed to decrease as the speed ratio value increased. The experimental roughness was observed to be consistently higher than the simulated roughness for all the grinding experiments performed with a non-grooved wheel. However, the trend of the simulated data was almost identical to the experimental data suggesting that the simulator could be used to predict trends in the experiments if not the absolute values. Since the simulated values are consistently lower than the experimental values, it is likely that the simulated wheel model could have been improved by reducing the number of cutting edges to give a rougher surface.

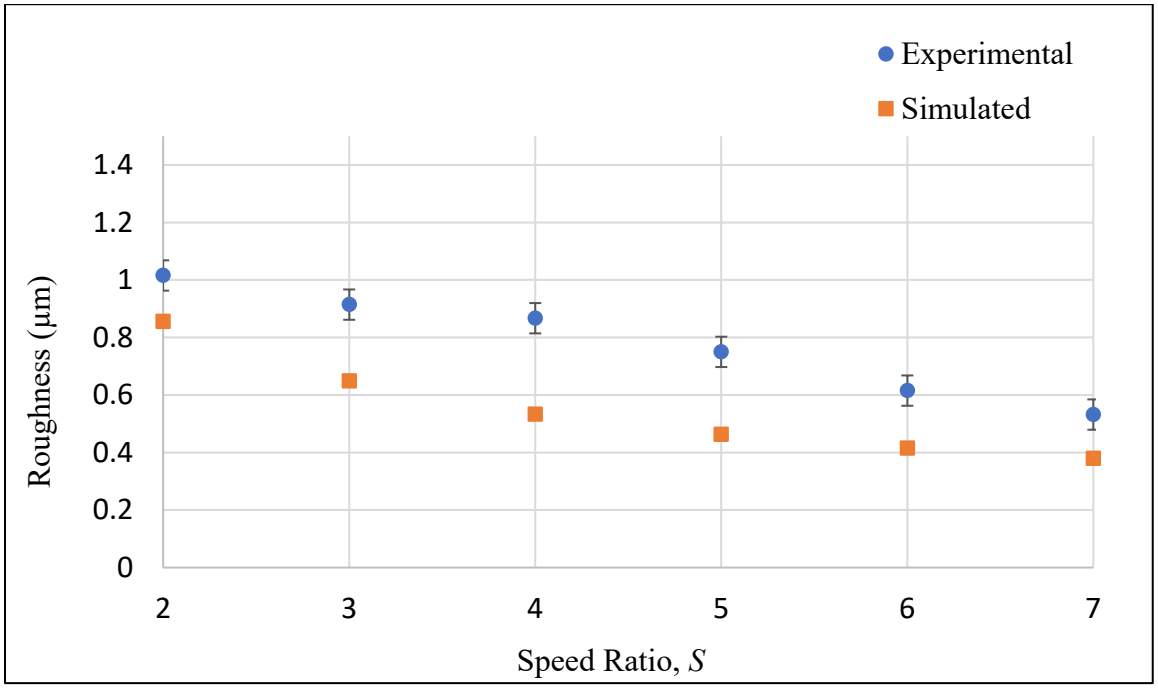

Figure 5.3: Comparison of experimental and simulated surface roughness for non-grooved wheel grinding at an integer speed ratio

Surface topographies of the workpieces ground with a grooved wheel were studied using the same procedure. Figure 5.4 shows all the workpieces after being ground at different integer speed ratios by the grooved wheel. Thread-like patterns were observed on all the workpieces.

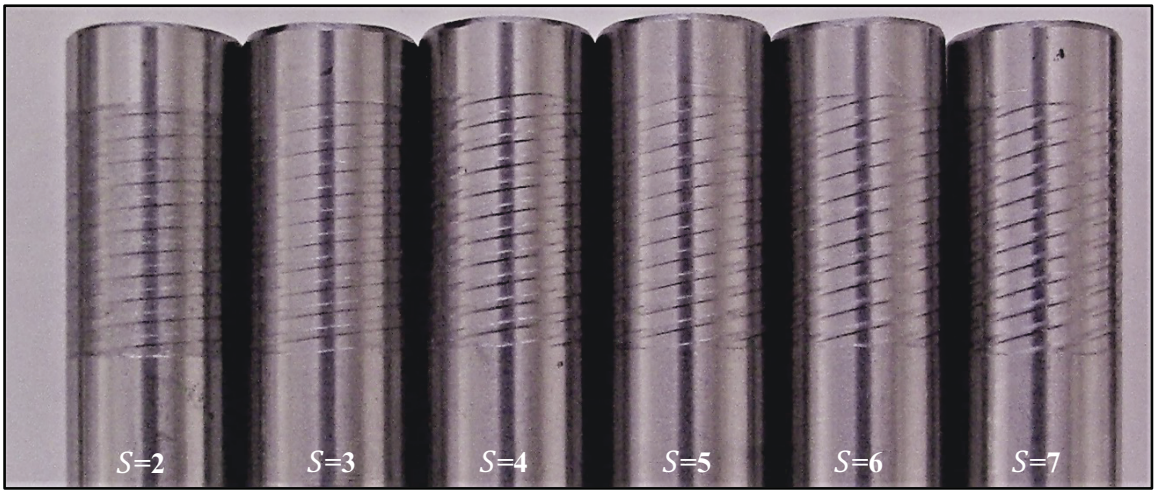

Figure 5.4: textured workpieces obtained after grinding with a grooved wheel

An area scan was taken to obtain a detailed 3D view of the workpiece surface. Figure 5.5 shows the 3D view of the textured workpiece that was ground at S=4. The threads clearly stand out from the rest of the workpiece surface.

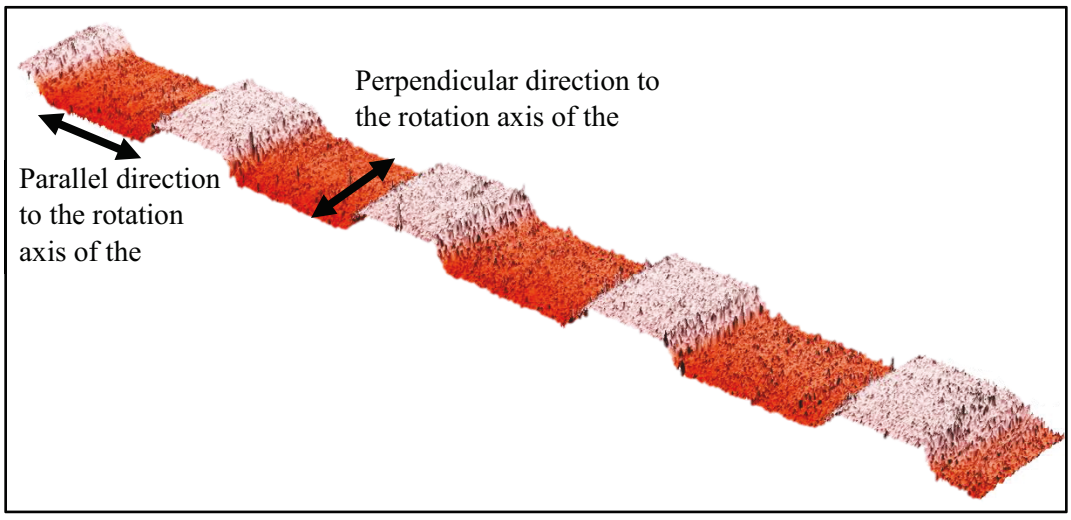

Figure 5.5: 3D rendering of the textured workpiece scan for S=4

Figure 5.6 shows an extracted profile from the area scan of the workpiece that was ground with a grooved wheel at S=4. This profile is in the direction parallel to the rotation axis of the workpiece. The intended depth of cut was 76.2 µm and the average achieved thread height was 65 µm. This difference can be attributed to the minimal dwell time used in the experiment. Note that, as previously described, during cylindrical grinding, the cantilevered workpiece deflects away from the grinding wheel due to the grinding forces. To reduce this deflection, the grinding wheel is usually allowed to continue cutting the workpiece at the desired final depth of cut for a specified dwell time effectively reducing the error in the depth of cut associated with workpiece deflection due to cutting forces. Since in this experiment set the workpiece was rotated just once in its dwell phase, the cut was not fully transferred to the workpiece as evident from the thread height.

The profile shown in Figure 5.6 suggests that the grinding wheel, which was created to have a groove factor of 50%, performed a cutting action on approximately 52.1% of the surface of the workpiece. This slight mismatch can be attributed to small errors incurred when actually grooving the grinding wheel as well as small speed ratio error during the grinding experiments. The presence of the groove texture on the workpieces from the grooved wheel experiments makes it possible to determine the depth of cut achieved since both the grooved surface and original (unground) surfaces are measured. Figure 5.7 shows the actual depth of cut for different integer speed ratios.

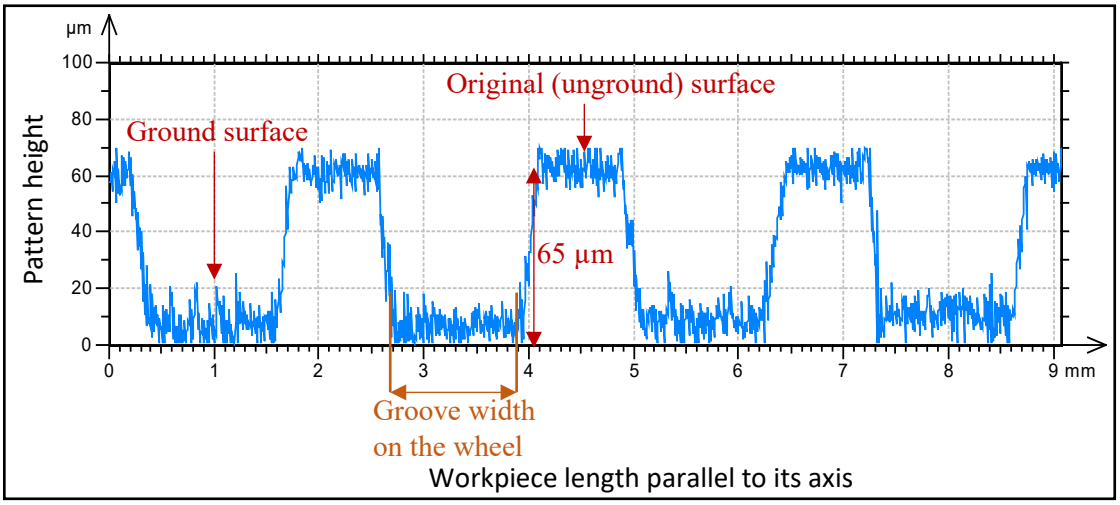

Figure 5.6: workpiece profile in the direction parallel to its rotation axis for grooved experiment at S=4

A horizontal line was fitted to the data. The achieved depth in grinding is slightly different for every integer speed ratio and there is no definite trend in the distribution of the achieved depth of cut for all the speed ratios ranging from 2 to 7. The average variations in actual depth of cut from the fitted line was 2.6 µm. The average difference between the desired and actual depth of cut was 10.3 µm. As previously noted, this difference was due to static deflection in the workpiece because of the minimal dwell time.

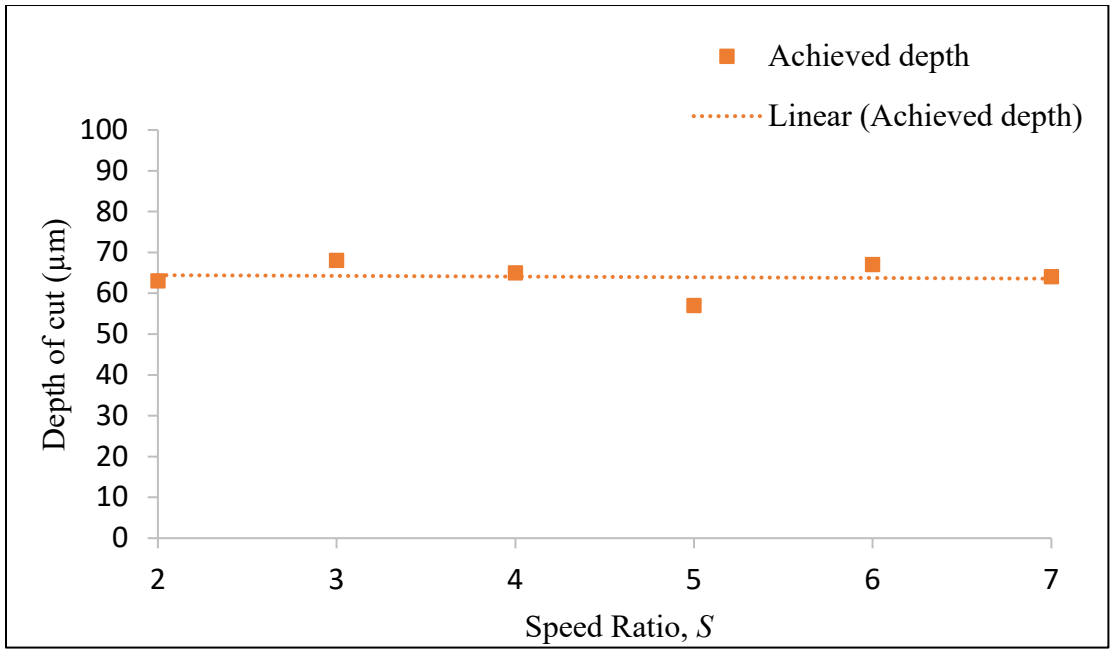

Figure 5.7: achieved depth of cut for grooved wheel grinding at different speed ratio

Referring to Figures 5.5 and 5.6, the spacing between the threads was also clearly defined and at regular intervals. The thread angle for all the workpieces with different speed ratios was measured. An example of thread angle measurement is shown in Figure 5.8. The figure represents an area scan of the workpiece ground at S=4. The inclination of the thread pattern is easily noticeable from the figure.

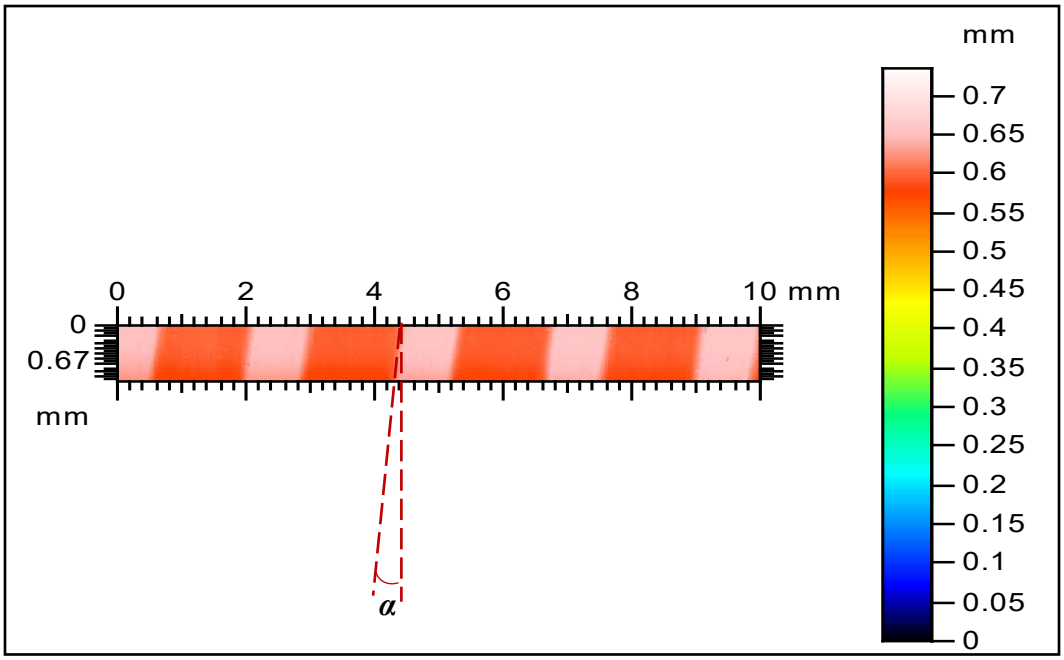

Figure 5.8: Area scan of the textured workpiece for S=4 showing measured thread angle

The angle α of the thread patterns is measured with respect to the axis perpendicular to the workpiece rotational axis as shown in Figure 5.8. As shown in the figure, α is measured to be 8.75 degrees for S=4.

Dewar *et al* [60] derived the following analytical equation for the angle of thread patterns α on the workpiece:

$$\alpha = tan^{-1}\left(\frac{f_g S}{\pi d_w}\right) \tag{5.1}$$

where f_g is the groove lead, S is the speed ratio and d_w is the workpiece diameter. Equation 5.1 was used to determine the theoretical pattern angle for each speed ratio in the current experiment set. The theoretical pattern angles for each speed ratio were compared with the experimentally-measured pattern angle as shown in Figure 5.9. Experimental and theoretical pattern angles increased with an increase in speed ratio values. The pattern angles varied from 3.3° for S=2 to 11.8° for S=7. The average difference between the theoretical and experimental pattern angle was only 3.2 %. This slight difference between

the theoretical and experimental pattern angle might be due to small errors in the experimental groove geometry.

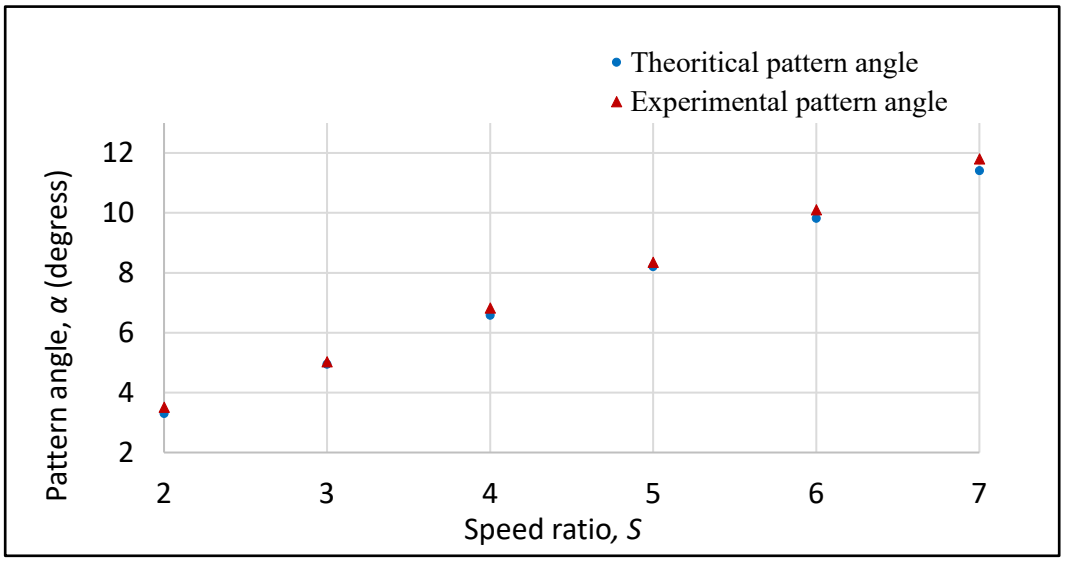

Figure 5.9: Comparison of theoretical and experimental thread angles for grooved grinding experiments at different integer speed ratios

Table 5.2 compares the thread number and thread width for experimental and simulated grinding at integer speed ratios. The number of threads around the circumference was equal to the respective speed ratios for all the experiments performed with a grooved wheel and at the same time, the ridge width became smaller with an increase in speed ratio because there was an increase in the number of ridges for the same length around the circumference of the workpiece.

(S)	Number of threads (experimental)	Number of threads (simulated)	Thread width in radians (experimental)	Thread width in radians (simulated)
2	2	2	1.33	1.15
3	3	3	0.79	0.70
4	4	4	0.54	0.48
5	5	5	0.38	0.35
6	6	6	0.28	0.25
7	7	7	0.19	0.16

Table 5.2: Thread details in experimental and simulated grinding results at integer speed ratios

The experiments performed with the grooved wheel were investigated for the surface roughness along the direction perpendicular to the axis of rotation of workpiece. Profiles of the ground surface of the workpiece between the ridges were taken to determine the roughness in the ground areas. Similar to the non-grooved wheel grinding experiments, the form was removed to straighten the curvature of the workpiece. The resulting surface roughness value R_a was determined at different sections of the workpiece and compared to the roughness values predicted by the computer simulator. The threaded ridges in the simulated profiles were removed and the surface roughness algorithm was run on the ground area of the workpiece so that the roughness values from the simulation could be compared with the experimentally measured values. Figure 5.10 (a) shows the simulated profile of a textured workpiece ground at S=4 using the grooved wheel model. The zero on the vertical scale represents the base of workpiece threads corresponding to the ground area on the workpiece.

A magnified view of one of the ground surfaces on the workpiece is shown in Figure 5.10 (b) and it can be seen that the simulated workpiece deviations in the ground zone are within 0 to 3 μm. The experimental and simulated roughness of this grooved zone can be compared.

Figure 5.11 compares experimental and simulated roughness for workpieces ground with a grooved wheel at different speed ratios. The simulator predicted a decrease of the workpiece surface roughness with an increase in the speed ratio value. Experimental roughness also decreased with an increase in speed ratio values. The simulated roughness was approximately 100 % higher for S=2 as compared to S=7, while the experimental roughness was 72% higher for S=2 in comparison to the surface roughness for S=7. This result suggests that the greater the integer speed ratio, the better the surface finish of the workpiece between the ridges.

a) simulated profile for S=4 showing threaded texture on the workpiece

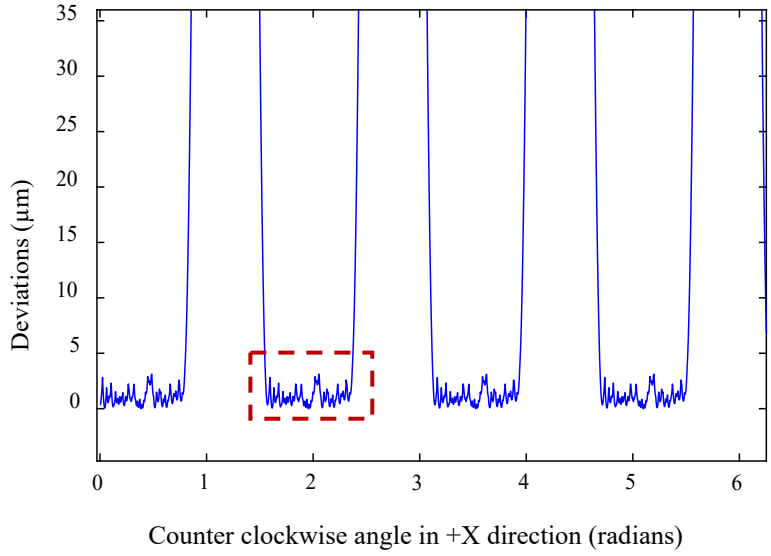

b) Magnified simulated view of the ground surface on the workpiece at S=4

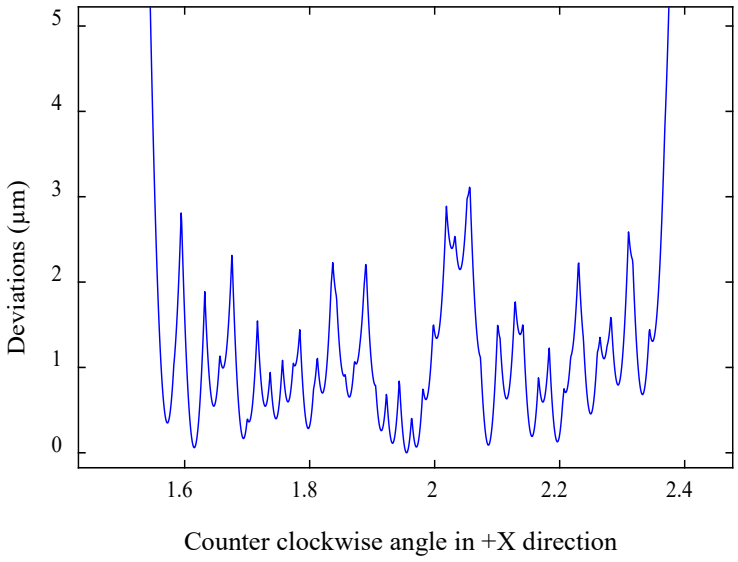

Figure 5.10: Simulated workpiece profiles for grooved wheel grinding at integer *S*

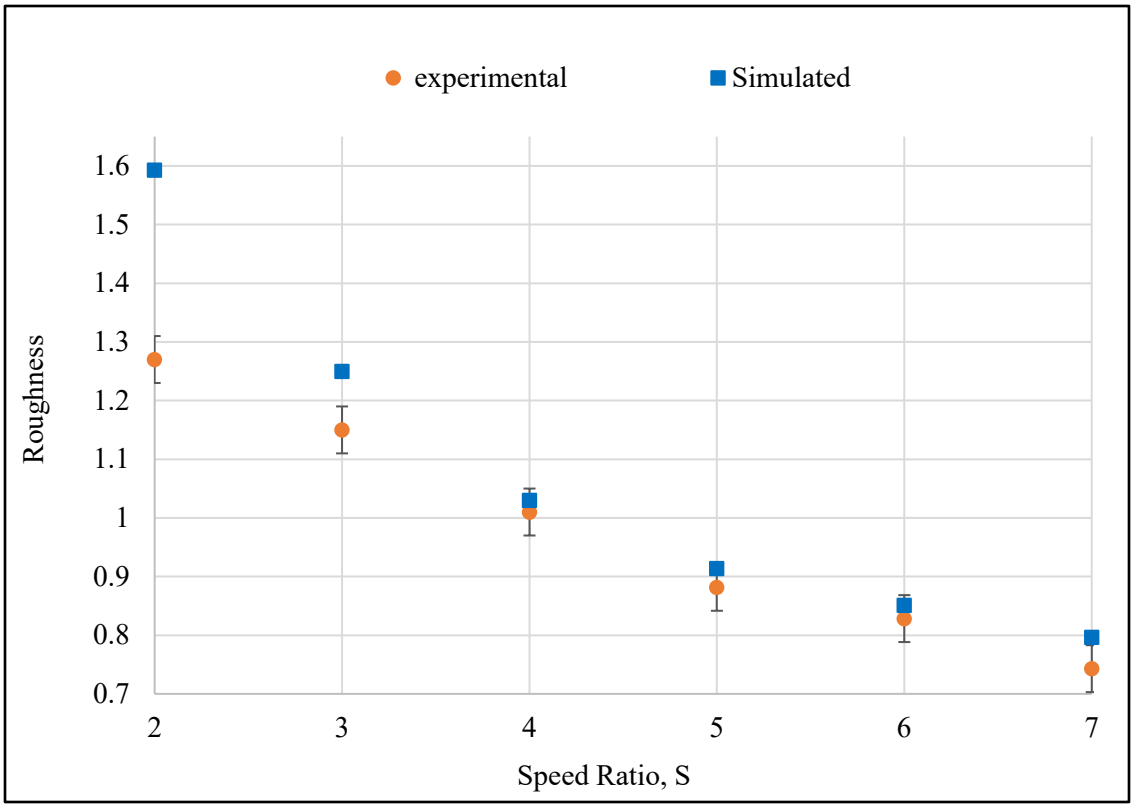

Figure 5.11: Comparison of experimental and simulated surface roughness for grooved wheel grinding at integer speed ratio

The experimental trends in surface roughness for grooved and non-grooved wheel grinding experiments were consistent with the trends in the simulator results. The difference between the experimental and simulation results is likely because the simulator captures only the kinematic effect and not any dynamic or cutting mechanics effects.

5.1.2.2 Process Forces and Spindle Power

Figure 5.12 shows the normal force, tangential force, and spindle power data for the grinding experiments performed with a non-grooved wheel at S =4. The data acqusition sampling frequency was 250 Hz. The noise in the raw data made it difficult to interpret the results; therefore, the raw force and power data were filtered using a low-pass Butterworth filter with a cut-off frequency of 2 Hz. The filtered force profiles (black) and spindle power profiles (orange) were used to understand various aspects of the grinding process. As

shown in Figure 5.12, the forces and power are zero before the grinding process begins. The grinding wheel cuts the workpiece until the commanded depth of cut. The normal force, tangential force and power increase until the commanded depth is reached. Note that steady-state cutting is not achieved. The Normal force, tangential force and spindle power are at their highest at the end of the spark in phase when the grinding wheel has reached the maximum depth. Since the dwell time, in this case, is effectively zero, the grinding wheel loses its contact with the workpiece immediately after the spark in phase is completed. This loss in contact results in the normal force, tangential force and spindle power values going down to zero immediately. The end point of the spark-in phase occurs when the force and power curve change their direction at the maximum point on the filtered curves and the corresponding force and power magnitudes at the end of the spark-in phase were referred to as the maximum forces and spindle power taken for the grinding experiment. It should be noted that the shapes of the normal force, tangential force and spindle power curves have similar characteristics.

Figure 5.13 shows the data processing of the normal force, tangential force, and spindle power for the grooved grinding experiment at S=4. A similar analysis to that of the non-grooved wheel grinding experiment was carried out for the normal force, tangential force and spindle power of the grooved wheel grinding experiments. Comparison of Figure 5.12 and Figure 5.13 shows that the grooved wheel required lower process forces and power for grinding at the same speed ratios compared to the non-grooved wheel.

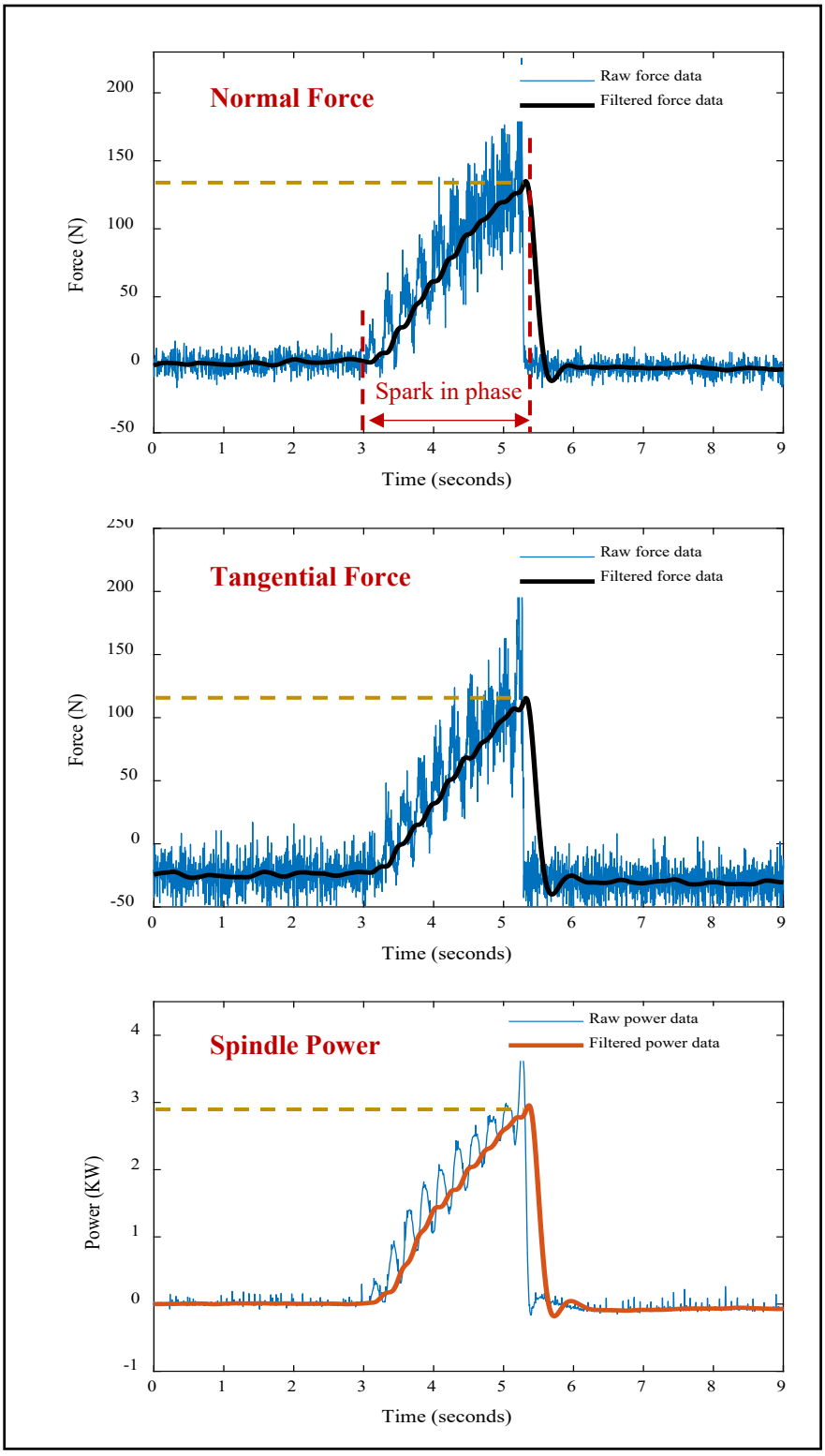

Figure 5.12: Processing of Normal force data, Tangential force data and Spindle power date for non-grooved wheel grinding experiment at *S*=4

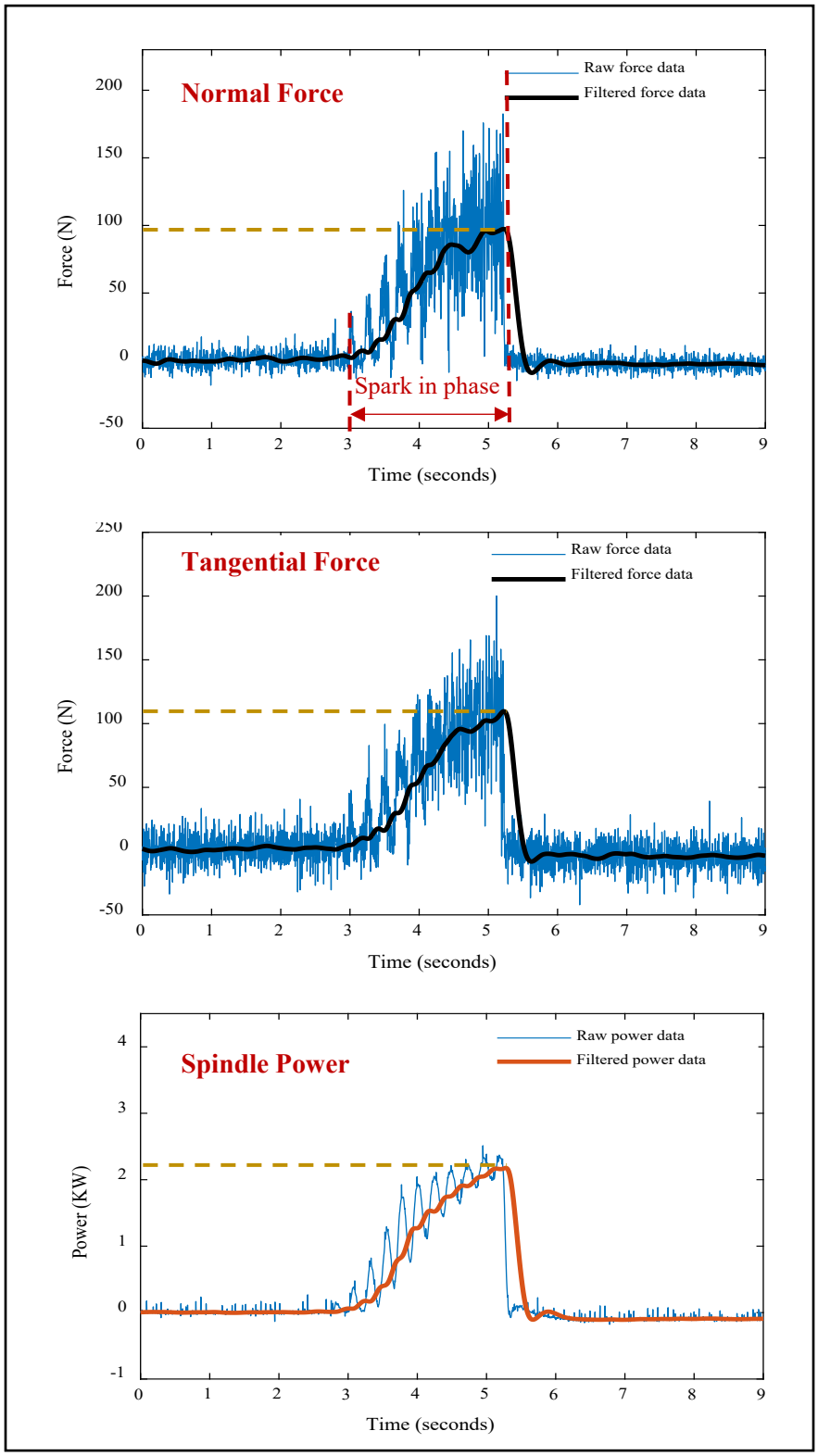

Figure 5.13: Processing of Normal force data, Tangential force data and Spindle power date for grooved wheel grinding experiment at *S*=4

Figure 5.14 shows a comparison of the maximum normal force F_n for the grooved and non-grooved grinding processes at different integer speed ratios. As evident from the figure, the maximum normal force decreases with an increase in the speed ratio for both grooved and non-grooved wheel experiments. This result can be related to the infeed rate during grinding. Since the infeed rate per revolution of the workpiece was kept constant at 12.7 µm, the grinding wheel travelled slower into the workpiece as the speed ratios increased. This is because the workpiece speed decreases as the speed ratio increases for the same wheel speed. The constant infeed rate per revolution meant that the wheel infeed speed reduced as the speed ratios increased. It is important to note that the maximum normal force appears to be always lower for the grooved experiments as compared to the non-grooved experiments for every integer speed ratio used in this study. On average, the maximum normal force for the grooved grinding wheel experiments was lower than the non-grooved grinding wheel experiments by 26.5%.

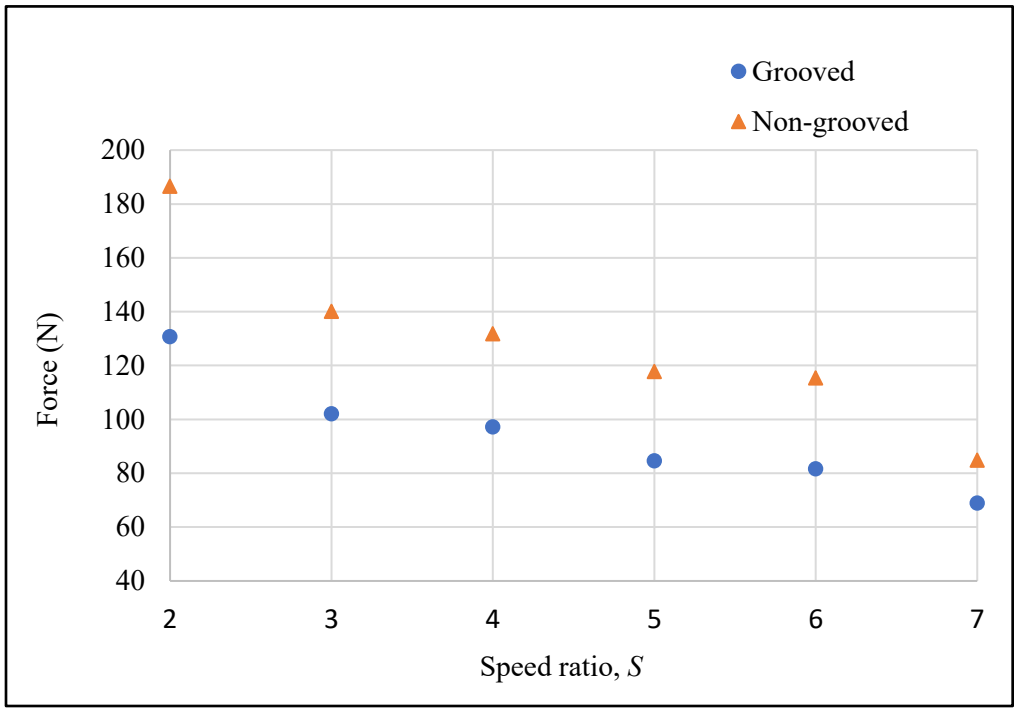

Figure 5.14: Comparison of Normal Force F_n for grooved and non-grooved experiments

Figure 5.15 shows a comparison of the maximum tangential force F_t for grooved and non-grooved grinding at integer speed ratios. Like normal force, there is a trend of decreasing tangential force with increase in a speed ratio. The decrease in the tangential force with increase in speed ratios can be linked to the constant infeed rate relative to the workpiece angular speed. Higher speed ratios have lower workpiece speeds and thus the wheel travels slower into the workpiece thereby reducing the tangential force. Also, the tangential forces for the grooved grinding experiments are lower than the non-grooved grinding experiments. On average, the maximum tangential force for the grooved grinding wheel experiments was lower than the non-grooved grinding wheel experiments by 20.2%.

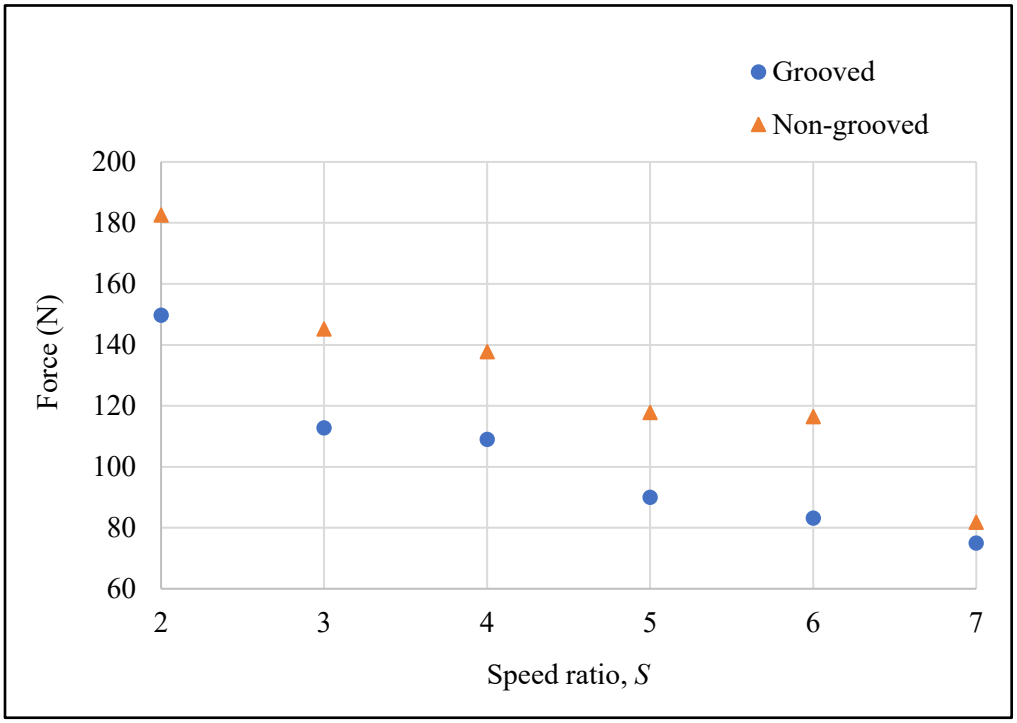

Figure 5.15: Comparison of Tangential Force F_t for grooved and non-grooved experiments

Figure 5.16 shows a comparison of maximum spindle power for both grooved and non-grooved grinding at different integer speed ratios. The maximum spindle power decreases with an increase in speed ratio for both grooved and non-grooved wheel experiments. Since the power curve had similar characteristics to the forces curves, it can be said that the lower wheel infeed speed, like in the case of the normal and tangential forces, is responsible for the decreasing trend in spindle power with an increase in speed ratio. It is important to note that the maximum spindle power is always lower for grooved experiments when compared to the non-grooved experiments for every integer speed ratio used in this study. On average, the maximum spindle power for grooved grinding wheel experiments was lower than the non-grooved grinding wheel experiments by 21.5%.

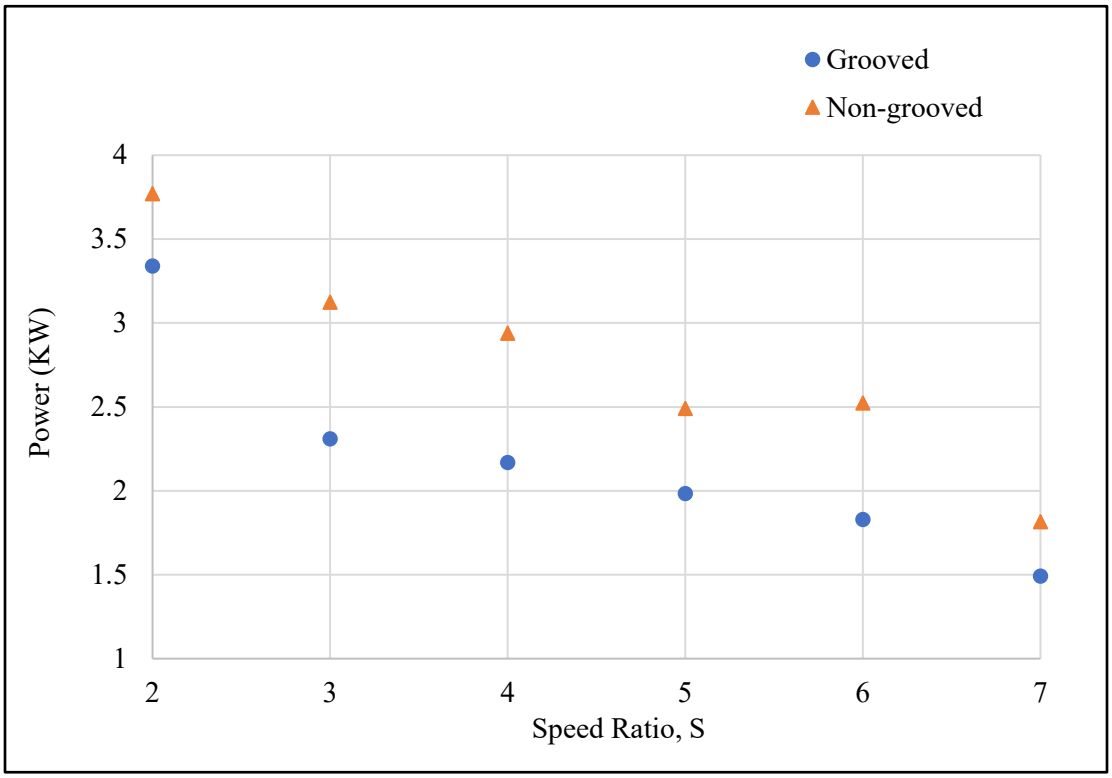

Figure 5.16: comparison of spindle power for grooved and non-grooved wheel grinding experiments at *S*=4

5.1.3 Conclusions for Integer Speed Ratio Study

This study was intended to investigate the effects of integer speed ratios for the cylindrical grinding process.

The major difference observed between the grooved and non-grooved experiments was the resulting thread-like texture on the workpieces when grinding with the grooved wheels. The topographical study of the patterned workpiece confirmed the kinematic analysis proposed by Dewar *et al* [60]. The observation of the textures on the workpieces for grooved grinding was also found to be consistent with the predictions from the 2D cylindrical grinding simulator. In addition, the simulator predictions of surface roughness for the grooved and non-grooved experiments were also found to be within 7.5% and 30% respectively of the experimental results and the overall trend across a range of different speed ratios was similar.

Grinding with the grooved wheel showed significant improvements in the force and spindle power requirements of the system as compared to grinding with the non-grooved wheel. Improvements in normal force, tangential force and power for grooved wheel grinding are summarized in Table 5.3.

Improved process parameters	**Improvements due to grooved wheel**
Normal Force, F_n	26.5 %
Tangential Force, F_t	20.2 %
Power, P	21.5 %

Table 5.3: Improvements in cylindrical grinding for grooved wheel grinding.

5.2 Investigation of the Effect of Dwell Time on Workpiece Surface roughness on Cylindrical Plunge Grinding Process

This section studies the effect of dwell time on the surface roughness for speed ratios 4.22 and 4.5. A series of simulations showed that S=4.5 yielded far higher roughness than other non-integer speed ratios and S=4.22 was found to be among the best surface-finish-yielding speed ratios. Hence these speed ratios were chosen to investigate how dwell time affected the grinding at good and bad surface-finish-yielding speed ratios. Both speed ratios were used in grinding with grooved and non-grooved wheels in simulations and experiments. These preliminary experiments were used to determine the suitable value of dwell time for the final set of experiments discussed in the next section using non-integer speed ratios. The forces and power curve characteristics were studied and the experimental roughness at both speed ratios were compared to the simulated roughness for grooved and non-grooved grinding.

5.2.1 Experimental and Simulator setup and preliminary discussion

The dressing and grooving parameters for these experiments were the same as the parameters given in Table 4.2 and 4.3. Table 5.4 lists the grinding parameters for these experiments.

Speed ratios (S)	4.22 and 4.5
Wheel speed ω_s	~1000 (adjusted slightly to achieve correct speed ratio)
Wheel diameter d_w	15.5 in
Infeed rate f_r	1.27 µm/rev
Dwell times used	0, 2.5, 5, 7.5, 10, and 12.5 seconds

Table 5.4:Grinding parameters for integer speed ratios experiments

First, a non-grooved wheel was used for plunge grinding at S=4.22 for six different dwell periods starting from zero (no dwell) to 12.5 seconds, followed by a similar set of experiments for S=4.5. Then the same experiments were performed using a grooved wheel having a groove factor of 50%. All of the non-grooved and grooved experiments were then repeated again to ensure repeatability of the results.

The cylindrical grinding computer simulator uses the number of revolutions of the grinding wheel as a measure of grinding time. The corresponding number of grinding wheel revolutions R_G for each dwell time value T_{dwell} can be calculated using:

$$R_G = \left(\frac{\omega_s \times T_{dwell}}{60}\right) \tag{5.2}$$

where ω_s is the grinding wheel angular speed (RPM) and T_{dwell} is the dwell time in seconds. Conversion of sample dwell times in seconds to their corresponding number of grinding wheel revolutions is shown in Table 5.5. Since the simulator uses only integer values of R_G, the calculated values of R_G are rounded up to the next integer in Table 5.5.

T_{dwell}	R_G
2.5	~ 42
5	~ 84
7.5	125
10	~167
12.5	~209

Table 5.5: Conversion of dwell time in grinding to the equivalent number of wheel revolutions

It should be pointed out that a zero dwell time used in the experiments will be, given the nature of the kinematic simulator, considered to be equivalent to one grinding wheel revolution in the simulator.

5.2.2 Results for Dwell Time Study

5.2.2.1 Surface Topographical Results

The workpiece surface roughness in the direction perpendicular to the workpiece rotational axis will be compared for both simulated and experimental surface topographies for grooved wheel and non-grooved wheel grinding.

Figure 5.17 compares the simulated workpiece surface roughness at S=4.22 with the simulated roughness at S=4.5 for both grooved and the non-grooved grinding for all of the dwell times listed in Table 5.5. A dwell time T_{dwell} of 0 seconds has been considered to be equivalent to 1 grinding wheel revolution R_G within the simulator for the purpose of illustrating the trends in surface roughness with the number of grinding wheel revolutions. It can be seen in the figure that the predicted ground surface roughness for S=4.5 with both the grooved wheel and non-grooved wheel grinding remained the same for all the dwell times after 0.55 seconds (corresponding to 9 grinding wheel revolutions). When S=4.5, the simulated surface roughness was lower for the non-grooved wheel grinding experiments as compared to the grooved wheel grinding experiments. When S=4.22, the simulated surface roughness of the workpiece in both the grooved and non-grooved grinding decreases consistently with an increase in dwell time. The predicted workpiece surface roughness using the grooved wheel was also initially higher than when using the non-grooved wheel for S=4.22 but gradually converge as the dwell time increases. The predicted workpiece surface roughness for S=4.22 decreases minimally from R_G = 167 to 209 for both the grooved and the non-grooved wheel.

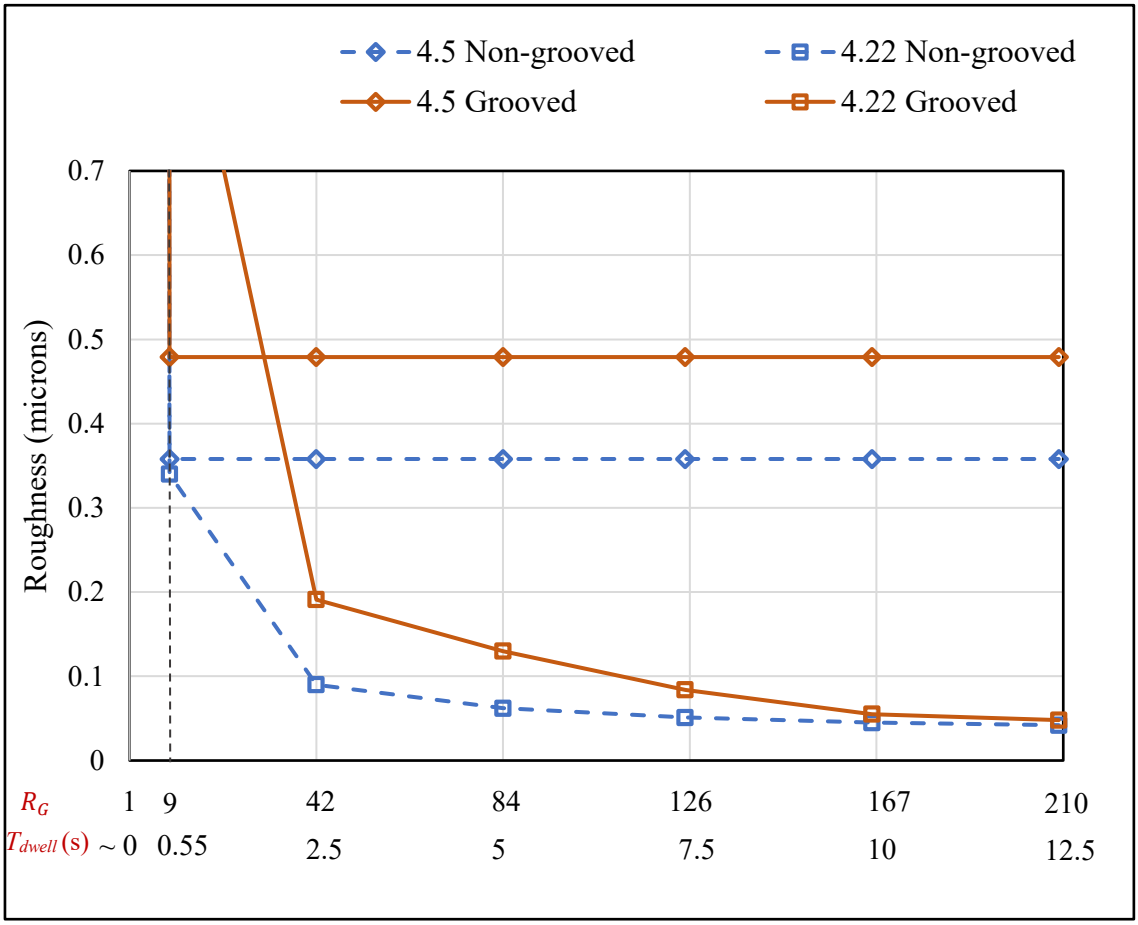

Figure 5.17: Comparison of simulated roughness for grooved and non-grooved grinding at *S*=4.22 and *S*=4.5

In order to understand the reason for the consistency in surface roughness for S=4.5 after 9 revolutions as seen in Figure 5.17, we will look at the progression of the workpiece surface profile with each revolution using the 2D cylindrical grinding simulator.

Figure 5.18 shows the simulated workpiece profiles for S=4.5 as the workpiece is ground for different numbers of wheel revolutions. These profiles were generated using a grooved wheel model. From the comparison of Figure 5.18 (a) and (b), it is clear that new cuts are imparted by the wheel on the workpiece by material removal on each subsequent wheel revolution up until the 9th wheel revolution (corresponding to a dwell time of 0.55 seconds). The predicted workpiece surface roughness reduces with every revolution of the grinding wheel until the 9th revolution. Figure 5.18 (h) shows the workpiece profile after

42 wheel revolution of the grinding wheel. As evident from Figure 5.18 (g) and Figure 5.18 (h), the grinding wheel did not remove any material from the workpiece after the 9^{th} grinding wheel revolution and the surface roughness of the workpiece profile after 42 wheel revolution was the same as the surface roughness of the workpiece profile after the 9^{th} grinding wheel revolution. This observation means that the grinding wheel stopped removing material from the workpiece after the 9^{th} grinding wheel revolution. Simulations for the same S=4.5 speed ratio using a non-grooved grinding wheel are shown in Figure 5.19. Similar to the grooved wheel case, the non-grooved grinding simulations showed that the workpiece profiles and surface roughness ceased to change after 9 grinding wheel revolutions.

Figure 5.20 and Figure 5.21 show simulated workpiece profiles for the grooved and the non-grooved grinding wheel at S=4.22, respectively. It can be observed that the workpiece profile changes continuously for all of the wheel revolutions considered and shows a continuously improved surface finish as the dwell time increases.

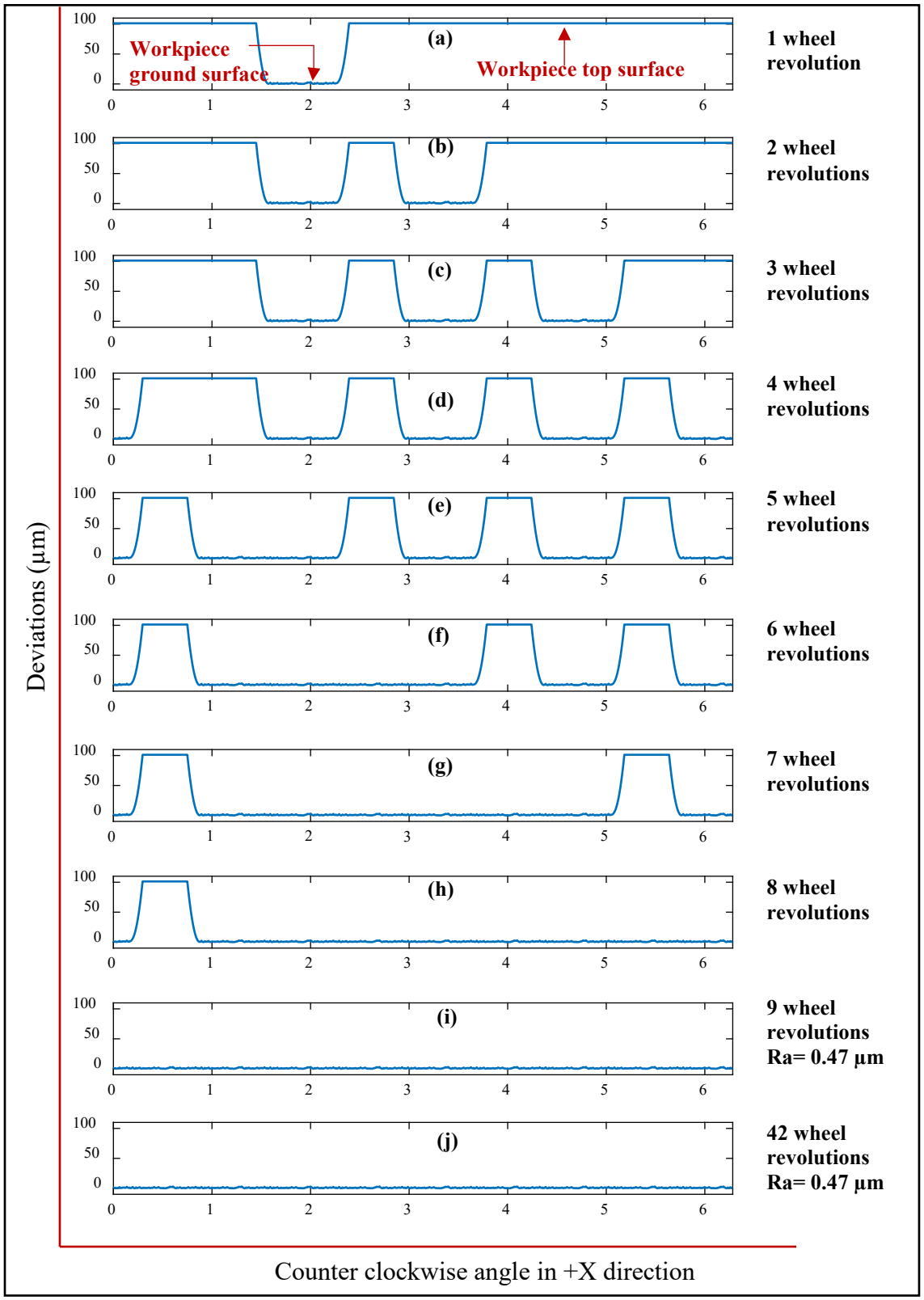

Figure 5.18: Simulated workpiece profiles for S=4.5 using a grooved grinding wheel

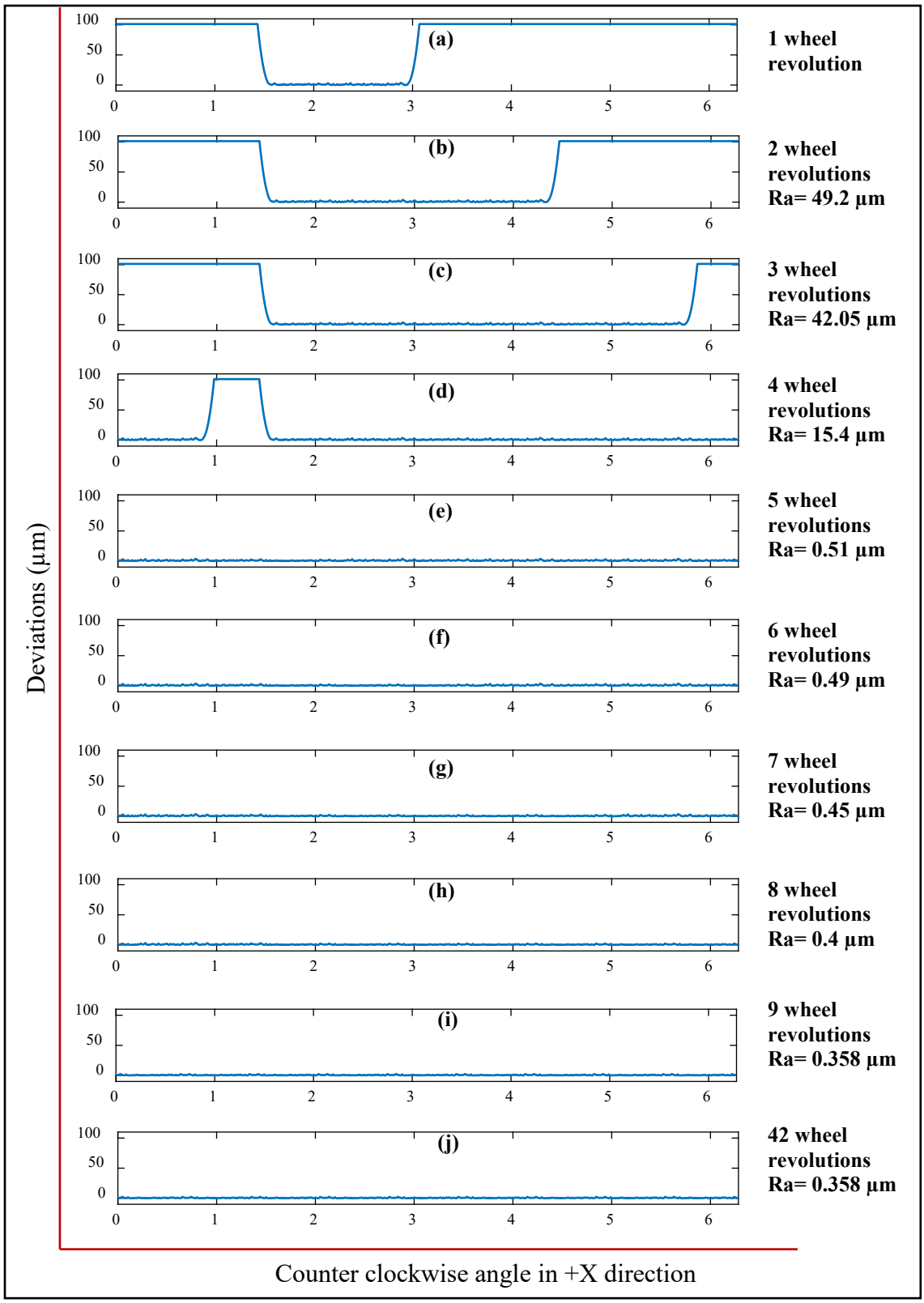

Figure 5.19: Simulated workpiece profiles for S=4.5 using a non-grooved grinding wheel

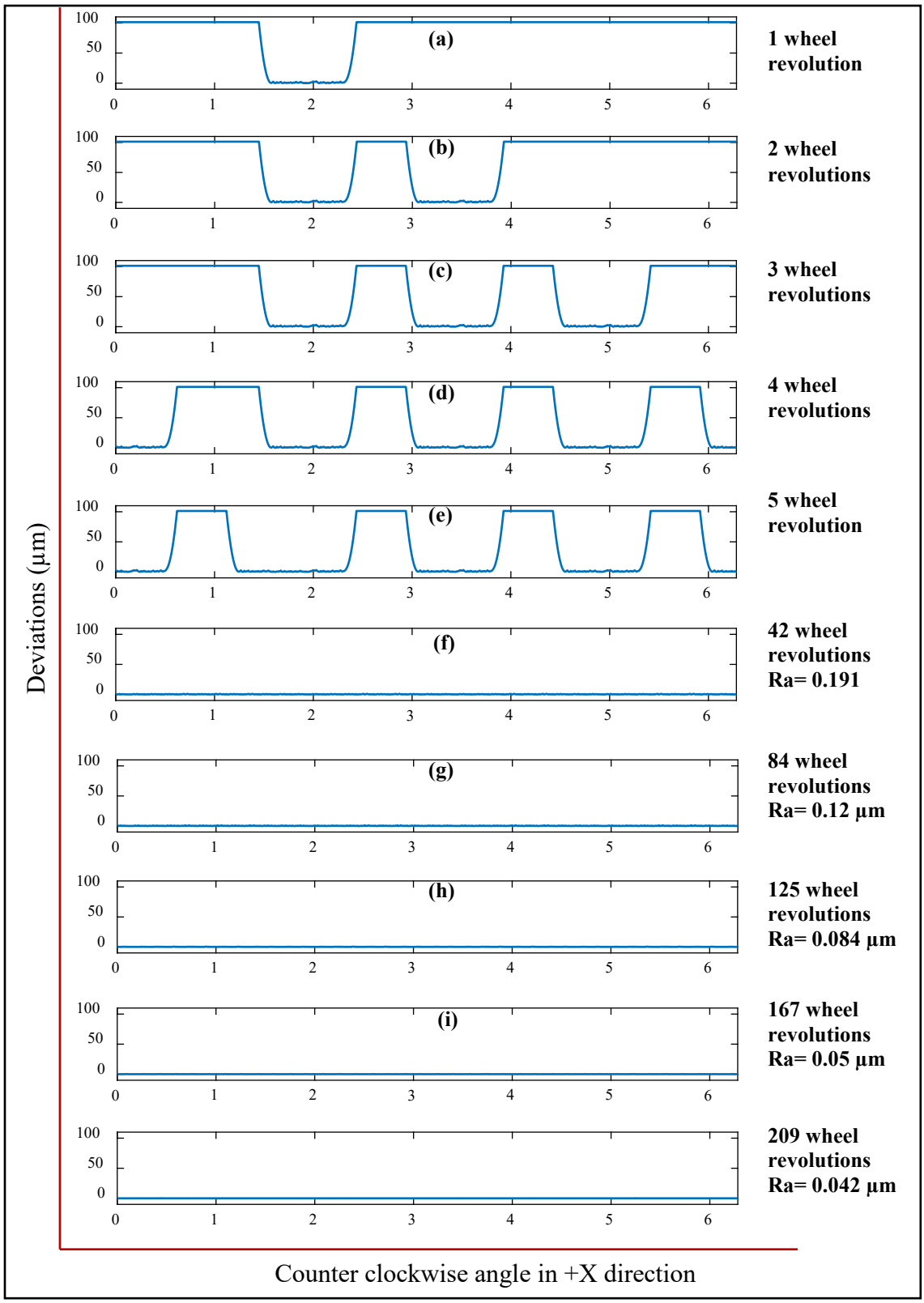

Figure 5.20: Simulated workpiece profiles for S=4.22 using a grooved grinding wheel

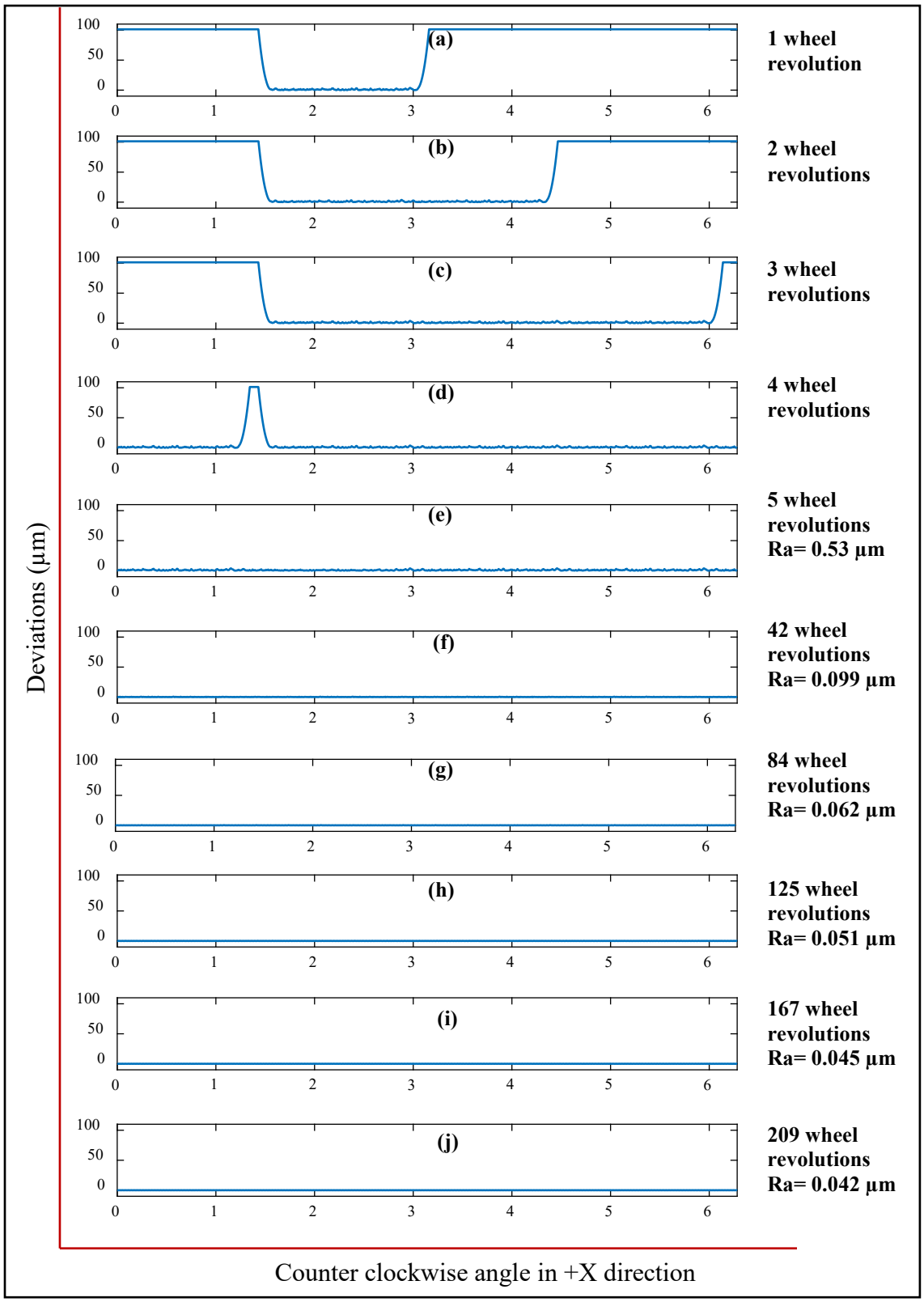

Figure 5.21: Simulated workpiece profiles for S=4.22 using a non-grooved grinding wheel

To understand the differences observed in the workpiece surface roughness when using a grooved and non-grooved grinding wheel at S=4.5 (shown in Figure 17), the workpiece profiles of both cases are compared in Figure 5.22. This figure has been annotated to show that the peaks of the workpiece deviations for the grooved wheel grinding (Figure 5.22 (a)) are greater than the peaks of workpiece deviations for non-grooved wheel grinding (Figure 5.22 (b)) because of insufficient cutting which causes the surface roughness to be different.

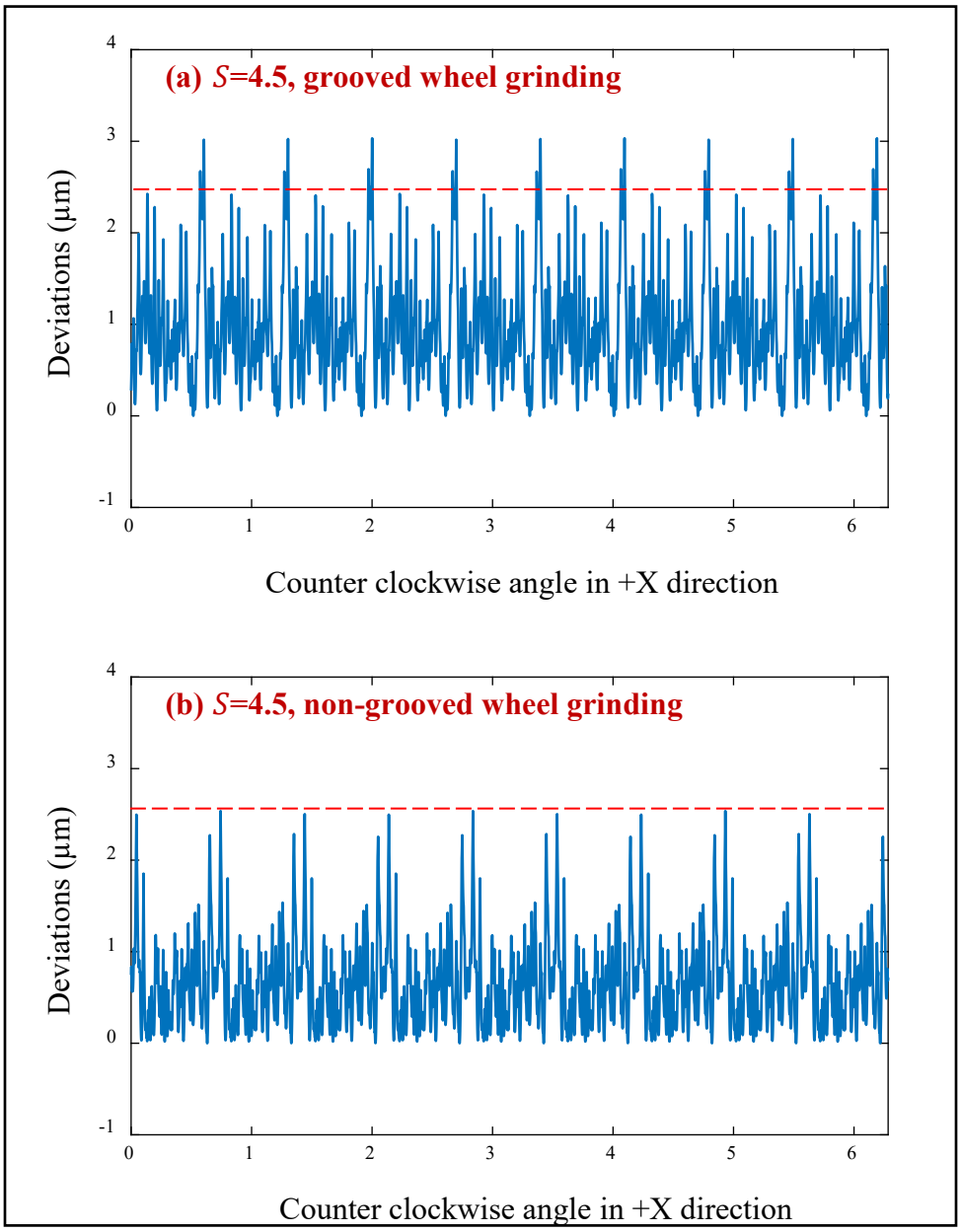

Figure 5.22: comparison of simulated workpiece profiles for S=4.5

Figure 5.23 compares the corresponding experimental surface roughness of the workpieces obtained after grooved and non-grooved wheel grinding at S=4.22 and S=4.5. The surface roughness of the workpiece was measured around its entire circumference. As can be seen in Figure 5.23, there is a sharp decrease in the surface roughness from R_G= 0 to 42 for the workpieces ground with a grooved grinding wheel for both S=4.22 and S=4.5. The overall trend for the two speed ratios using both grooved and non-grooved wheels is that the experimental surface roughness decreases as the dwell time increases. However, the improvement in the surface finish is very small in all cases after a dwell time of 10 seconds suggesting that there is no significant advantage in continuing to grind beyond 10 seconds of dwell period with the current setup conditions. These observations are consistent with the predictions from the simulator (Figure 5.17) where the simulated

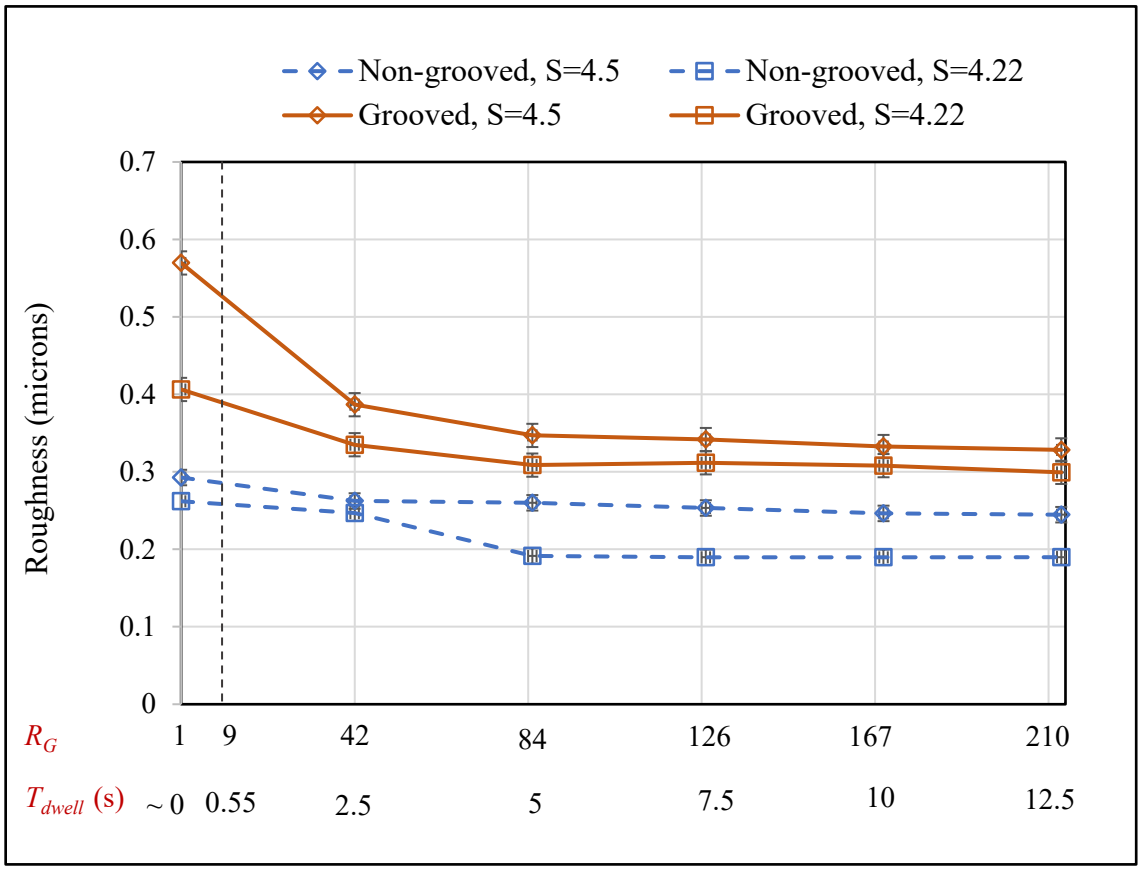

Figure 5.23: Comparison of experimental surface roughness for grooved and non-grooved wheel grinding at S=4.22 and S=4.5

roughness did not improve significantly after 10 seconds of dwell time for the grooved and the non-grooved grinding wheel at S=4.22 and S=4.

A comparison of Figure 5.17 and Figure 5.23 shows a difference in the trend of workpiece roughness for grooved and non-grooved grinding cases of S=4.5. The experimental surface roughness for both the grooved and the non-grooved grinding cases does not remain consistent after R_G= 9, unlike the simulation predictions. This difference between the experimental and the simulated workpiece surface roughness for S=4.5 could be attributed to various mechanical factors not modelled in the simulator such as vibrations, fluctuations in wheel and workpiece speeds, and misalignments in the workpiece setup. In addition, the simulator assumes cutting right from the first revolution of the grinding wheel at the commanded depth while the grinding wheel in practice takes a certain number of wheel revolutions to reach the commanded depth. Finally, another important factor that could contribute to the differences in the simulated and experimental roughness is the differences in the grain distribution and grain spacing between the real grinding wheel and the simulated grinding wheel model.

The simulation and experiment results for S=4.5 and 4.22 show that a dwell time of up to 10 seconds improves surface finish. Grinding beyond 10 seconds of dwell showed very small improvements in surface finish; therefore, a dwell time of 10 seconds was selected for the remaining non-integer speed ratio simulations and experiments.

5.2.3 Conclusions for Dwell Time Study

The workpiece topographies were investigated for two different speed ratios (4.22 and 4.5) for grooved and non-grooved wheel grinding using simulations and experiments. The grooved wheel consistently yielded a rougher surface finish compared to the non-grooved wheel. In comparison to S=4.22, S=4.5 was found to yield a rougher workpiece surface finish in both experimental and simulation analysis of the workpiece surface topography. One important and consistent observation from the experimental and simulation analysis was that the surface roughness ceased to improve beyond 10 seconds of dwell time.

The topographical analysis showed that a dwell time of 10 seconds would serve as a common basis for investigating the effect of non-integer speed ratios using grooved and non-grooved wheels in cylindrical grinding conducted in section 5.3.

5.3 Investigation of the Effect of Non-Integer Speed Ratios on Cylindrical Plunge Grinding Process

The purpose of this study was to determine the effect of non-integer speed ratios on the workpiece surface roughness, process forces and spindle power in cylindrical grinding.

5.3.1 Experimental Set up

The wheel dressing and grooving parameters used for this set of experiments are given in Table 4.2 and 4.3 respectively. The grinding parameters for these experiments are given in Table 5.6. The dwell time was kept at 10 seconds for all the experiments.

Wheel speed ω_s	~1000 RPM
Wheel diameter d_s	15.45 in
Infeed rate f_r	1.27 µm/rev
Dwell time T_{dwell}	10 seconds

Table 5.6: Grinding parameters for multiple speed ratios experiments

Grinding was performed for all the speed ratios given in Table 5.7. The workpiece speed was varied according to the speed ratios. A 50% groove factor grinding wheel and a non-grooved grinding wheel was used. The roughness of the resulting workpiece surface, and corresponding grinding forces and power were measured.

Speed ratio (S)	Workpiece angular speed (ω_w) RPM
4.04	247.52
4.125	242.42
4.22	236.96
4.25	235.29
4.41	226.75
4.5	222.22
4.59	217.86
4.75	210.52
4.78	209.2
4.875	205.12
4.96	201.61

Table 5.7: List of speed ratios and their corresponding workpiece angular speeds

5.3.2 Results for non-integer speed ratio study

5.3.2.1 Surface roughness results

The surface roughness around the circumference of the workpiece was measured. The experimental roughness was compared with the simulated roughness obtained using the stochastic wheel model discussed in Section 4.2.2. The simulations were run at speed ratios ranging from 4 to 5 in increments of 1/128. The roughness results of the experiments performed with the speed ratios in this experimental set were superimposed on the simulation results.

Figure 5.24 plots the experimental and the simulated roughness results for grooved wheel grinding at different speed ratios. Since the range of absolute values of experimental roughness was very small as compared to the range of predicted roughness values from the simulator, a two-sided plotting technique was implemented using different scales on the left-hand side and right side of the graph. The left-side vertical axis represents simulation results while the right-side vertical axis represents experimental results. In all cases, the

surface roughness was lower for non-integer speed ratios as compared to the integer speed ratios of 4 and 5. The overall trends in simulation and experimental roughness were very similar. For example, from Figure 5.24, the experimental and simulated surface roughness was highest for S=4.5 and the workpieces ground with S=4.25 and S=4.75 were found to be second highest in their surface roughness values. The simulated surface roughness at S=4.125, 4.375, 4.625, and 4.875 was third highest since their peaks were smaller than S=4.25 and 4.75 and S=4.5. The corresponding grinding experiments performed at S=4.125 and 4.875 yielded lower surface roughness values as compared to the two highest roughness value levels at S=4.25,4.5 and 4.75 but higher roughness values than all the other speed ratios in the experiment set. From the experiment set, the speed ratio of 4.22 produced the best surface finish of all other speed ratios tested.

Figure 5.25 compares the trends between the experimental and the simulated roughness for non-grooved wheel grinding at non-integer speed ratios between 4 and 5. Once again, the trends between the simulation and experimental roughness results were similar. The grooved wheel grinding roughness values were higher than the non-grooved wheel grinding values. Again, for non-grooved grinding also, S=4.5 yielded highest surface roughness for both experimental and simulated cases compared to other speed ratios. The distribution of peaks was similar to the non-grooved case in simulation and experimental roughness results. S =4.78 produced the best surface finish among all other speed ratios in the experimental set. Comparison of Figure 5.24 and Figure 5.25 shows that the surface roughness for all the speed ratios increased for grooved wheel grinding experiments and simulations as compared to the non-grooved wheel grinding operations.

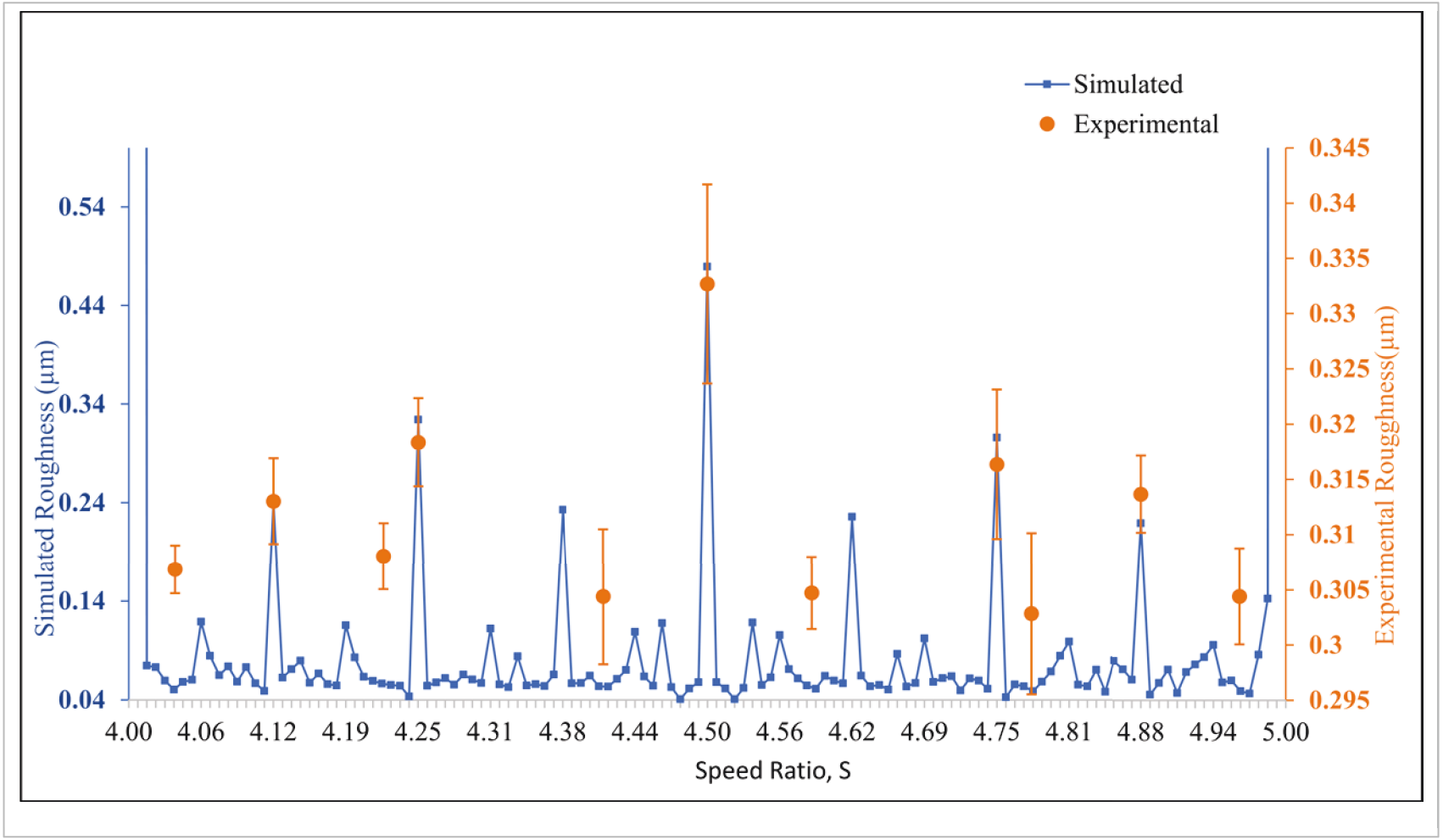

Figure 5.24: Comparison of trends between experimental and simulated surface roughness at different speed ratios using a grooved grinding wheel

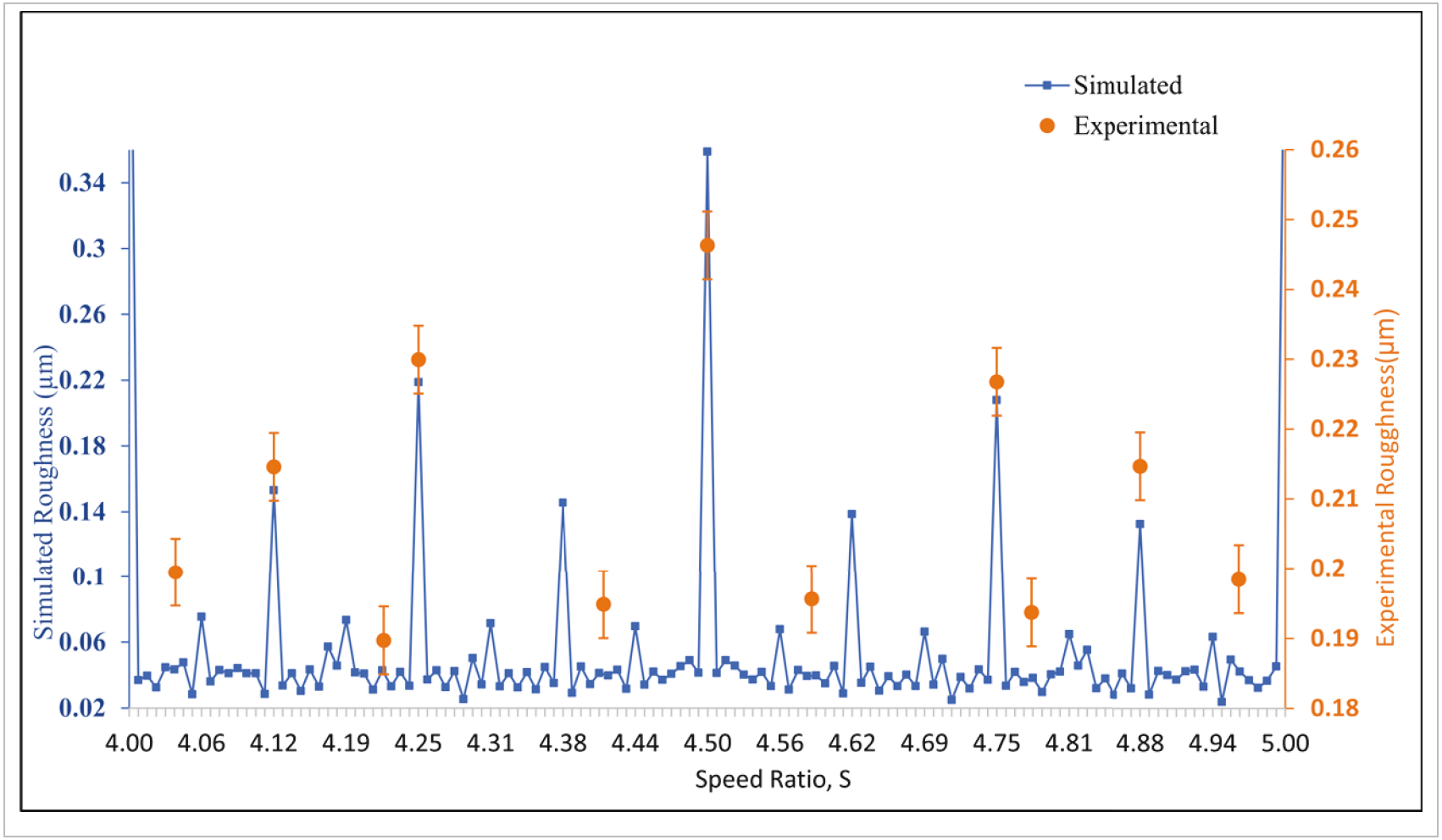

Figure 5.25: Comparison of trends between experimental and simulated surface roughness at different speed ratios using a non-grooved grinding wheel

5.3.2.2 Process Forces and Spindle Power results

The raw force and power data were filtered using a lowpass Butterworth filter with a cut-off frequency of 1 Hz.

Figure 5.26 compares the normal force cycles for the grooved and the non-grooved wheel grinding at S=4.5. As shown in the figure, the grooved wheel grinding force reaches steady state earlier than the non-grooved wheel grinding normal force. The steady state value of the normal force for grooved wheel grinding is lower than the steady state value of the normal force for non-grooved wheel grinding. These results shows that grooved wheel grinding required lower process forces than non-grooved wheel grinding. The spark-out of the grooved wheel grinding was completed in 7 seconds after the completion of the steady-state phase. In comparison, the non-grooved wheel grinding took 10 seconds to complete the spark-out as shown in Figure 5.26. This result shows that the non-grooved wheel performed cutting action for more time than the grooved wheel. Similar observations of lower spark-out time with grooved wheels was consistent for all other non-integer speed ratios used. The tangential forces and spindle power also were also observed to have lower steady-state magnitude for grooved wheel grinding when compared to non-grooved wheel grinding for all the speed ratios. Like normal force, the tangential force and spindle power curves completed the spark-out phase earlier for grooved wheel grinding as compared to non-grooved wheel grinding.

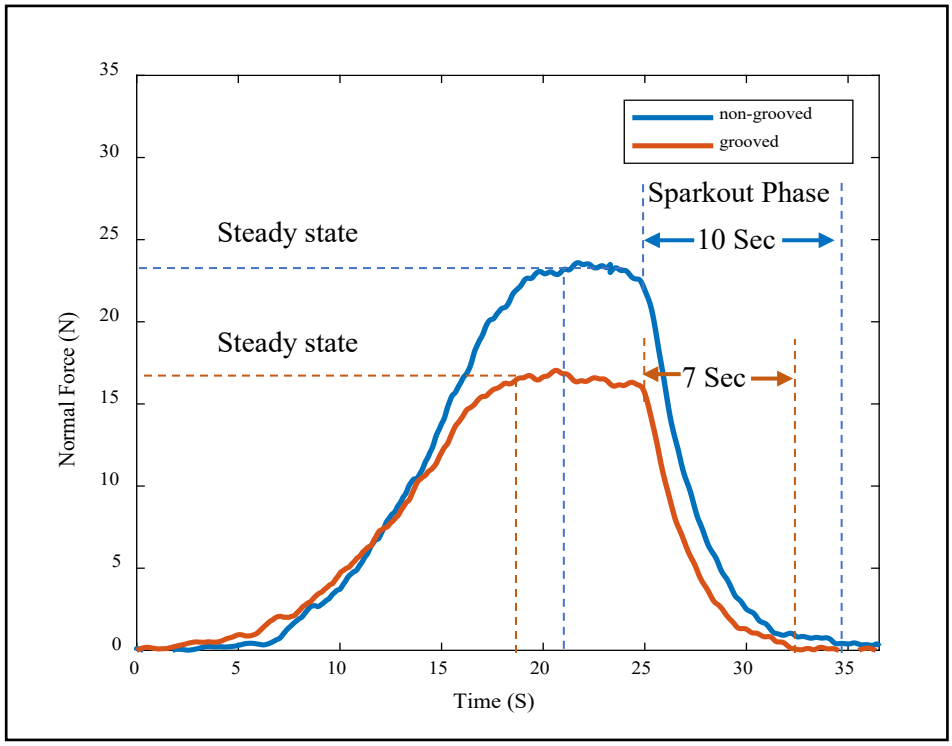

Figure 5.26: Comparison of normal force cycle for grooved and non-grooved wheel grinding at S=4.5

The steady state values of forces and spindle power were recorded for all the experiments. The transverse force was approximately zero for all the experiments and hence the transverse force has not been shown.

Figure 5.27 (a) shows the comparison of normal force between grooved wheel grinding and non-grooved wheel grinding. Grinding at S=4.5 required the least normal force than the other speed ratios for both grooved and non-grooved wheel grinding. S=4.75 required more normal force than S=4.5 but less than the other speed ratios. Other speed ratios that had a better surface finish than 4.5 and 4.75 required higher normal force. On average, the grooved wheel reduced the normal forces by 37.6% as compared to the non-grooved wheels.

Figure 5.27 (b) compares the tangential forces for different speed ratios when grinding with a grooved and non-grooved grinding wheel. Similar to the normal force results, the tangential force was found be least for S=4.5 followed by S=4.75. The trend of tangential forces was similar to the normal forces for grooved and non-grooved grinding. On average, grooved wheels reduced the tangential forces by 40.6% as compared to the non-grooved wheels.

The Spindle power required for grinding at different speed ratios using a grooved and non-grooved wheel is been shown in Figure 5.27 (c). Among all the grooved wheel grinding experiments, S=4.5 required the least power. This observation was true for the non-grooved grinding wheel experiments as well. S=4.25 and S=4.75 consumed the least power after S=4.5. The grooved wheel reduced the spindle power requirement by approximately 35% compared with the non-grooved wheels for the same speed ratios.

Experimental surface toughness of grooved and non-grooved wheel grinding plotted in Figure 5.24 and Figure 5.25 respectively has been plotted again in Figure 5.27 (d). It can be observed from Figure 5.27 (a), (b), (c) and (d) that the trend in normal force, tangential force and spindle power was mostly opposite to that of surface roughness for both the grooved and non-grooved grinding experiments.

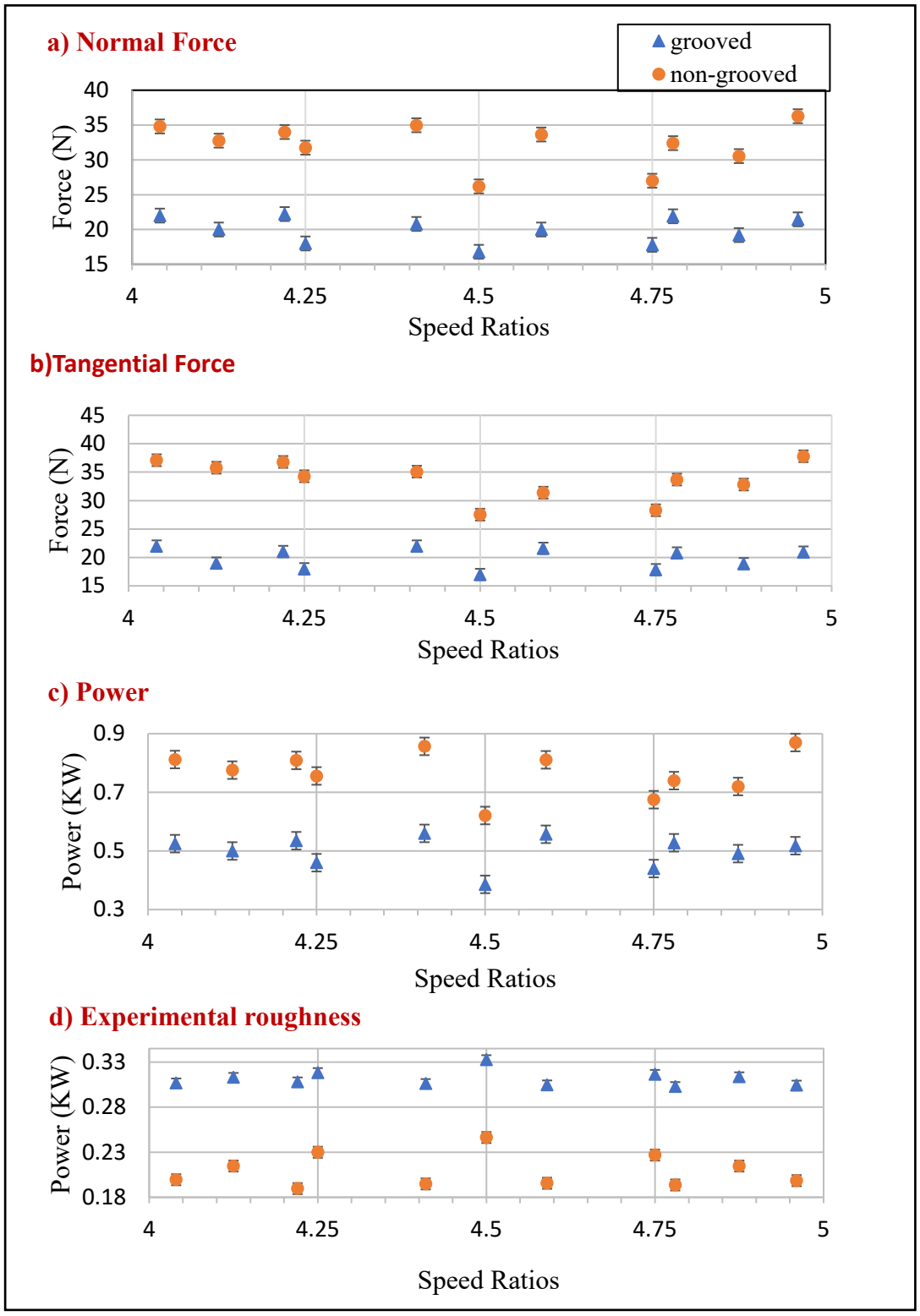

Figure 5.27: Comparison of a) normal force, b) tangential force, c) spindle power and experimental roughness for grooved and non-grooved wheel grinding

5.3.3 Conclusions for Non-integer Speed Ratio Experiments and Simulations

Cylindrical grinding experiments were performed to investigate the effect of speed ratios on the workpiece surface finish. Speed ratios of 4.25, 4.5 and 4.75 yielded higher surface roughness than other speed ratios. The trend of the surface roughness predicted by 2D cylindrical grinding simulator was found to be consistent with the experimental observations. The above factors were true for both grooved and non-grooved wheel cases.

The force and power analysis showed that grooved wheel grinding reached spark-out earlier than non-grooved wheel grinding. The spark-out phase for non-grooved wheel grinding was observed to run for 10 seconds after the steady phase as compared to 7 seconds in the grooved-wheel grinding case.

S=4.5, (which yielded the highest workpiece surface roughness) was found to have the least process forces and power for both grooved wheel and non-grooved wheel grinding. Speed ratios such as 4.01, 4.22, 4.41, 4.59 and 4.96 yielded superior surface finish were found to have higher process forces and power consumption compared to the speed ratios that gave the rougher surface finish.

5.4 Conclusions for Plunge Grinding Experiments

This chapter investigated the effect of integer speed ratios, dwell time and non-integer speed ratios on the workpiece surface roughness in cylindrical plunge grinding through kinematic simulations and experimental validation. The grooved wheel was found to affect textures on the workpiece at integer speed ratios. A dwell time of 10 seconds allowed enough time for the spark-out phase for the cylindrical grinding experiments with both grooved as well as non-grooved wheels. The grooved wheels were found to exhibit higher surface roughness than the non-grooved wheels but exhibited less process forces and spindle power consumption.

The next chapter analyzes cylindrical plunge grinding for different speed ratios to understand the trends observed in the surface roughness results of non-integer speed ratios.

Chapter 6

Analysis of Synchronization in Cylindrical Grinding

In the experimental and simulation results presented in Chapter 5, it was observed that integer speed ratios produced thread-like patterns on the workpiece surface and rough surface finishes. Furthermore, certain non-integer speed ratios also produced rough surface finishes.

Dewar *et al*. [4] postulated that these phenomena were due to the zero phase difference between the workpiece velocity and the wheel velocity. In this chapter, this concept will be fully developed by first considering a grinding wheel with one cutting edge and then considering a grinding wheel with multiple cutting edges. It should be pointed out that only the kinematics have been considered to establish the concepts and derive the formulas. Though the depth of cut is an obvious parameter in grinding, its specific magnitude is not relevant to this discussion.

Let us begin investigating the behaviour of cutting grains and their effect on the final workpiece surface with a simple case of a speed ratio S=4.5 with the number of grains on the grinding wheel N_g=5.

The wheel model for this simulation was designed using non-stochastically distributed grains having the same protrusion height. The plunge cylindrical grinding process was simulated for this case using the 2D cylindrical grinding simulator. Table 4.5 lists important parameters used as inputs to the simulator. Figure 6.1 shows the simulated workpiece profiles and corresponding roughness for S=4.5 after the completion of the 8th, the 9th and the 10th revolution of the grinding wheel.

As the simulation progresses from one revolution of the grinding wheel to the next, the workpiece profile changes and the roughness values decrease with each revolution until the 9th revolution. Comparing Figure 6.1 (a) and Figure 6.1 (b), it is evident that workpiece

material is still being removed on the 9th revolution and the overall surface roughness decreases from 14.02 μm to 8.17 μm. However, as can be seen in Figure 6.1 (b) and 6.1 (c), workpiece profiles and surface roughness values of the workpiece after the 9th revolution and the 10th revolution are identical. More simulations were conducted for further wheel revolutions, but the final workpiece profiles and their surface roughness remained the same as the 9th revolution workpiece profile and roughness value. These simulations show that the grains stopped cutting after the 9th wheel revolution. This result can be thought to have happened because, after the 9th revolution, the grains follow the same earlier paths that led to workpiece material removal.

In any form of grinding, each grain of a grinding wheel follows a fixed path into the workpiece although every grain might not remove workpiece material. Additionally, for cylindrical grinding, each grain's path depends on the speed ratio between the grinding wheel and the workpiece. Using kinematics and geometry, it is possible to determine the theoretical grain path if one were to neglect the effects of vibrations, speed fluctuations, misalignments, and dimensional errors. It has been observed in the previous example that, as the grain interacts with the workpiece, the path of each grain starts to repeat after a certain number of wheel revolutions. This repetition of the path ultimately makes all grains inactive since there is no material removal when retracing the same path throughout the workpiece.

The present author coined the term “synchronization” to describe the phenomenon of a grain’s trajectory falling exactly on its own or other grains’ previous trajectories thereby making the grain inactive and resulting in no further removal of workpiece material. In constant speed ratio cases where the velocity of the grinding wheel and workpiece do not change throughout the entire grinding process, grains do not create new trajectories once synchronization has been achieved.

a) workpiece profile after 8 Wheel revolutions

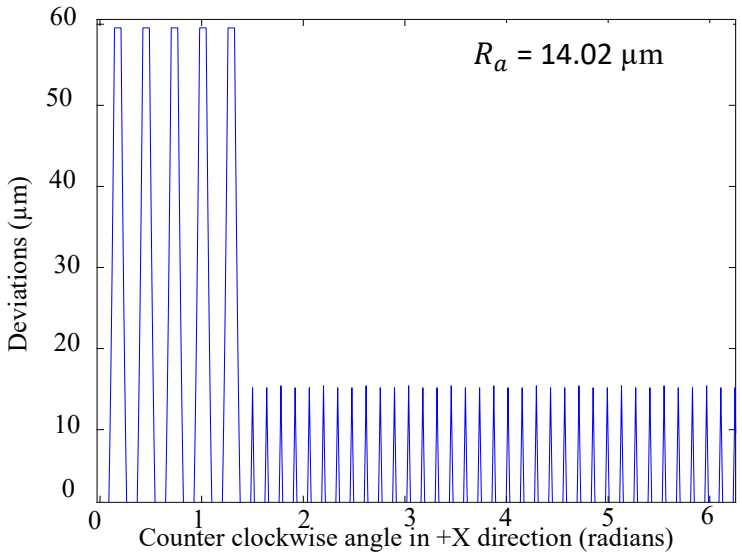

b) workpiece profile after 9 Wheel revolutions

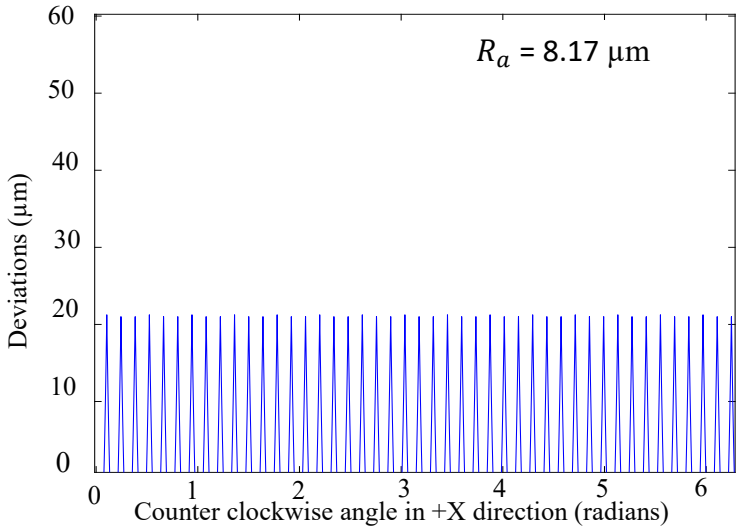

c) workpiece profile after 10 Wheel revolutions

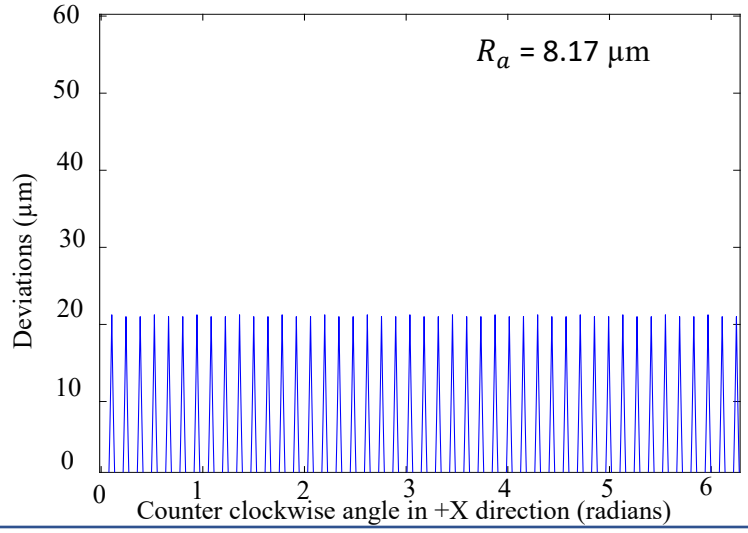

Figure 6.1: Final workpiece surface Deviations

6.1 Synchronization in a Single-grain Wheel Model

To help explain the synchronization phenomenon, we start with the kinematics of a single cutting grain. A single-grain wheel model can be thought of as a hypothetical wheel with one grain on its periphery. Starting with one grain helps to more easily understand the geometry of how a grain interacts with the workpiece.

Figure 6.2 shows the grinding wheel and workpiece contact at the grinding wheel's Bottom Dead Center (BDC) and the workpiece's Top Dead Center (TDC). In this figure, the coordinate system used for the mathematical derivations is defined. The angles for the grinding wheel are defined with respect to its BDC and the angles for the workpiece are defined with reference to its TDC. The counterclockwise direction is considered to have a positive angle.

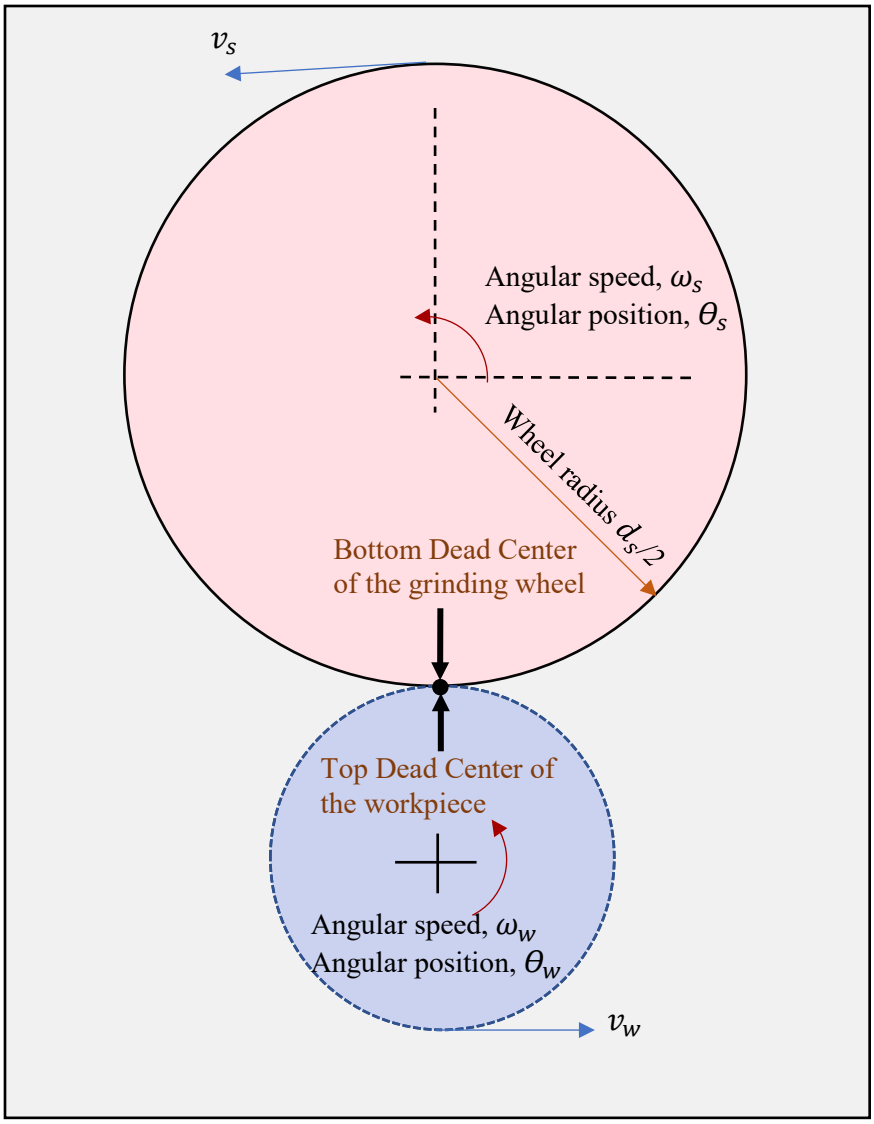

Figure 6.2: The co-ordinate system for cylindrical grinding

6.1.1 Synchronization with Integer Speed Ratios

Unless otherwise stated, units for angular position, angular speed and time are radians, radians/sec and seconds, respectively.

As discussed earlier, the speed ratio S is defined as the ratio of the grinding wheel angular speed ω_s and the workpiece angular speed ω_w:

$$S = \frac{\omega_s}{\omega_w} \tag{6.1}$$

If t is the time from the start of the grinding process to the current time, then the angular position of the grinding wheel θ_s at any given time is calculated using:

$$\theta_s = \omega_s \times t \text{ radians} \tag{6.2}$$

Similarly, the angular position of the workpiece θ_w at any given time is calculated using:

$$\theta_w = \omega_w \times t \text{ radians} \tag{6.3}$$

From Equation 6.2 and Equation 6.3,

$$t = \frac{\theta_s}{\omega_s} = \frac{\theta_w}{\omega_w} \text{ seconds} \tag{6.4}$$

From Equation 6.4 and Equation 6.1,

$$\frac{\theta_s}{\theta_w} = \frac{\omega_s}{\omega_w} = S \tag{6.5}$$

Rearranging Equation 6.5 gives,

$$\theta_s = S \times \theta_w \text{ radians} \tag{6.6}$$

From Equation 6.6, if S is an integer, then the grinding wheel will rotate through S complete revolutions for one revolution of the workpiece at which point synchronization will occur. Therefore, if we let N_s^{syn} be the minimum number of grinding wheel revolutions required for the system to attain synchronization, then

$$N_s^{syn} = S \tag{6.7}$$

As a result, the simplest case of grain synchronization in cylindrical grinding occurs when the speed ratio S is an integer value where a grain on the grinding wheel comes into phase with one of its previous workpiece cuts after N_s^{syn} revolutions. The term self-synchronization is used to describe when the grain synchronizes with its own previous cutting path.

Examples of such type of self-synchronization have been illustrated in Figure 6.3. For Case 1 where S=1, the rotational speeds of the grinding wheel and the workpiece are the same. This condition means that the grain on the grinding wheel cuts the workpiece at a fixed location every revolution. As can be observed in parts (a), (b) and (c) of Case 1 in Figure 6.3, the grain on the grinding wheel meets the same point on the workpiece every revolution and hence the path of cut of the first revolution is re-traced in the second and third revolution. In this case, synchronization has occurred after 1 revolution ($N_s^{syn} = 1$) which is equal to S from Equation 6.7 since the grain effectively becomes inactive after this point.

Case 2 of Figure 6.3 illustrates synchronization for S=3. Since S is again an integer like in Case 1, $N_s^{syn} = S = 3$. Since from Equation 6.7, N_s^{syn}=3, it takes three revolutions of the grinding wheel before the grain stops cutting due to self-synchronization. As shown in parts (a), (b) and (c) of Case 2 in Figure 6.3, three new cuts occur until the third revolution of the grinding wheel. There is no change in surface geometry of the workpiece in the fourth revolution as shown in part (d). The workpiece remains unaffected thereafter for any number of further wheel revolutions. In the fourth wheel revolution, the grain path follows the first cut and, similarly, in the fifth wheel revolution the grain path would follow the second cut, the sixth on the third, the seventh on the first again and so on. This principle holds true for any integer speed ratio which implies that the number of cuts on the workpiece is equal to the integer speed ratio. It is important to note that for all integer speed ratio cases, the workpiece rotates just once after which all of the cut patterns on the workpiece synchronize with the grain.

Figure 6.4 shows workpiece profiles generated by single grain simulations for cylindrical grinding with S=3. The cylindrical grinding process was simulated for 1000 revolutions of the grinding wheel. As evident in the figure, a fresh cut occurs on the workpiece for the first three revolutions of the grinding wheel and then the workpiece profile remains unchanged after the 3rd wheel revolution. The visual representation of the synchronization in Figure 6.3 (Case 2) and the simulation results in Figure 6.4 show that, when grinding with integer speed ratios, synchronization is achieved after S=3 wheel revolutions. Both of these figures confirm the validity of Equation 6.7.

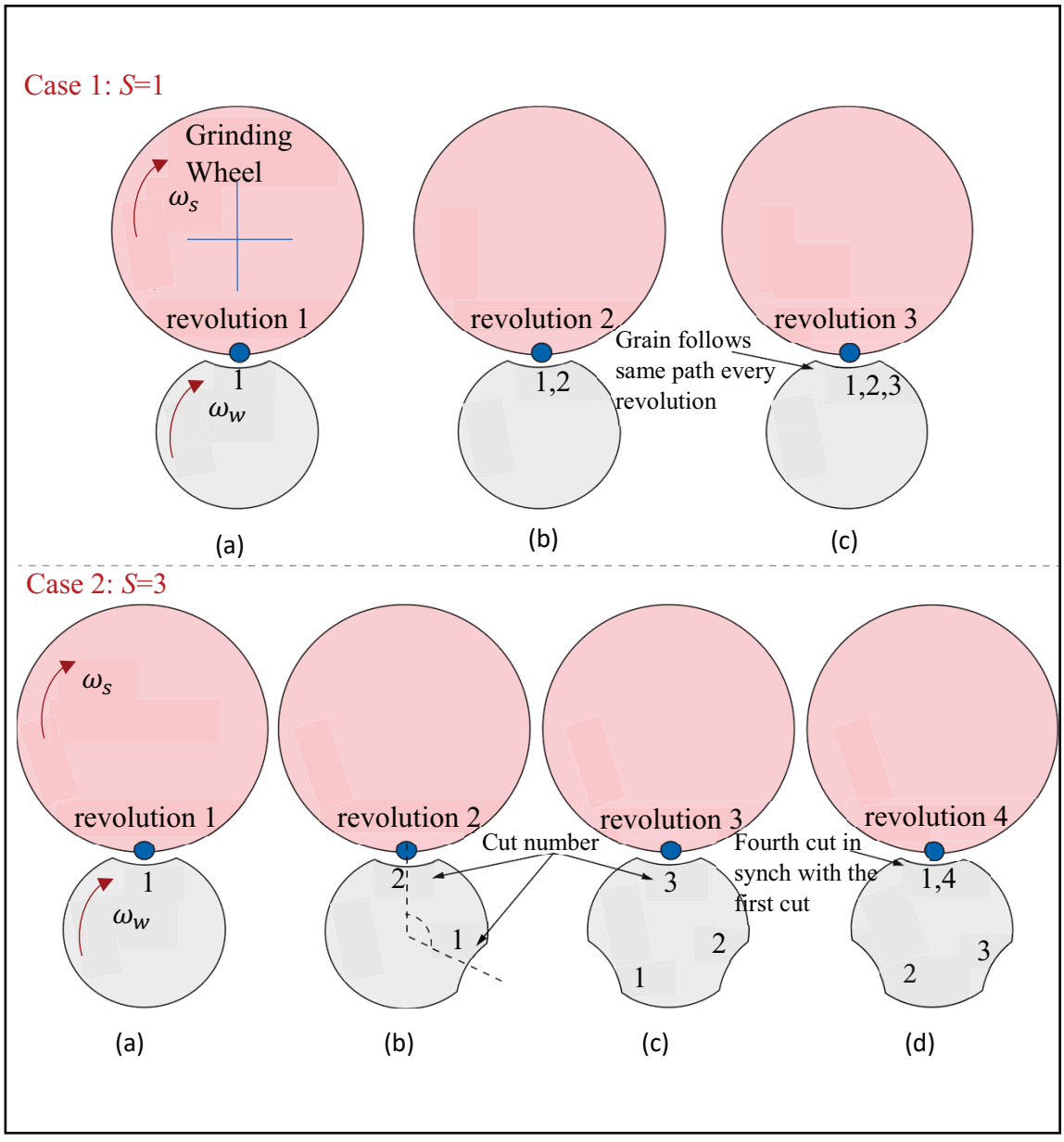

Figure 6.3: Single grain Self-Synchronization in integer speed ratios

For *S*=3

A) workpiece profile after 1 revolution of the grinding wheel

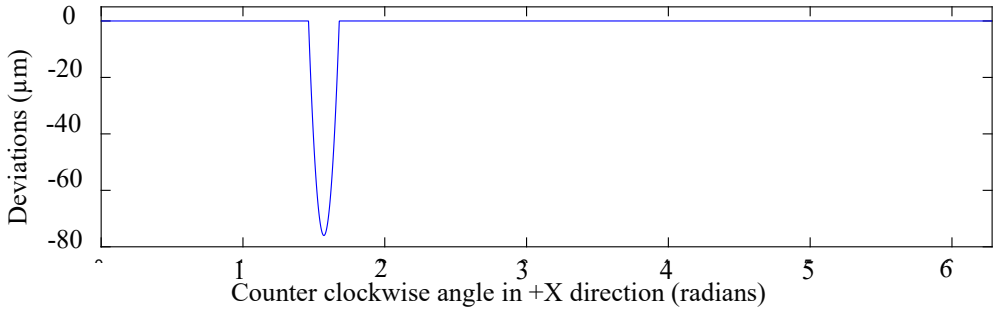

B) workpiece profile after 2 revolutions of the grinding wheel

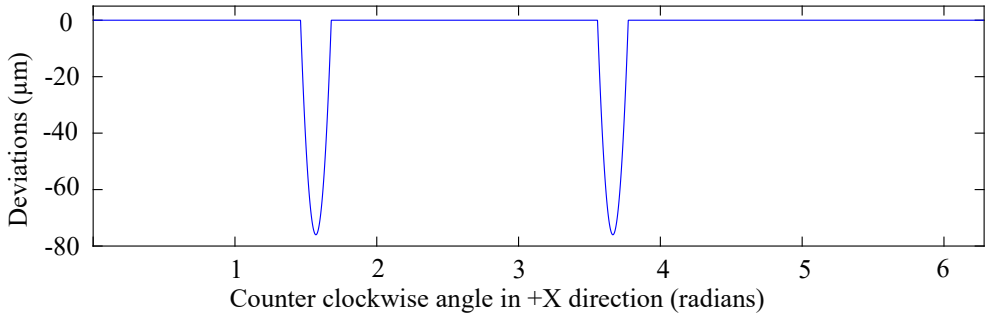

C) workpiece profile after 3 revolutions of the grinding wheel

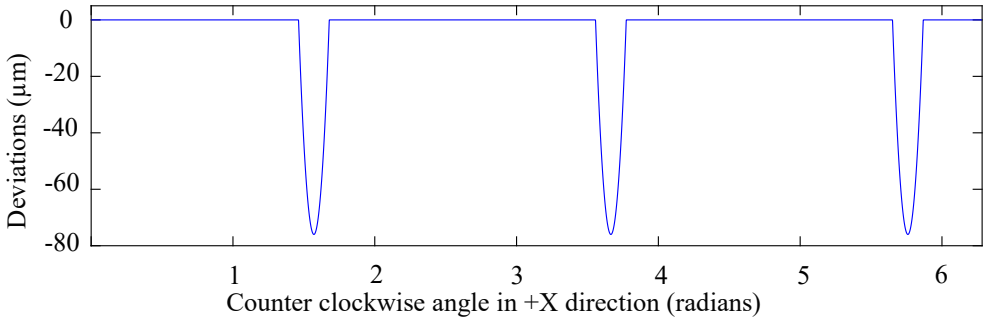

D) workpiece profile after 1000 revolutions of the grinding wheel

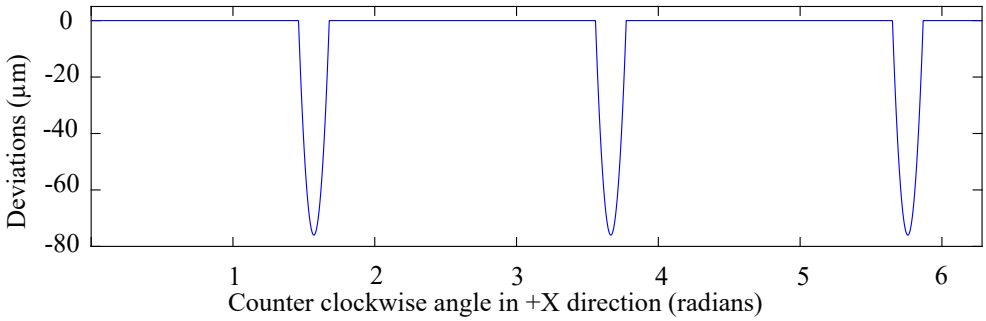

Figure 6.4:Simulated workpiece profiles for plunge cylindrical grinding at *S*=3 with single grain model

6.1.2 The Phase Difference in Non-integer Speed Ratios

The number of complete revolutions of the grinding wheel N for one revolution of the workpiece can be determined by rounding down the value of speed ratio S:

$$N = round\ (S) \tag{6.8}$$

Therefore, the number of incomplete revolutions of the grinding wheel f for one revolution of the workpiece is:

$$f = S - N \tag{6.9}$$

The phase angle ϕ_s of the grinding wheel is the angle in radians which the wheel rotates past BDC for one revolution of the workpiece. Figure 6.5 illustrates the concept of the phase difference for non-integer speed ratios. Grain *G* on the grinding wheel is assumed to cut into the workpiece at the starting condition (Figure 6.5 (a)) to create cut #1. After one complete revolution of the workpiece, when cut #1 reaches TDC once again (Figure 6.5 (b)), grain *G* on the wheel had travelled beyond BDC by the phase angle ϕ_s. An alternate way to visualize the situation is to think in terms of one complete grinding wheel revolution (Figure 6.5 (c)) rather than one complete workpiece revolution. Since the value of S is 1.2, the grinding wheel speed is higher than the workpiece speed. Therefore, by the time grain *G* comes back to BDC to create cut #2 (Figure 6.5(c)), cut #1 on the workpiece has not yet returned to TDC. Since the workpiece speed is lower than the grinding wheel speed, cut #1 lags in phase thereby leading to the exposure of fresh workpiece surface. This newly exposed surface meets grain *G* and cut #2 is created on the workpiece at an angle equal to the workpiece phase difference ϕ_w from cut #1. Case (b) and Case (c) in Figure 6.5 summarize the two different ways to look at the difference in phases of grain *G* and cut #1.

Using the definition of f in Equation 6.9, the phase angle of the grinding wheel after one revolution of the workpiece can be calculated as:

$$\phi_s = 2\pi f \text{ radians} \tag{6.10}$$

Substituting Equation 6.10 into Equation 6.6 allows us to calculate the angular rotation of the workpiece θ_w for a given angular rotation of the wheel $\theta_s = \phi_s = 2\pi f$ as follows:

$$2\pi f = S\phi_w \text{ radians} \tag{6.11}$$

Rearranging Equation 6.11 yields a relationship for the workpiece phase difference ϕ_w:

$$\phi_w = \frac{2\pi f}{S} \tag{6.12}$$

Referring to Figure 6.5 (c), it can be seen that the phase difference ϕ_w is the angle between two consecutive cuts affected by the same wheel grain. It can be further noted that Equation 6.9 and 6.12 confirms our understanding of phase difference since for integer values of S, $f = 0$ giving $\phi_s = \phi_w = 0$ radians.

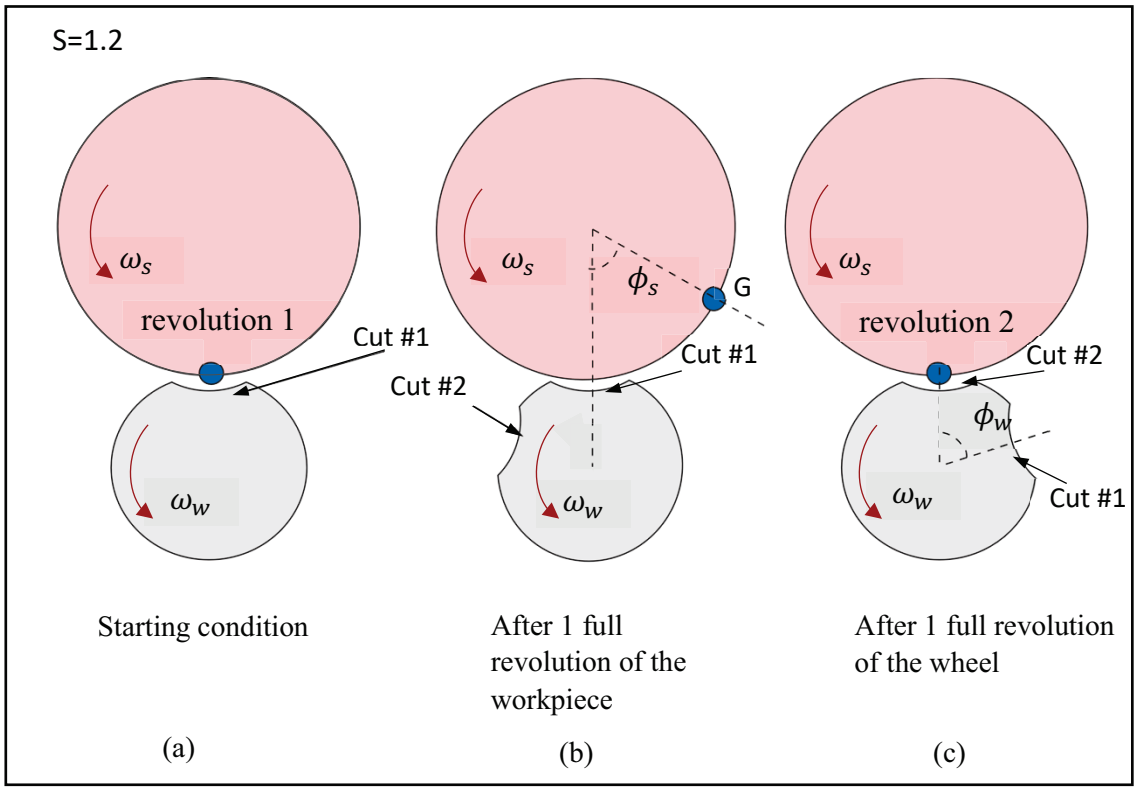

Figure 6.5: Illustration of phase difference in non-integer speed ratios

6.1.3 Synchronization with Non-integer Speed Ratios

Section 6.1.1 showed that integer speed ratios result in synchronization of the grinding wheel and the workpiece. This section will demonstrate that rational speed ratios also result in synchronization. Note that a rational number is a number that can be determined by dividing two integers [61]. In this section, the number of revolutions required to achieve synchronization will also be determined.

Let the minimum number of grinding wheel revolutions required for synchronization be N_s^{syn} and the minimum number of workpiece revolutions required for synchronization be N_w^{syn}.

Since synchronization of the grinding wheel and the workpiece occurs at the same instant in time, from Equation 6.5 we can see that:

$$S = \frac{N_s^{syn}}{N_w^{syn}} \tag{6.13}$$

where S is the speed ratio.

Since N_s^{syn} and N_w^{syn} are integers, S in Equation 6.13 case is a rational number. Therefore, the number of revolutions required for synchronization can be determined by converting S to a fraction and examining the numerator and denominator to determine N_s^{syn} and N_w^{syn}.

From Equation 6.9,

$$S = N + f \tag{6.14}$$

Since f <1, it may have n digits after the decimal point. For example, if f=1.25 then N=1 from Equation 6.8, f=0.25 from Equation 6.9 and n=2.

Based on the theory of rational numbers, the following equation can be used to determine the number of workpiece revolutions required for synchronization:

$$N_w^{syn} = \frac{10^n}{\text{GCD}\,(10^n,\, S \times 10^n)} \quad \text{revolutions} \tag{6.15}$$

where GCD refers to the greatest common divisor.

Using Equation 6.13 and multiplying Equation 6.15 by speed ratio S gives the minimum number of grinding wheel revolutions N_s^{Syn} after which the system attains synchronization:

$$N_s^{syn} = \frac{S \times 10^n}{\text{GCD}\,(10^n,\, S \times 10^n)} \quad \text{revolutions} \tag{6.16}$$

To validate Equation 6.16, we compare its prediction for N_s^{syn} using S=1.2 with a simulation result illustrated in Figure 6.6. Equation 6.16 yields N_s^{syn}= 6. As shown in Figure 6.6 (a) to 6.6 (e), a new cut is imparted to the workpiece by the same single grain *G* for all five revolutions of the wheel. From Equation 6.12, the phase difference for the speed ratio in consideration is 60 degrees. This angle means that two consecutive cuts imparted on the workpiece by the same wheel grain will be placed at an angle of 60 degrees from each other and grain *G* traces the same path of cut #1 in the sixth revolution of the grinding wheel (Figure 6.6 (f)). Since cut #1 is already established in the wheel grain's first revolution, the sixth revolution does not affect further cutting and the grain effectively becomes inactive. This pattern continues such that the grain trajectory will retrace cut #2 on the seventh wheel revolution, cut #3 on the eighth, cut #4 on the ninth, cut #5 on the tenth and cut #1 will be traced again on the eleventh wheel revolution. All the retracing revolutions after fifth revolutions do not result in the workpiece being cut since the grain is in synchronization with all its previous cuts.

Minimum dwell time T_{max} required for the grinding wheel to complete N_s^{syn} revolutions can be determined by using the following equation:

$$T_{max} = \frac{60 \times N_s^{syn}}{\omega_s} \quad \text{seconds} \tag{6.17}$$

where ω_s is the angular speed of the grinding wheel in revolutions per minute.

The knowledge of the magnitude of T_{max} for a given speed ratio is an important factor since it can be used to determine the required minimum dwell time during grinding experiments.

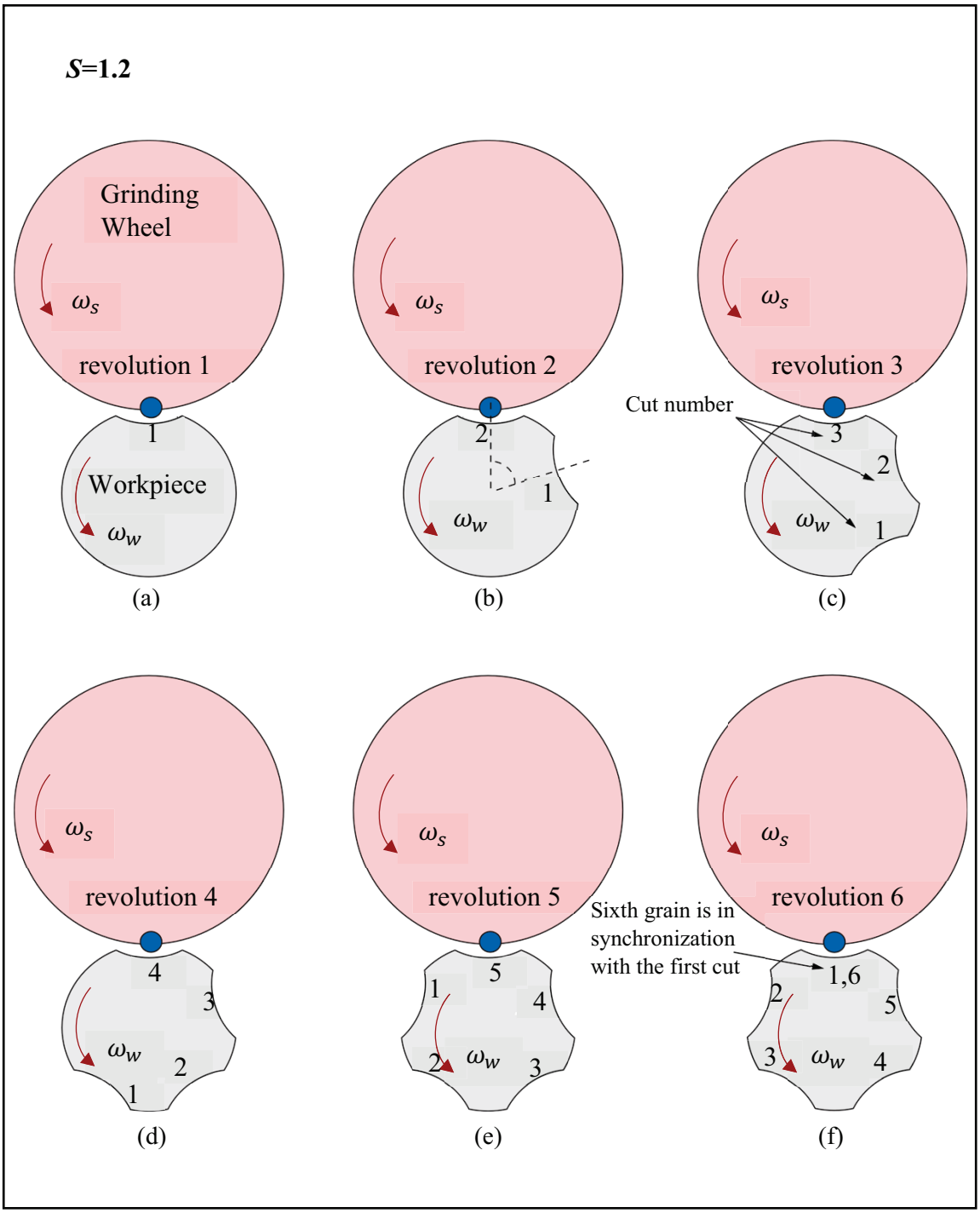

Figure 6.6: Single grain self-synchronization in non-integer speed ratios

6.2 Synchronization in Multiple-grain Non-stochastic Wheel Models

This section aims to extend the understanding of synchronization for a single-grain wheel model to a non-stochastic multiple-grain model. As illustrated in Figure 6.7, a so-called non-stochastic wheel model has evenly-spaced grains at equal protrusion heights. The wheel model in this example has four grains: *a*, *b*, *c*, and *d* — all at the same protrusion heights. The angular distance between two adjacent grains is called the grain spacing θ_g.

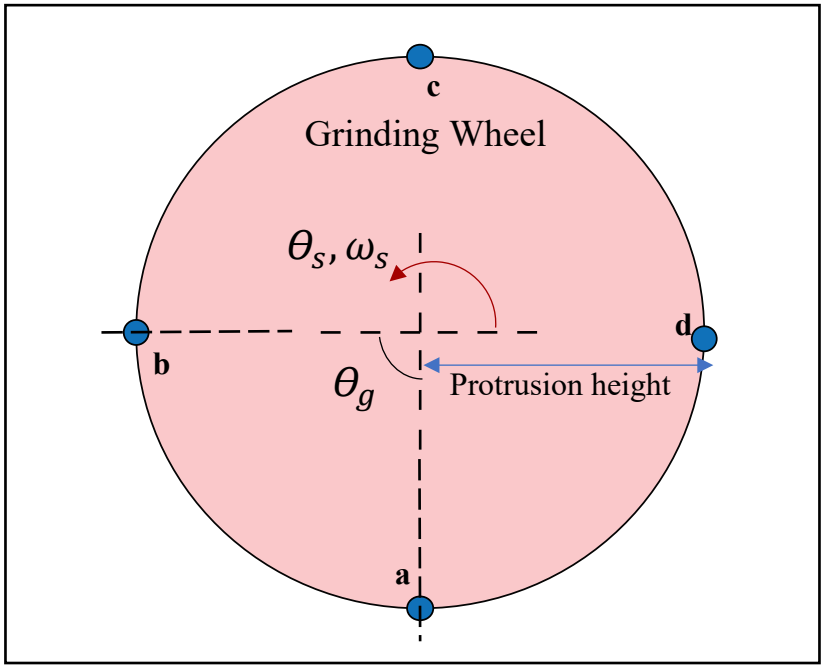

Figure 6.7: A non-stochastic wheel model (N_g=4)

For a non-stochastic wheel with N_g grains, the grain spacing θ_g is calculated using:

$$\theta_g = \frac{2\pi}{N_g} \text{ radians} \tag{6.18}$$

First, we will look at the effect of non-stochastic wheel models on the synchronization of integer speed ratios and then the non-integer speed ratio cases will be studied.

6.2.1 Synchronization of Non-stochastic Wheel Models with Integer Speed Ratios

To study the synchronization of non-stochastic wheel models with integer speed ratios, Figure 6.8 maps the grinding wheel grains onto the workpiece surface for the first wheel revolution for S=4 and N_g=4. Grinding is assumed to start when grain a touches the workpiece at location a_1. Similarly, the projection of grains b, c and d on the wheel are at b_1, c_1 and d_1 on the workpiece.

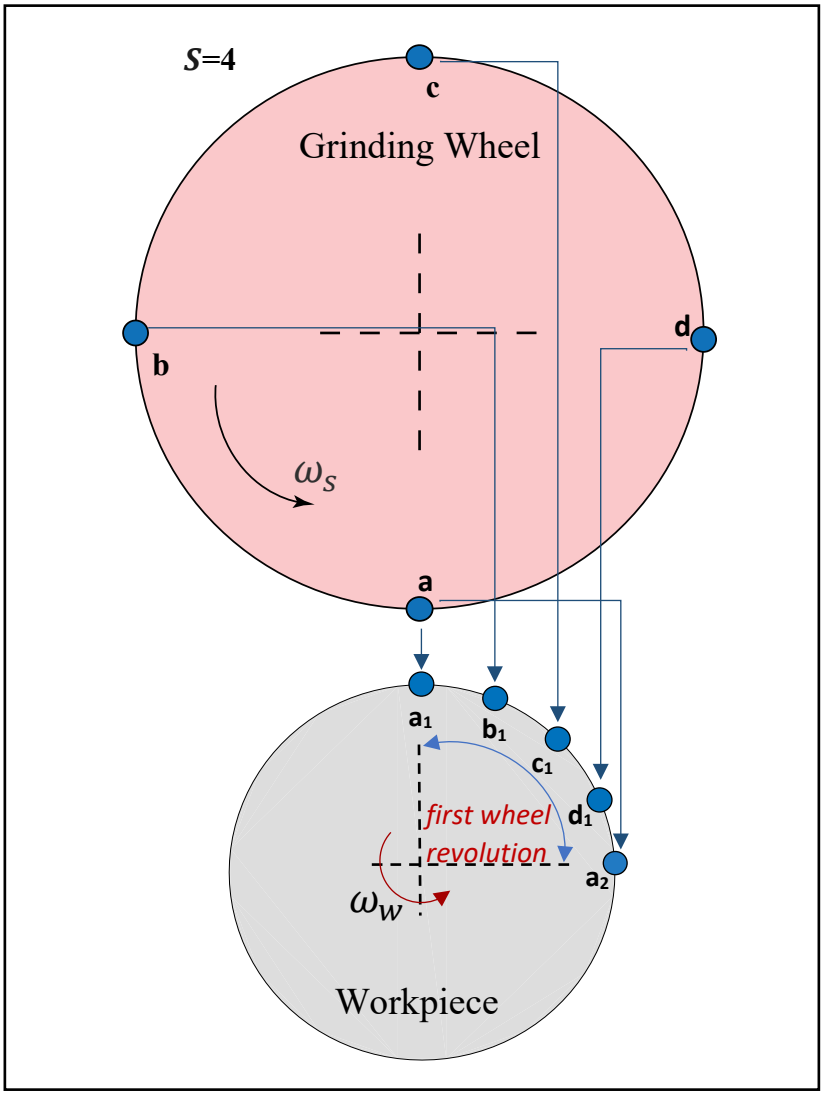

Figure 6.8: Projection of wheel grains on cylindrical workpiece for first wheel revolution. (N_g=4, S=4)

Note that the subscripts in the grain location on workpiece represent the number of grinding wheel revolution for which those projections correspond. For example, the first wheel revolution is completed when grain *a* touches the workpiece at a_2.

Figure 6.9 is the continuation of the previous example of Figure 6.8. The second wheel revolution (Figure 6.9 (a)) starts at a_2 and ends at a_3. Here, θ_w is the angle of workpiece rotation for one revolution of the wheel.

The angle of workpiece rotation θ_w for one revolution of the wheel can be determined if the speed ratio *S* is known using Equation 6.6 as follows:

$$\theta_w = \frac{2\pi}{S} \text{ radians} \tag{6.19}$$

Therefore, the angular distance *D* between two consecutive cuts on the workpiece by two adjacent wheel grains in the non-stochastic wheel model can be calculated by:

$$D = \frac{2\pi}{N_g \times S} \text{ radians} \tag{6.20}$$

For example, when S=4 and N_g=4, Equation 6.20 predicts that D=0.393 radians. Figure 6.9 (b) represents the state of workpiece after the third wheel revolution while the fourth wheel revolution (Figure 6.9 (c)) starts at a_4 and ends at a_5. It should be noted that location a_5 is exactly the same as a_1 from the first revolution. This result means that the workpiece and wheel are in synchronization at the end of the fourth wheel revolution. All the wheel grains would fall exactly at the same previous locations in sequence for further revolutions.

Figure 6.10 is a simulation-based result of the final workpiece surface deviation of the cylindrical grinding process at a speed ratio of 4. The angular distance between two cuts *D* in Figure 6.10 was measured and compared with the analytical solution shown by Equation 6.20 and was found to agree. The simulation was then used to successfully validate Equation 6.20 for different sets of integer speed ratios.

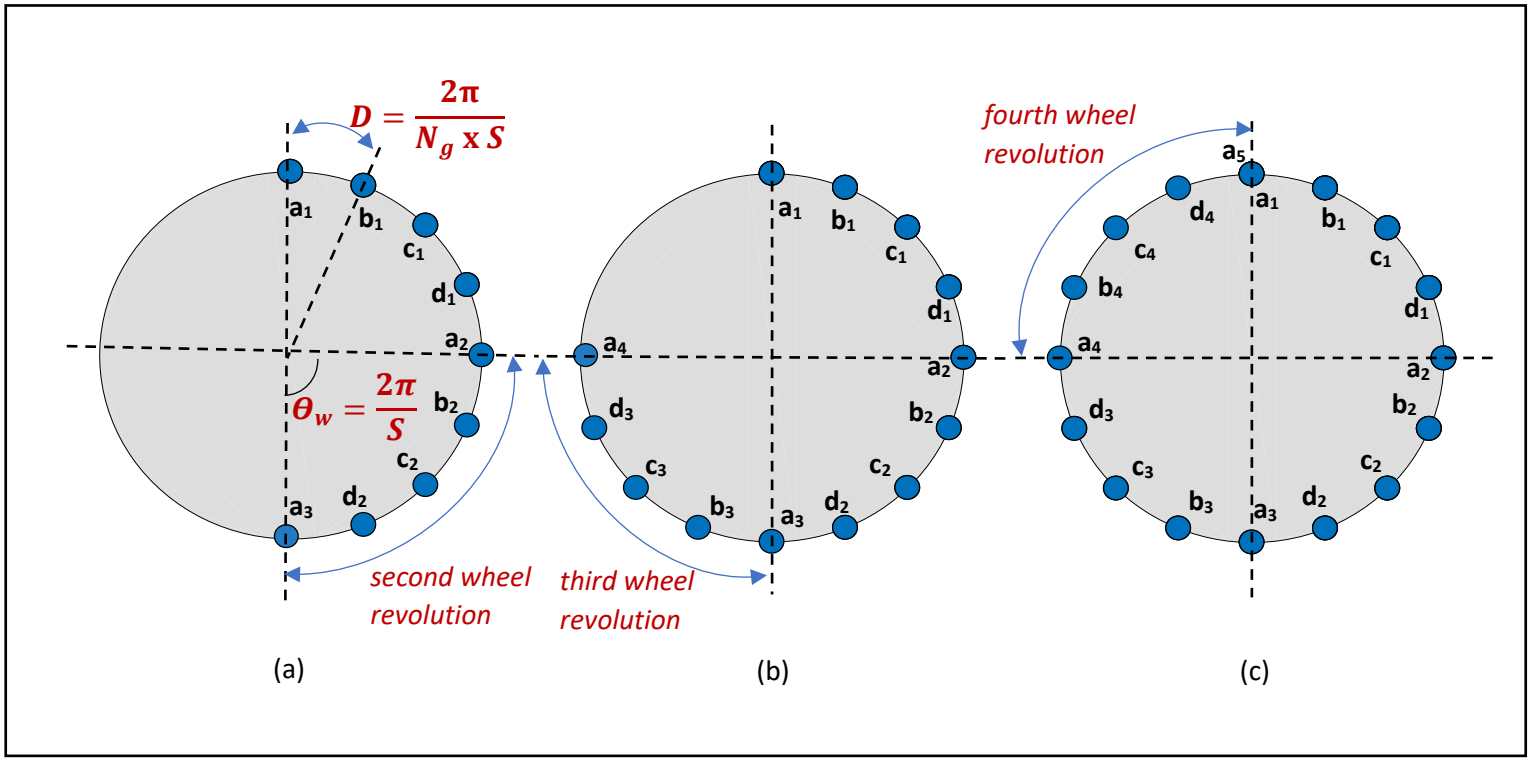

Figure 6.9: Projection of wheel grains on cylindrical workpiece for second, third- and fourth-wheel revolution. (Ng=4, S=4)

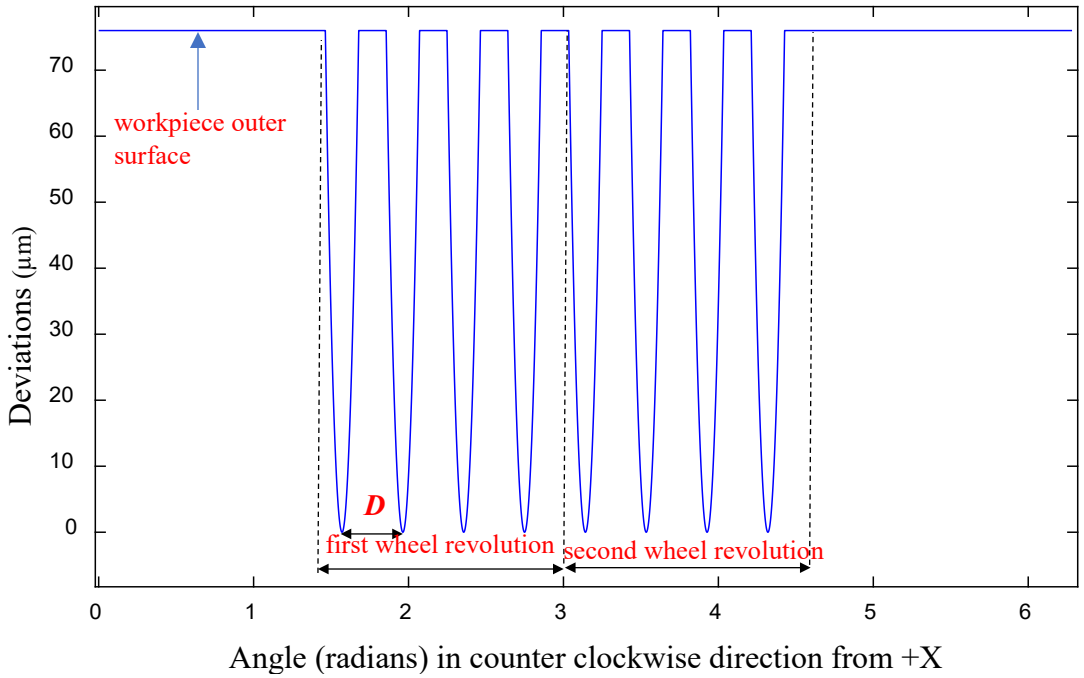

Figure 6.10: Final workpiece surface deviations for S=4 (first two wheel revolutions)

For an N_g-grain non-stochastic wheel model grinding at integer speed ratios, each grain can be thought to follow the same principle of synchronization as a single grain wheel model. Therefore, the grain touches the same point on the workpiece when the grinding process operates at integer speed ratios. Similar to the single-grain wheel model, each grain on the non-stochastic wheel is in phase with its respective cut after N_s^{syn} revolutions of the wheel which has a value identical to the speed ratio as determined by Equation 6.7.

Therefore, for cylindrical grinding with integer speed ratios S and non-stochastic wheel models with any number of grains, the system achieves synchronization after $N_s^{syn} = S$ revolutions of the grinding wheel similar to the single grain model case.

The next section studies the synchronization phenomenon in cylindrical grinding with non-stochastic wheel models when the speed ratios are non-integers.

6.2.2 Synchronization of Non-stochastic Wheel Models with Non-Integer Speed Ratios

6.2.2.1 Earliest Synchronization Cases

An example of synchronization with a non-stochastic wheel model and non-integer speed ratio is shown in Figure 6.11. The speed ratio S is 4.75 and the number of equally-protruding evenly-spaced grains N_g is 4.

Figure 6.11 (a) shows a projection of the wheel grains (*a*, *b*, *c*, and *d*) on the cylindrical workpiece during the first wheel revolution of the grinding wheel. This figure is similar to Figure 6.9 except that the angle the workpiece has revolved after the grinding wheel has completed one revolution is from Equation 6.19, 2π/4.75 radians. In addition, as shown in Figure 6.11 (b), the angular spacing around the workpiece of the grain contact points D is calculated by Equation 6.20 which for this case is 2π/(4×4.75). Figure 6.11 (b) to Figure 6.11 (d) shows the progression of the grinding process until the fourth wheel revolution. It is important to note in Figure 6.11 (e) that the wheel's fifth revolution starts at *a5* and would normally end at *a6* but the location on the workpiece at *a6* was already cut by *b1* in the wheel's first revolution. Similarly, *d5* overlaps *a1*. This synchronization means that the wheel only cuts the workpiece until *c5*. When the wheel reached *d5*, the grains effectively become inactive as they started to retrace the already-cut paths thereby ceasing to remove any material. If the grinding wheel does another 6th revolution as shown in Figure 6.11 (f), no further cutting occurs.

According to Equation 6.16, a single grain wheel grinding at S=4.75 would, starting with the grain at bottom-dead center (BDC), require 19 wheel revolutions for synchronization to occur; however, the 4-grain non-stochastic wheel in Figure 6.11 took only 4.75 grinding wheel revolutions to synchronize. This early synchronization occurs because, after the workpiece completes one revolution, a grain on the grinding wheel is in the BDC position of the grinding wheel. The following is one way of mathematically expressing this observation.

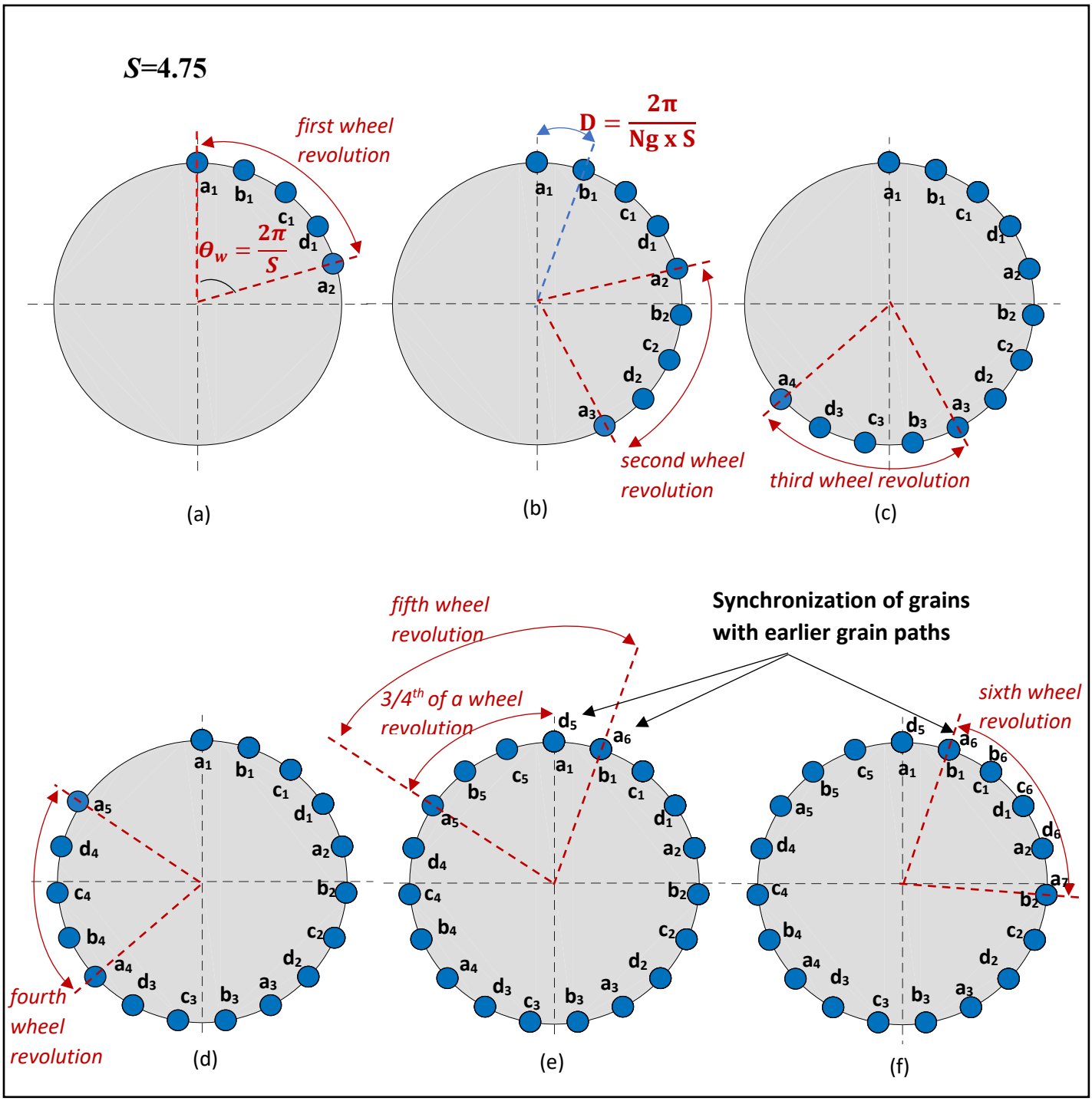

Figure 6.11: Projection of wheel grains on cylindrical workpiece for N_g=4 and S=4.75

For a rotating non-stochastic wheel model with N_g grains, there will be a grain at BDC N_g times per revolution of the grinding wheel. After S revolutions of the grinding wheel, there will have been $SN_g = i$ grains at BDC such that i is a positive integer. This relationship can be rewritten as:

$$(S - N)N_g = i - NN_g = i_{new} \tag{6.21}$$

where i_{new} is another positive integer value and N corresponds to the rounded-down integer value of the speed ratio S as explained in Equation 6.8.

Substituting Equation 6.9 in Equation 6.21 gives:

$$fN_g = i_{new} \tag{6.22}$$

When the product fN_g equals an integer value, the synchronization phenomenon illustrated in Figure 6.11 occurs (where there is a grain on the grinding wheel at BDC after the workpiece has completed 1 revolution). In this case, the number of grinding wheel revolutions for synchronization is:

$$N_s^{syn} = S \tag{6.23}$$

For the case shown in Figure 6.11, S=4.75, N_g=4, f=0.75, fN_g=3 (which is an integer value); therefore, $N_s^{syn} = 4.75$.

An example of synchronization for S=4.75 with the 4-grain non-stochastic wheel model is illustrated using simulation results in Figure 6.12. Simulated workpiece profiles after the wheel's first, third, fourth and fifth revolution are shown. As grinding progresses, it is clear from the workpiece profiles that a fresh area of the workpiece is exposed for cutting until the end of 4.75 wheel revolutions. This point corresponds to exactly one revolution of the workpiece. As seen in Figure 6.12 (c), after 4 wheel revolutions, the length of the uncut workpiece profile is equivalent to 3/4 of one grinding wheel revolution on the workpiece. This uncut area of the workpiece is cut in the next 3/4 wheel revolution (Figure 6.12 (d)). The grains retrace the previously-cut profile for the remaining ¼ revolution of the grinding wheel. This simulation shows and confirms that the system reached synchronization after 4.75 revolutions of the grinding wheel as suggested by Equation 6.23.

When using a non-stochastic wheel model with non-integer speed ratios, synchronization can occur much earlier than what is predicted by Equation 6.16 which corresponds to grinding with a single-grain wheel model with non-integer speed ratios. This difference occurs because, in a single-grain model, the grain can only synchronize with itself. Since the spacing and protrusion height of grains on multiple-grain non-stochastic wheel models are equal throughout the wheel circumference, synchronization happens when any grain trajectory comes into phase with another grain trajectory.

6.2.2.2 Sub-divisions of Earliest Synchronization Cases

In the previous section, it was determined that synchronization will occur if after one workpiece revolution there is a grain on the wheel at BDC to repeat the pattern of cuts. However, for some speed ratios, synchronization may only occur after two or more rotations of the workpiece. In this case, synchronization will occur when

$$nfN_g = i \tag{6.24}$$

where n is the number of workpiece revolutions required to ensure the product nfN_g is an integer value i.

Thus, the number of grinding wheel revolutions for synchronization will be:

$$N_s^{syn} = nS \tag{6.25}$$

It should be noted that the value of n in the previous section was effectively 1 and hence the workpiece revolved just once before synchronizing with the wheel grains. In some cases, the number of workpiece rotations is more than 1 and hence for the process to attain synchronization,

$$n > 1 \tag{6.26}$$

Take, for example, the case shown in Figure 6.13 where S=4.125 and N_g=4. Equation 6.24 states that the product $n(0.125)(4)$ must be an integer value. The smallest value of n that satisfies this requirement is n=2. Therefore, synchronization will occur after ($n \times S$) = 2 × 4.125 = 8.25 revolutions of the grinding wheel. This case is illustrated in Figure 6.13.

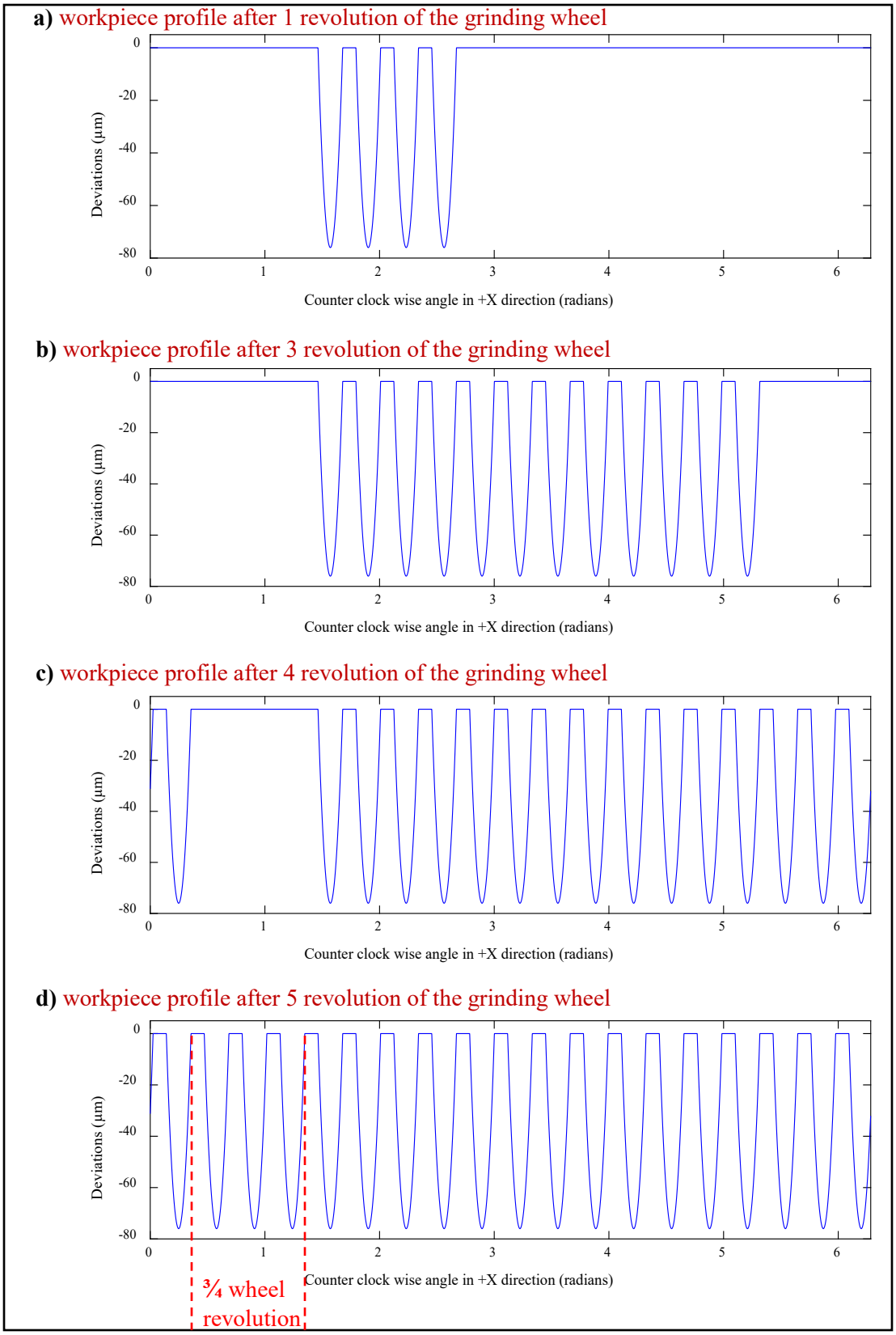

Figure 6.12: Simulated workpiece profiles for plunge cylindrical grinding at S=3 with single grain model

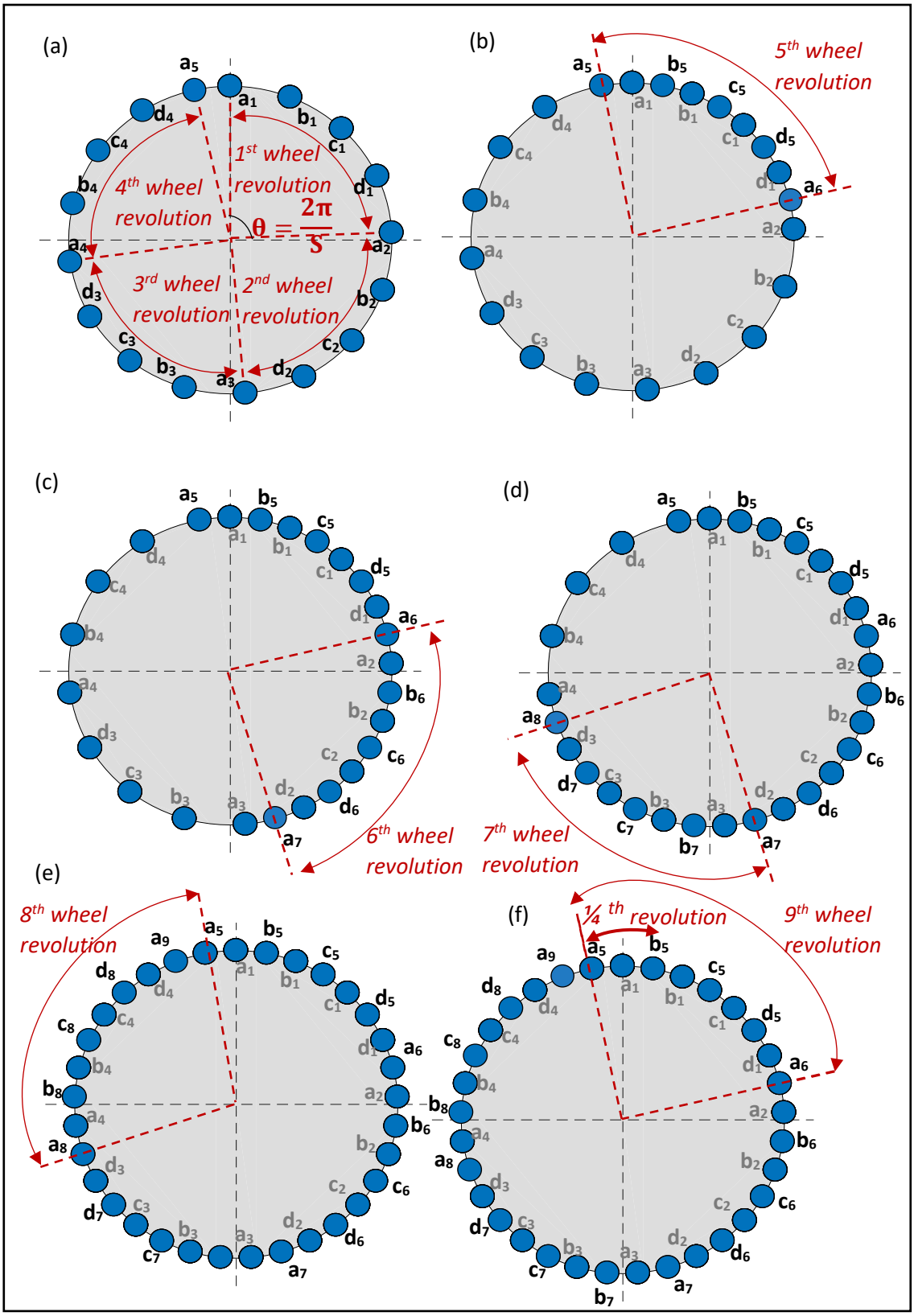

Figure 6.13: Synchronization for S=4.125 with 4 grain non-stochastic wheel model

Figure 6.13 (a) shows a projection of grains on the first wheel revolution of the grinding wheel. Note that the angle between *a5* and *a1* is half the angle between *a1* and *b1* and that synchronization has not occurred. Figure 6.13 (b) to Figure 6.13 (e) shows the progression of the grinding process until the eighth wheel revolution. Between the 4^{th} and 8^{th} revolution, grain contacts are between the previous grain contacts i.e. *b5* is between *a1* and *b1*. The eighth wheel revolution ends at a5 where the ninth revolution begins. It is important to note in Figure 6.13 (f) that the wheel's ninth revolution starts from *a5* and ends at *a6* but *a6* was already cut by of the wheel's earlier revolutions. This result means that the wheel performed cutting action on the workpiece only until the end of the eighth revolution. It took one-fourth of the ninth revolution to reach the synchronization point. The material removal stopped after 8.25 revolutions as the grains started to retrace the same paths taken by other grains in earlier wheel revolutions. Figure 6.13 (f) makes it clearer to understand the synchronization in this case. The ninth wheel revolution of the grinding wheel results in grains touching exactly the cut areas of initial revolutions where the material removal had already taken place. This result shows that the grinding took place for n=2 revolutions of the workpiece as predicted by Equations (6.25).

The comparison of examples in Figure 6.12 and Figure 6.13 shows that the synchronization case of n=2 will remove more material than the synchronization case of n=1 and have a better surface finish. Selecting speed ratios with greater material removal has the potential for achieving a better surface finish. This knowledge can be used to choose the speed ratios for optimized results.

6.3 Synchronization in Stochastic Wheel Model

It is important to study the synchronization phenomenon in cylindrical grinding using stochastic wheel models since the distribution of the abrasive grains on real grinding wheels is stochastic in nature. Stochastic wheel models have randomly-spaced grains with random protrusion heights.

6.3.1 Simplification of Stochastic Wheel Model into Single-grain Model

The approach taken in this thesis to study stochastic wheel models with irregular grain spacing and protrusion heights is to consider the wheel as a superposition of simple single-grain wheel models.

Figure 6.14 is a visual representation of how a 9-grain stochastic wheel model can be represented as nine single-grain wheel models. In other words, it can be said that the 9-grain stochastic model is a combined result of the addition of all the nine single-grain wheel models. The effect of the combined stochastic wheel model is equivalent to superimposing the effect of all the single-grain wheel models working independently. Thus, the theory and equations developed for a single grain model for predicting synchronization should apply to stochastic wheel models. We shall investigate the validity of this idea in the next section with kinematically-simulated examples.

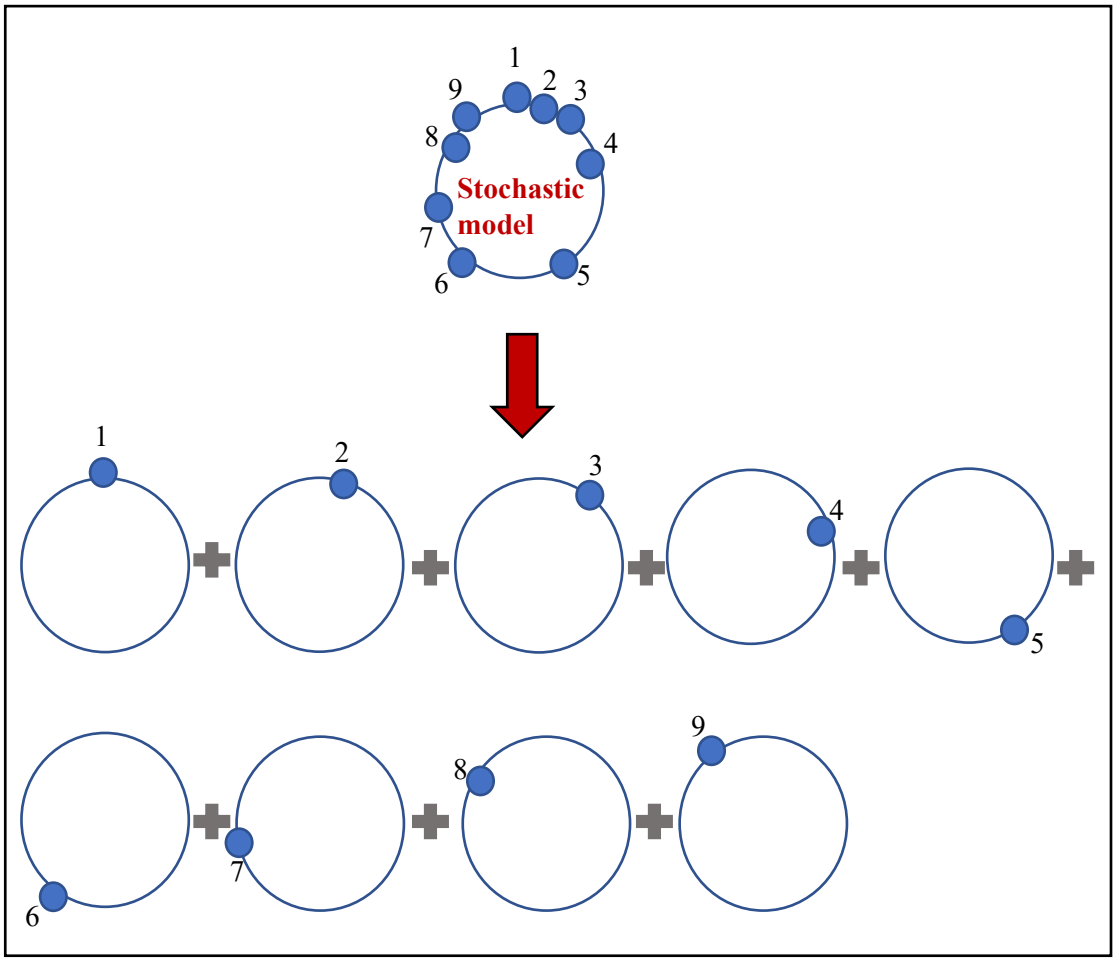

Figure 6.14: Breakdown of 9-grain stochastic wheel model into single grain wheel models

6.3.2 Kinematic Simulations of Cylindrical Grinding with Stochastic Wheel Model

This section intends to understand grain synchronization in cylindrical grinding with a stochastic wheel using kinematic simulations. The wheel model used for these simulations is made up of 14 grains stochastically distributed by shaking the nominal non-stochastic wheel model and changing their relative angular spacings and protrusions heights.

Equation 6.16 was used to predict the synchronization points of two different speed ratios for a single-grain wheel model and the cylindrical grinding simulator was used to simulate the cylindrical grinding process until the system achieved synchronization for each speed ratio. Table 6.1 lists these speed ratios and their predicted N_s^{syn} values for the kinematic simulation examples in this section (Figure 6.15 and Figure 6.16).

Speed ratio, S	Number of digits to the right of the decimal point, n	N_s^{syn} predicted by Equation 6.16
1.2	1	6
4.25	2	17

Table 6.1 Determination of synchronization points using Equation 6.16

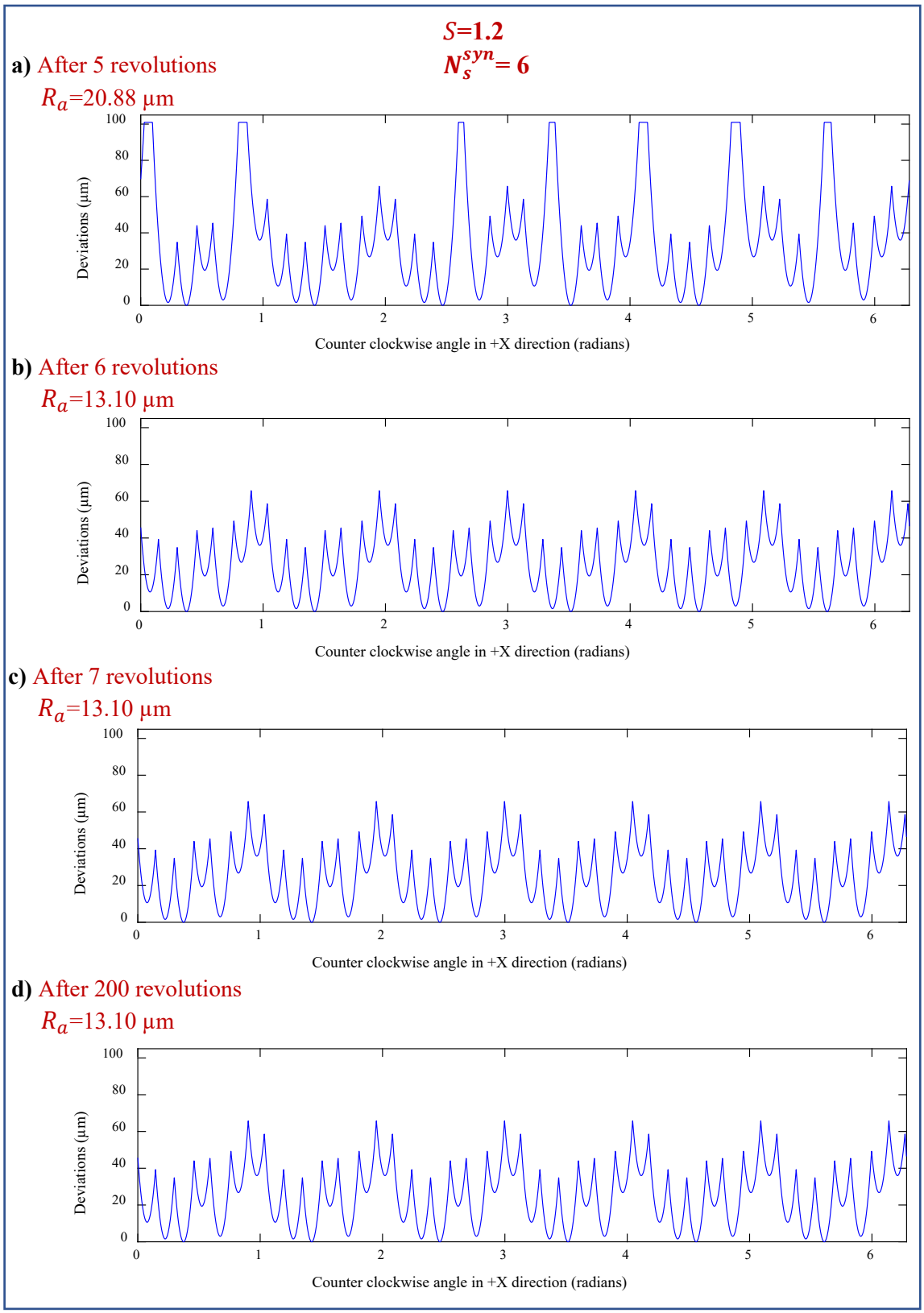

Figure 6.15: Simulated Workpiece profiles for S=1.2

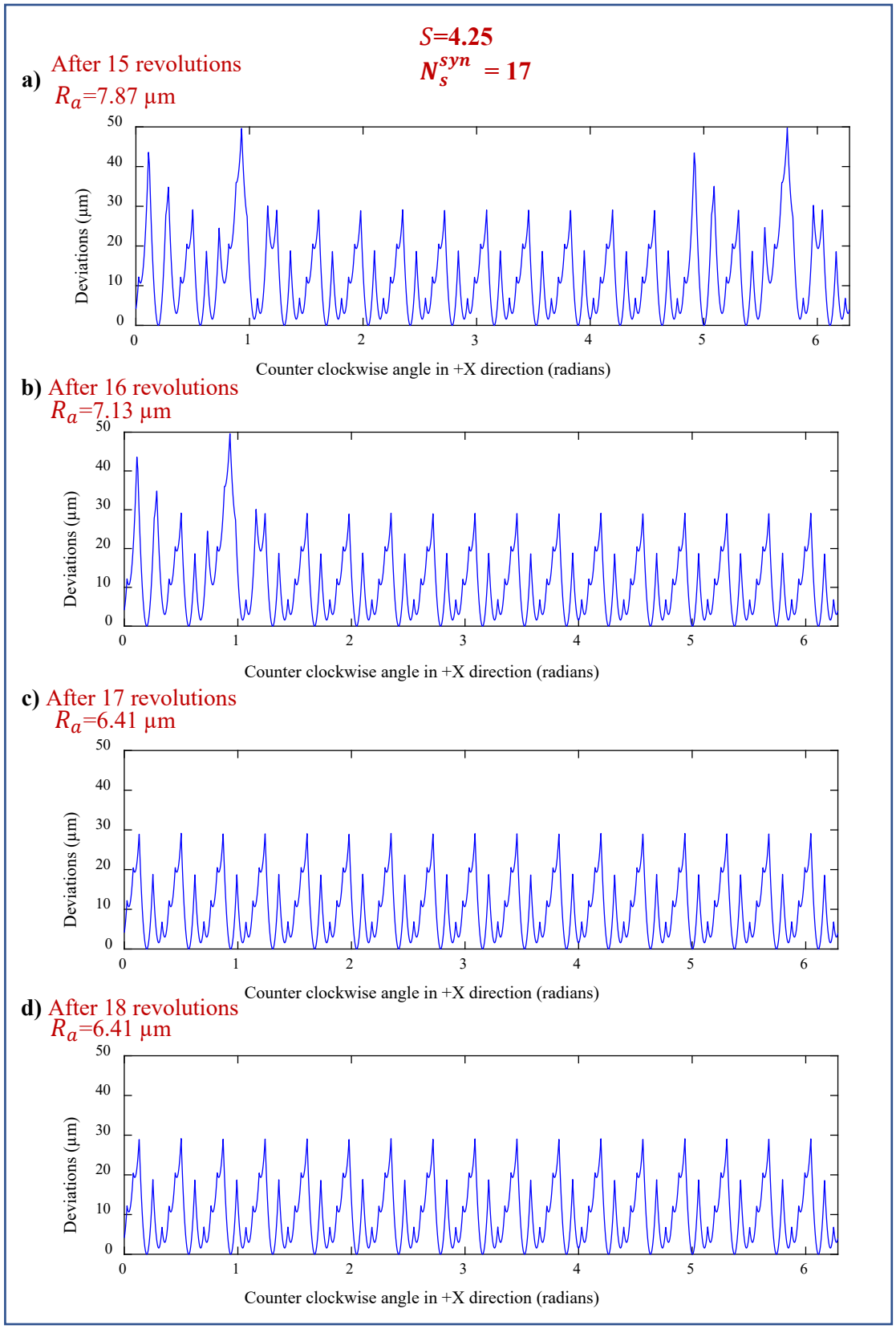

Figure 6.16: Simulated Workpiece profiles for *S*=4.25

Figure 6.15 shows simulation-based workpiece profiles for S=1.2 using the stochastic wheel model. Figure 6.15 can be compared with Figure 6 which shows a visual representation of synchronization for the same speed ratio with a single-grain wheel model. It is clear from Figure 6.15 that the workpiece surface profile ceases to change after the sixth wheel revolution as predicted in Table 6.1. A comparison of workpiece surface roughness values also confirms this result. The roughness of the workpiece at the sixth revolution and two hundredth revolution is the same (Figure 6.15 (a) and (d)). This observation means that material removal stopped at the synchronization point calculated by Equation 6.16 for S=1.2 at the sixth revolution. This result proves that the wheel grains retrace their previous paths over the workpiece surface for all the revolutions after the sixth one.

Figure 6.16 shows one more example of simulation-based workpiece profiles for S=4.25 using the stochastic wheel model. This figure shows the two profiles of the workpiece surface before the synchronization point of the system. It is clear from the figure that the workpiece surface profile changes until the seventeenth wheel revolution (Figure 6.16 (a) to (c)). A comparison of workpiece surface roughness values also indicates changes up to the 17th wheel reolution. The roughness of the workpiece for the seventeenth revolution is the same as for the eighteenth revolution (Figure 6.16 (d)). This observation means that the material removal stopped at the synchronization point predicted by Equation 6.16 for S=4.25 at seventeenth revolution. This result proves that the wheel grains retrace their previous paths over the workpiece surface for all the revolutions after the seventeenth revolution.

Batch simulations were performed for speed ratios from 4 to 5 in increments of 1/128 for 167, 65, 33, 19, and 9 wheel revolutions. Table 6.2 lists a sample of these speed ratios with their corresponding predicted N_s^{syn} values. Speed ratios of 4 and 5 had the minimum N_s^{syn}. As evident from the batch simulations shown in Figure 6.17, the surface roughness for S=4 and 5 remained unchanged for all different number of wheel revolutions. This result was observed because the N_s^{syn}value for S=4 and 5 is 4 and 5, respectively. Similarly, since S=4.5 reaches its synchronization point after 9 revolutions, the roughness did not change for 4.5 after that for any other simulation with more revolutions of the

grinding wheel. S=4.75 had no change in the final workpiece surface roughness values after 19 revolutions. Similarly, the surface roughness for S=4.0625 ceased to get better after 65 grinding wheel revolutions and the same was observed for S=4.125 after 33 revolutions. It can thus be said that the surface roughness does not decrease after N_s^{syn} revolutions for a given speed ratio. This result proves that the principles of single-grain self-synchronization apply to a multi-grain stochastic wheel model.

Speed ratio, S	Number of digits to the right of the decimal point, n	N_s^{syn} predicted by Equation 6.16
4.0625	4	65
4.125	3	33
4.75	2	19
4.5	1	9

Table 6.2: Determination of N_s^{syn} using Equation 6.16

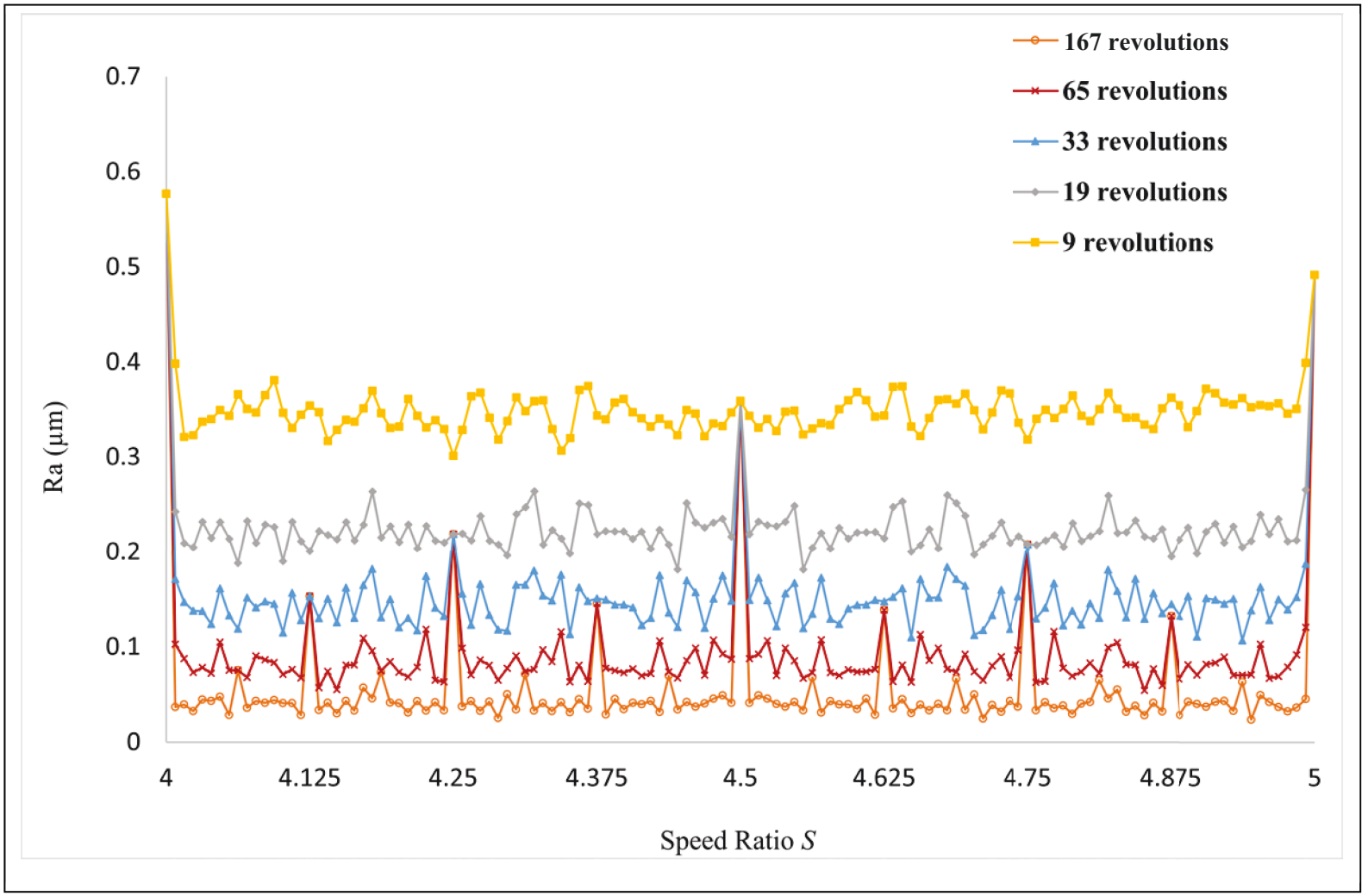

Figure 6.17: Non-grooved cylindrical plunge grinding simulations using stochastic wheel model

6.4 Conclusion of Synchronization Study

Synchronization depends mainly on the speed ratio *S*. The number of grains on the wheel N_g has an effect on grain synchronization if the wheel model is non-stochastic in nature. There are different cases of synchronization depending on whether the speed ratio is an integer or non-integer value, and whether the grain distribution on the grinding wheel is stochastic or non-stochastic.

Equations were derived to determine the minimum number of wheel revolution after which the system ceases to remove workpiece material. Synchronization for different speed ratio cases was studied. Most importantly, it was found that the synchronization calculation for single-grain wheel models is applicable for cylindrical grinding with real-world stochastic wheels. Since the actual cutting and material removal occur only up until synchronization has reached, continuing the grinding process beyond synchronization is unnecessary from a purely kinematics perspective. Furthermore, the synchronization phenomenon is undesirable since it stops further removal of material leading to a higher workpiece surface roughness. This knowledge can thus be used to analytically determine the speed ratios that reach synchronization as late as possible. The workpiece undergoes cutting for more revolutions when grinding with such speed ratios since the material removal takes place on every revolution of the grinding wheel.

Chapter 7

Discussion and Summary of the Findings of the Thesis

7.1 Explanation of Trends in Roughness Results of Experiments and Simulations

Having studied and developed an understanding of synchronization phenomenon, we can now look back at the results of experiments and simulations of Chapter 5 to explain the trends.

The decline of surface roughness value with an increase in speed ratio value in integer speed ratio study (Section 5.1) can be explained as a result of the increasing number of material removal cuts on the workpiece (since $N_s^{syn} = S$ for integer speed ratio synchronization in cylindrical grinding). The presence of S threads (for both the experimental and simulation workpiece surface) for S speed ratio can be explained as a consequence of insufficient material removal due to effective grinding of the workpiece for minimal S revolutions only.

The observation that the workpiece roughness ceased to decrease after 9 wheel revolutions for S=4.5 in dwell time study (Section 5.2) can be easily linked to the synchronization of wheel and workpiece since for S=4.5, $N_s^{syn} = 9$ according to Equation 6.16. The presence of 9 thin peak regions in simulated workpiece profile for S=4.5 can thus be explained as insufficiently-cut regions of the workpiece due to premature inactivation of wheel grains. It is also clear that grinding at S=4.22 was found to yield lower surface roughness than S=4.5 because of higher N_s^{syn} value for the speed ratio of 4.22.

The trends observed in experimental and simulated roughness in non-integer speed ratio study (Section 5.3) can also be explained using Equation 6.16 of grain synchronization in cylindrical grinding. The magnitude of N_s^{syn} for S=4.25 and S=4.75 is lower than other

speed ratios tested but higher than that of speed ratio 4.5. Hence, the roughness peaks for S=4.25 and 4.75 were the second highest. Similarly, S=4.125, 4.375, 4.625 and 4.875 had third fastest synchronization point and hence these speed ratios had third highest roughness peaks. The speed ratios with a high standard of surface finish had a significantly higher magnitude of N_s^{syn} which enabled prolonged and efficient cutting of the workpiece.

7.2 Comparison of Grooved Wheel Grinding and Non-Grooved Wheel Grinding

Table 7.1 shows the force, power and roughness data for grooved and non-grooved grinding with non-integer speed ratios. The experimental roughness ranged from 0.302 μm to 0.332 μm and the simulated roughness ranged from 0.048 μm to 0.479 μm for grooved wheel grinding. For non-grooved wheel grinding, the range of experimental roughness was from 0.189 μm to 0.246 μm and the simulated roughness ranged from 0.033 to 0.358 μm. The surface roughness was always found to be higher in grooved grinding compared to non-grooved grinding for the same speed ratio. The experimental surface roughness was higher by 32.9 % and the simulated roughness was higher by 28.2 % for the grooved wheel grinding as compared to the non-grooved wheel grinding. These experiments show that the speed ratio can improve the surface roughness by up to 10% for grooved wheels and 23% for non-grooved wheels.

The power for grooved-wheel grinding is reduced by 35 % on average compared to non-grooved-wheel grinding. This reduction in power consumption for the grooved wheel is a major advantage because the power consumption has a significant role in workpiece thermal damage. The normal force was 37.6% lower for the grooved wheel grinding than the non-grooved wheel grinding. Normal force value is also important because it affects time constant and workpiece deflection and workpiece deflection is detrimental in part tolerance.

	Grooved wheel				Non-grooved wheels				% diff. in Power	% diff. in Normal Force	% diff. in Ra	% diff. in Ra
S	Power (KW)	Normal Force (N)	Experimental Ra (µm)	Simulated Ra (µm)	Power (KW)	Normal Force (N)	Experimental Ra (µm)	Simulated Ra (µm)	(Exp.)	(Exp.)	(Exp.)	(Sim.)
4.04	0.52	22.04	0.306	0.058	0.81	34.8	0.199	0.047	-35.8	-36.7	+34.9	+18.9
4.125	0.5	20.07	0.313	0.24	0.77	32.76	0.214	0.153	-35.0	-38.7	+31.6	+36.2
4.22	0.53	22.22	0.308	0.055	0.8	34	0.189	0.033	-33.7	-34.6	+38.6	+40.0
4.25	0.46	18.10	0.318	0.324	0.75	31.75	0.23	0.218	-38.6	-43.0	+27.7	+32.7
4.41	0.56	20.81	0.306	0.053	0.85	34.97	0.194	0.039	-34.1	-40.5	+36.6	+26.4
4.5	0.38	16.80	0.332	0.479	0.62	26.19	0.246	0.358	-38.7	-35.8	+25.9	+25.3
4.59	0.55	20.03	0.304	0.051	0.81	33.64	0.195	0.039	-32.1	-40.5	+35.9	+23.5
4.75	0.44	17.80	0.316	0.306	0.67	27	0.226	0.207	-34.3	-34.0	+28.4	+32.3
4.78	0.52	21.90	0.302	0.048	0.74	32.4	0.193	0.038	-29.7	-32.4	+36.0	+20.8
4.875	0.49	19.20	0.313	0.219	0.72	30.54	0.214	0.132	-31.9	-37.1	+31.6	+39.7
4.96	0.51	21.46	0.304	0.049	0.87	36.27	0.198	0.042	-41.3	-40.8	+34.9	+14.3
Avg.	**46.64**	**20.03**			**76.45**	**32.21**			**35**	**37.6**	**32.9**	**28.2**

Table 7.1: Force, power and roughness data for grooved and non-grooved wheel grinding

Figure 7.1 plots the experimental surface roughness versus power for all the speed ratios tested. The fitted line through the grooved grinding data has a higher slope than the fitted line for the non-grooved grinding data. The roughness values of up to 0.30 µm are considered as a "fine quality" surface finish and the range of roughness values from 0.30 to 1.6 µm is considered as an "average quality" surface finish [17]. Therefore, the experimental surface roughness for non-grooved wheel grinding can be considered to be fine quality. The experimental surface roughness of the grooved-wheel grinding was just outside this category. This result shows that the grooved-wheel grinding is more sensitive to the selection of speed ratio on the resulting power and surface finish than the non-grooved wheel grinding. Considering the results of experiments for this thesis, for a non-integer value interval between 4 and 5, it can be concluded that the speed ratio of 4.22 produced the best surface finish for non-grooved-wheel grinding. A speed ratio of 4.78 produced the best surface roughness for grooved-wheel grinding, and the grinding power consumed for this speed ratio was significantly lower than all the non-grooved experiments. It can thus be said that for an interval of non-integer speed ratios between 4

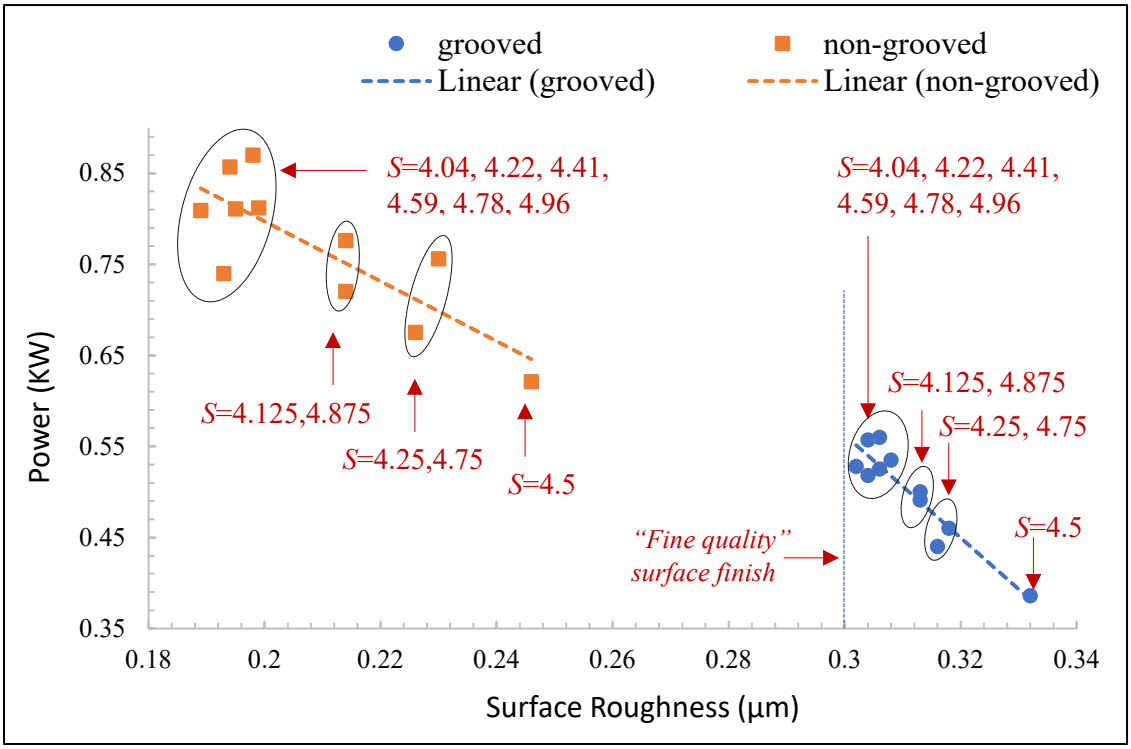

Figure 7.1: Trend in power with surface roughness for grooved and non-grooved wheel grinding

and 5, the speed ratio of 4.78 is optimal for grooved wheel grinding for best surface finish and low power consumption.

It should be noted that the best surface-finish-yielding speed ratios for grooved-wheel grinding like 4.04, 4.22, 4.41, 4.59, 4.78 and 4.96 were found to have values in the range of 0.302 μm to 0.308 μm which is very close to the standard 0.30 μm fine quality surface finish. There is potential to further improve the surface quality with these speed ratios in grooved wheel grinding with a cylindrical grinding set up where the wheel-workpiece speeds can be controlled more accurately. One more factor that can improve the result would be the accuracy of achieving the desired speed ratio. With the knowledge of grain-synchronization, speed ratios with higher N_s^{syn} can be selected to further improve the surface finish with grooved wheels.

7.3 Conclusion

The experimental and simulation results of surface roughness recorded in Chapter 5 were explained using the newly-developed understanding of N_s^{syn}. The performance of grooved wheels and non-grooved wheels was compared for surface finish, process forces and power consumption.

Chapter 8

Conclusion

All the four main objectives and the outcomes of the work for their accomplishment are discussed in this chapter.

The first objective of this thesis was to investigate a wide range of speed ratios for workpiece surface topography using grooved and non-grooved wheel. This investigation was planned in three systematic studies. The integer speed ratio experiments yielded workpiece textures as opposed to the non-grooved grinding experiments at the same conditions. The surface roughness of the workpieces ground with integer speed ratios was larger than the non-grooved grinding experiments for both the experimental and simulation results. This study was followed by a dwell time study that investigated the effect of various dwell times on the workpiece surface finish. No improvement in the workpiece surface finish was observed after 10 seconds of dwell time in both the experimental and simulation results. This knowledge of maximum dwell time was used for the non-integer speed ratio study experiments and simulations.

The second objective of this work was to find a speed ratio that yields a surface for the grooved wheel as smooth as for the non-grooved wheel, but no such speed ratio was found. The most important reason for this result can be found by looking at the workpiece profiles generated by the simulator in Chapter 5 which shows that the grooved wheel created fewer grain-trajectories on the workpiece than the non-grooved wheel because of the difference in the active cutting area on the grinding wheel. This lower number of material-removal cuts of grooved-wheel grains result in sweeping of less area on the workpiece than the non-grooved wheel leaving insufficiently cut peaks on the workpiece that contributes to raised surface roughness. The simulation results support the

experimental findings in that the surface finish for grooved wheels is never better than the non-grooved wheels. One solution may be to change the distribution of active and passive areas of the grinding wheel to better represent the active grain distribution on a grooved wheel.

The third objective was to determine optimal and undesirable speed ratios for workpiece surface roughness. The non-integer speed ratios like 4.22, 4.41, and 4.59 were found to yield a fine surface finish. The speed ratio of 4.5 yielded the highest surface roughness of all the non-integer speed ratios followed by the speed ratios like 4.25 and 4.75. This observation of good and bad surface-finish-yielding speed ratios was consistent for both the experimental and the simulation results. Also, for the same speed ratio, grooved wheels yielded a rougher surface finish but applied less process forces and consumed less power than the non-grooved wheels. The trend of experimental surface roughness values for different non-integer speed ratios was very similar to that of the simulation results. The speed ratio of 4.22 was found to be optimal for non-grooved-wheel grinding and the speed ratio of 4.78 was found to be optimal for grooved-wheel grinding, while the speed ratio of 4.5 was found to be the most undesirable non-integer speed ratio for the surface finish between the interval from 4 to 5.

The fourth objective of this thesis was to develop methods that could predict the effectiveness of a speed ratio value on the workpiece surface finish. The approach adopted for the work of this objective was to develop a knowledge base on the synchronization phenomenon in cylindrical grinding that could additionally explain the trends in simulation and experimental results of this thesis work. Using kinematics, formulas to predict the minimum number of grinding wheel revolutions required for synchronization in constant-velocity plunge cylindrical grinding for different speed ratio cases were derived. The concept of synchronization was built upon by starting from simple synchronization cases of single grain interaction to multiple grain non-stochastic wheel model interaction with the workpiece. These concepts were eventually applied to stochastic wheel model

interaction with the workpiece replicating the real-world cylindrical grinding process. A series of batch simulations within the speed ratios 4 and 5 were performed at different dwell times to further help understand the dependence of the synchronization phenomenon on speed ratio value. It was concluded that integer speed ratios yield rougher surfaces due to early synchronization which results in the wheel grains being effectively inactive. The workpiece textures created by grooved grinding at integer speed ratios is also a result of early synchronization which results in insufficient material removal thereby leaving a thread-like pattern on the workpiece. The non-integer speed ratios yielded a smoother surface than integer speed ratios because of the higher value of their grinding wheel revolutions for synchronization. Also, the observation that the surface finish for certain non-integer speed ratios was better than other tested speed ratios was explained by the increase in the number of grinding wheel revolutions required for synchronization. Studying the synchronization phenomenon helped explain the results of experiments and simulations. With the newly-discovered understanding of synchronization phenomenon in cylindrical grinding, it is now possible to choose the speed ratios that would take a higher number of grinding wheel revolutions to attain synchronization for a good quality surface finish thereby helping to improve the cylindrical grinding process easily.

The key takeaway of this thesis is that choosing and successfully achieving the right speed ratio that synchronizes as late as possible (higher N_s^{syn}) can yield a high standard of surface quality even with grooved wheels along with the addition of proven benefits like low power consumption, process forces and thermal damage to the workpiece.

8.1 Recommendations for Future Work

- Non-constant speed cylindrical grinding can be worth investigating with the initial phase of material removal with low power consuming speed ratio like 4.5 until the commanded depth is achieved followed by a high surface finish yielding speed ratios like 4.22 or 4.78. This method can be a solution to an efficient cylindrical grinding process for power and surface finish.

- The current 2D cylindrical grinding simulator has the potential to improve in terms of addition of plunge velocity and simulation of the workpiece profiles along the axial direction. These modifications will allow for 3D simulations of the cylindrical workpiece.
- Cylindrical traverse grinding can also be investigated for the effect of speed ratios on workpiece surface finish at different axial feed rates.

Bibliography

[1] Groover, M. P. “Grinding and other Abrasive Processes” *Fundamentals of Modern Manufacturing*, Third Edition., John Wiley & Sons, 2007, pp. 595-612.

[2] Schneider, George Jr. “Grinding Wheels and Operations.” *Cutting Tool Applications*, ISBN-13: 978-0615121918

[3] Marinescu, Ioan D., et al. *Handbook of Machining with Grinding Wheels*. CRC / Taylor & Francis Group, LLC, 2007.

[4] Dewar, Scott. *Design and Application of a CNC Rotary Axis for Grinding Research*. M.A.Sc. Dissertation, Dept. of Mechanical Engineering, Dalhousie University, Halifax, Canada, 2017.

[5] Nadolny, Krzysztof. “Estimation of the Active Grains Load in Different Kinematic Variations of the Internal Cylindrical Grinding Process.” *The International Journal of Advanced Manufacturing Technology*, vol. 89, no. 9, 2017, pp. 3337–3348.

[6] Nadolny, Krzysztof. “A Review on Single-Pass Grinding Processes.” *Journal of Central South University*, vol. 20, no. 6, 2013, pp. 1502–1509.

[7] Heywood, J. *Grinding Wheels and Their Uses.* Second Edition, The Penton Publishing Co., 1942.

[8] Marinescu, Ioan D. *Tribology of Abrasive Machining Processes*. 2nd ed., William Andrew, 2013.

[9] American National Standards Institute, American national standard: markings for identifying grinding wheels and other bonded abrasives. ANSI: B74.13-1982, New York, NY: American National Standards Institute, 6th ed., 1982.

[10] McDonald, Andrew. *Investigation of Grinding Wheel Wear Using a White Chromatic Sensor*. M.A.Sc. Dissertation, Dept. of Mechanical Engineering, Dalhousie University, Halifax, Canada, 2015.

[11] Jackson, M. J. "Modelling of Fracture Wear in Vitrified CBN Grinding Wheels." *Journal of Achievemnets in Materials and Manufacturing Engineering,* vol. 24, no. 1, 2007, pp. 230–36.

[12] Darafon, Abdalslam, et al. "3D Metal Removal Simulation to Determine Uncut Chip Thickness, Contact Length, and Surface Finish in Grinding." *The International Journal of Advanced Manufacturing Technology*, vol. 66, no. 9, 2013, pp. 1715–1724.

[13] Forbrigger, Cameron, et al. "A Review of State-of-the-Art Vitrified Bond Grinding Wheel Grooving Processes." *International Journal of Advanced Manufacturing Technology*, vol. 90, no. 5-8, 2017, pp. 2207–2216.

[14] Verkerk, J. "Slotted Wheels to Avoid Cracks in Precision Grinding." *1979 Proceedings: Sixteenth Annual Abrasive Engineering Society Conference/ Exhibition*, 1979, pp. 75–81.

[15] Malkin, Stephen. "Grinding Geometery and Kinematics." *Grinding Technology*, Society of Manufacturing Engineers, 1989, pp. 45-78.

[16] Darafon, Abdalslam. *Measuring and Modeling of Grinding Wheel Topography.* Ph.D. Dissertation, Dept. of Mechnanical Engineering, Dalhousie University, Halifax, Canada, 2013.

[17] Mohamed, Al-Mokhtar. *Investigation of Circumferentially-grooved Grinding Wheels for Creep-feed Grinding*. Ph.D. Dissertation, Dept. of Mechanical Engineering, Dalhousie University, Halifax, Canada, 2014.

[18] Gadelmawla, E. S., et al. "Roughness Parameters." *Journal of Materials Processing Technology*, vol. 123, no. 1, 2002, pp. 133–145.

[19] McDonald, Andrew, et al. “Kinematic Simulation of the Uncut Chip Thickness and Surface Finish Using a Reduced Set of 3D Grinding Wheel Measurements.” *Precision Engineering*, vol. 49, 2017, pp. 169–178.

[20] George, Lijohn P., et al. “Study on Surface Roughness and Its Prediction in Cylindrical Grinding Process Based on Taguchi Method of Optimization.” *International Journal of Scientific and Research Publication,* vol. 3, no. 5, 2013, pp. 1–5.

[21] Panthangi, Ravi Kumar.,“Optimization of Surface Roughness in Cylindrical Grinding Process.” *International Journal of Applied Engineering Research*, vol. 12, no. 18, 2017, pp. 7350–54.

[22] Patil, Kshitij R., et al “Modeling and Optimization of Cylindrical Grinding Parameters for MRR and Surface Roughness.” *International Journal of Engineering Sciences and Research Technology,* vol. 6, no. 4, 2017, pp-498-503.

[23] Pal, Pradip Kumar., “Effects of Process Parameters on Surfaec Finish in Cylindrical Grinding.” *Advanced Materials Research,* vols. 264-265, 2011, pp. 1118-1123.

[24] Kumar, Kundan, et al. “Optimal Material Removal and Effect of Process Parameters of Cylindrical Grinding Machine by Taguchi Method.” *International Journal of Advanced Engineering Researh and Studies,* E-ISSN2249-8974.

[25] Kumar, Naresh, et al. “Optimization of Cylindrical Grinding Process Parameters on C40E Steel Suing Taguchi Method.” *International Journal of Engineering Research and Applications,* vol. 5, 1-3, 2015, pp. 100-104.

[26] Rudrapati, Ramesh, et al. “Investigation on Surface Roughness in Cylindrical Grinding.” *CP1315, International Conference on Advances in Materials and Processing Technology,* 2010.

[27] Krishnan, Radhan B., et al. “Prediction of Surface Roughness (AISI 4140 Steel) in Cylindrical Grinding Operation by RSM.” *International Journal for Research and Development in Technology,* vol. 9, no. 3, 2018, pp. 702-704.

[28] Thiagarajan, C, et al. “Modeling and Optimization of Cylindrical Grinding of Al/SiC Composites Using Genetic Algorithms.” *Journal of the Brazilian Society of Mechanical Sciences and Engineering*, vol. 34, no. 1, 2012, pp. 32–40.

[29] Rudrapati, Ramesh, et al. “Modelling for Surface Roughness in Cylindrical Grinding*” Int. J. Machining and Machinability of Materials,* vol. 12, no.1/2, 2012, pp. 28–36.

[30] Sharma, Rajani, et al. “*Optimization of Surface Roughness in Cylindrical Grinding.” International Research Journal of Engineering and Technology,* vol. 3, no. 12, 2016, pp. 482–486.

[31] Kiyak, M., et al. “A Study on Surface Roughness in External Cylindrical Grinding.” *12th International Scientific Conference Achievments in Mechanical and Materials Engeneering*, 2003, pp. 459-462.

[32] Zahedi, Ali. and Azarhoushang, Bahman. “FEM Based Modeling of Cylindrical Grinding Process Incorporating Wheel Topography Measurement.” *Procedia CIRP*, vol. 46, 2016, pp. 201–204.

[33] Ding, Zishan, et al. “Investigation of the Grinding Temperature and Energy Partition during Cylindrical Grinding.” *The International Journal of Advanced Manufacturing Technology*, vol. 97, no. 5, 2018, pp. 1767–1778.

[34] Liu, Yueming, et al. “Experimental and Numerical Investigation into Workpiece Surface Topology in Point Grinding.” *Proceedings of the Institution of Mechanical Engineers, Part B: Journal of Engineering Manufacture*, vol. 226, no. 11, 2012, pp. 1793–1800.

[35] Botcha, Bhaskar, et al. “Process-Machine Interactions and a Multi-Sensor Fusion Approach to Predict Surface Roughness in Cylindrical Plunge Grinding Process.” *Procedia Manufacturing*, vol. 26, 2018, pp. 700–711.

[36] Karanja, Samuel karanja., “Dynamic Modeling of Chatter Vibration in Cylindrical Plunge Grinding Process.” *Innovative Systems Design and Engineering*, vol. 2, no. 4, 2011, ISSN 2222-2871.

[37] Wang, Jia-Zhong, et al. “Prediction of Surface Roughness in Cylindrical Traverse Grinding Based on ALS Algorithm.” *Proceedings of the Fourth International Conference on Machine Learning and Cybernetics, Guangzhou,* August, 2005, pp. 549–54.

[38] Chi, Jun, et al. “The Study on a Simulation Model of Workpiece Surface Topography in External Cylindrical Grinding.” *The International Journal of Advanced Manufacturing Technology*, vol. 82, no. 5, 2016, pp. 939–950.

[39] Guo, Jianliang. “Surface Roughness Prediction by Combining Static and Dynamic Features in Cylindrical Traverse Grinding.” *The International Journal of Advanced Manufacturing Technology*, vol. 75, no. 5, 2014, pp. 1245–1252.

[40] Voronov, S. A, and Veidun, Ma. “Mathematical Modeling of the Cylindrical Grinding Process.” *Journal of Machinery Manufacture and Reliability*, vol. 46, no. 4, 2017, pp. 394–403.

[41] Lee, E. S., et al. “Simulation of Cylindrical Plunge Grinding Based on the Behaviour of Cutting Edge Wear.” *International Journal of Production Research*, vol. 35, no. 10, 1997, pp. 2917–2938.

[42] Kim, Jeong-Du, et al. “Development of Discontinuous Grinding Wheel with Multi-Porous Grooves” *Int. J. Mach. Tools Manufact,* 1997, vol. 37, no. 11, pp 1611-1624.

[43] Nakayama, K., et al. “Grinding Wheel with Helical Grooves - an Attempt to Improve the Grinding Performance” *CIRP Annals Manufacturing Technology,* vol. 26, no. 1, pp. 133-138.

[44] Mohamed, AL-Mokhtar, et al. “A Novel Method for Grooving and Re-Grooving Aluminum Oxide Grinding Wheels.” *The International Journal of Advanced Manufacturing Technology*, vol. 73, no. 5, 2014, pp. 715–725.

[45] Li, Hao Nan. and Axinte, Dragos. “Textured Grinding Wheels: A Review.” *International Journal of Machine Tools and Manufacture*, vol. 109, 2016, pp. 8–35.

[46] Aslan, D. and Budak, E. “Surface Roughness and Thermo-Mechanical Force Modeling for Grinding Operations with Regular and Circumferentially Grooved Wheels.” *Journal of Materials Processing Technology*, vol. 223, 2015, pp. 75–90.

[47] Suto, Tetsuya, et al. “High Performance Creep Feed Grinding of Difficult-to-Machine Materials with New-Type Wheels.” *Bulletin of the Japan Society of Precision Engineering*, vol. 24, no. 1, 1990, pp. 39–44.

[48] Kwak, Jae-Seob. and Man-Kyung Ha. “Force Modeling and Machining Characteristics of the Intermittent Grinding Wheels.” *KSME International Journal*, vol. 15, no. 3, 2001, pp. 351–356.

[49] Mohamed, Al-Mokhtar, et al. “Uncut Chip Thickness and Coolant Delivery Effects on the Performance of Circumferentially Grooved Grinding Wheels.” *The International Journal of Advanced Manufacturing Technology*, vol. 85, no. 5, 2016, pp. 1429–1438.

[50] Waida, Tohru, et al. “Creep Feed Grinding of Ceramics and Ceramic-Matrix Composites with slotted & Perforated Wheels” *Journal of the Japan Society of Precision Engineering,* vol. 57, no. 7, pp. 324-329, 1991.

[51] Oliveira, J.F.G., et al. “A Novel Dressing Technique for Texturing of Ground Surfaces.” *CIRP Annals - Manufacturing Technology*, vol. 59, no. 1, 2010, pp. 361–364.

[52] Denkena, B., et al. “Grinding with Patterned Grinding Wheels.” *CIRP Journal of Manufacturing Science and Technology*, vol. 8, 2015, pp. 12–21.

[53] Mohamed, Al-Mokhtar, et al. “Application of Shallow Circumferential Grooved Wheels to Creep-Feed Grinding.” *Journal of Materials Processing Technology*, vol. 213, no. 5, 2013, pp. 700–706.

[54] Uhlmann, E., and Hochschild, L. “Tool Optimization for High Speed Grinding.” *Production Engineering*, vol. 7, no. 2, 2013, pp. 185–193.

[55] Gavas, M., et al. “A Novel Method to Improve Surface Quality in Cylindrical Grinding.” *Experimental Techniques*, vol. 35, no. 1, 2011, pp. 26–32.

[56] Gavas, Muammer, et al. “Effects of Various Helically Angled Grinding Wheels on the Surface Roughness and Roundness in Grinding Cylindrical Surfaces.” *Materials and Technology*, vol. 49, no. 6, 2015, pp. 865–870.

[57] Köklü, Uğur. “Grinding with Helically Grooved Wheels.” *Proceedings of the Institution of Mechanical Engineers, Part E: Journal of Process Mechanical Engineering*, 2014, vol. 228, no. 1, pp. 33–42.

[58] Tawakoli, Taghi, et al. “An Experimental Investigation on the Characteristics of Cylindrical Plunge Dry Grinding with Structured CBN Wheels.” *Procedia CIRP*, vol. 1, no. 1, 2012, pp. 399–403.

[59] Dewar, S., et al. “Application of High-Angle Helical-Grooved Vitrified Wheels to Cylindrical Plunge Grinding.” *The International Journal of Advanced Manufacturing Technology*, vol. 96, no. 5, 2018, pp. 2443–2453.

[60] Dewar, Scott, et al. “Effect of Speed Ratio on Surface Finish using Circumferentially-Grooved Vitrified Bond Wheels in Cylindrical Plunge Grinding.” *ISSAT*, 2018.

[61] Wikipedia contributors. "Rational number." *Wikipedia, The Free Encyclopedia*. Wikipedia, The Free Encyclopedia, 24 Mar. 2019. Web. 26 Mar. 2019.